



**HAL**  
open science

# Non-linear regime of cosmic structure formation

Linda Blot

► **To cite this version:**

Linda Blot. Non-linear regime of cosmic structure formation: Imprints on the covariance of the power spectrum and dynamics of Dark Energy inhomogeneities. *Cosmology and Extra-Galactic Astrophysics* [astro-ph.CO]. Observatoire de Paris, 2015. English. NNT : . tel-01246351

**HAL Id: tel-01246351**

**<https://hal.science/tel-01246351>**

Submitted on 18 Dec 2015

**HAL** is a multi-disciplinary open access archive for the deposit and dissemination of scientific research documents, whether they are published or not. The documents may come from teaching and research institutions in France or abroad, or from public or private research centers.

L'archive ouverte pluridisciplinaire **HAL**, est destinée au dépôt et à la diffusion de documents scientifiques de niveau recherche, publiés ou non, émanant des établissements d'enseignement et de recherche français ou étrangers, des laboratoires publics ou privés.

# OBSERVATOIRE DE PARIS

ECOLE DOCTORALE  
ASTRONOMIE ET ASTROPHYSIQUE D'ILE-DE-FRANCE

DOCTORAT  
ASTRONOMIE ET ASTROPHYSIQUE

Linda BLOT

---

## RÉGIME NON-LINÉAIRE DE FORMATION DES STRUCTURES COSMIQUES

Empreintes sur la covariance du spectre de puissance et  
dynamique des inhomogénéités d'énergie noire

---

Thèse dirigée par: Dr. Pier Stefano CORASANITI  
Soutenue le 1 Octobre 2015  
devant le jury composé de:

Dr. Pier Stefano Corasaniti	Directeur de thèse
Pr. Hervé Dole	Examineur
Pr. Simona Mei	Présidente du jury
Pr. Lauro Moscardini	Rapporteur
Pr. Will J. Percival	Rapporteur
Dr. Filippo Vernizzi	Examineur



# Résumé

Dans le futur proche, de nombreux sondages de galaxies fourniront une cartographie de la distribution de la matière dans l'univers, avec laquelle il sera possible de contraindre les paramètres cosmologiques avec une précision inégalée. Cela implique que les prédictions théoriques des observables en question doivent atteindre une précision suffisante pour pouvoir être comparées aux observations et extraire le maximum d'information cosmologique. Ces sondages ont été conçus pour comprendre la nature de l'énergie noire, une composante dont on a supposé l'existence pour expliquer l'accélération de l'expansion de l'univers observée à bas décalage vers le rouge. Dans le modèle standard de la cosmologie, cette composante est représentée par une constante cosmologique  $\Lambda$  qui domine le budget énergétique de l'univers aujourd'hui. Même si le modèle  $\Lambda$ CDM reste en bon accord avec les observations, de nombreux problèmes théoriques concernant la nature de la constante cosmologique motivent l'étude d'un très grand nombre de modèles alternatifs, qui doivent maintenant être mis à l'épreuve des observations. Pour ce faire, il est nécessaire de tenir compte des effets de la dynamique non-linéaire du processus d'effondrement gravitationnel. Cette thèse se place dans ce contexte, en utilisant les simulations N-corps comme outil pour relier aux observations la théorie de la formation des structures cosmiques dans le régime non-linéaire. D'un côté je vais explorer l'impact des effets non-linéaires sur l'estimation des paramètres cosmologiques dans le cadre d'une interprétation statistique des données. Celle-ci nécessite le calcul de la matrice de covariance du spectre de puissance de la matière. L'estimation de cette matrice au moyen des simulations permet de quantifier l'importance de ces effets qui, si négligés, peuvent biaiser les résultats ou amener à une sous-estimation des erreurs statistiques sur les paramètres cosmologiques. De l'autre, je vais présenter les méthodes numériques pour résoudre l'évolution d'un fluide d'énergie noire dans le cas où les perturbations ont une vitesse de propagation très faible devant celle de la lumière. En s'effondrant l'énergie noire laisse des empreintes distinctes sur la distribution de matière dans l'univers. Dans ce cas, l'énergie noire ne peut être traitée comme un fluide homogène

et son evolution doit être suivie dans le régime non-linéaire en meme temps que celle de la matière noire. Ces méthodes numériques, une fois couplées avec un code N-corps, permettront de produire les premières simulations de l'évolution cosmique d'un modèle d'énergie noire in-homogène.

## **Mots clés**

Cosmologie, structure à large échelle, Energie Noire, méthodes numérique

---

**NON-LINEAR REGIME OF COSMIC STRUCTURE  
FORMATION**

**Imprints on the covariance of the power spectrum and  
dynamics of Dark Energy inhomogeneities**

---



# Summary

In the near future numerous galaxy surveys are going to provide a cartography of the distribution of matter in the universe, with which it will be possible to constrain the cosmological parameters with an unprecedented precision. This means that theoretical predictions of the observables at issue need to attain a high level of precision, so that we can extract the maximum cosmological information when comparing them to observations. Upcoming surveys have been conceived to understand the nature of dark energy, a component of which we have postulated the existence to explain the acceleration of the expansion of the universe observed at low redshift. In the standard cosmological model this component is represented as a cosmological constant  $\Lambda$  that dominates the energy budget of the universe today. Even if the  $\Lambda$ CDM model remains in good agreement with observations, a number of theoretical problems regarding the nature of the cosmological constant justify the study of a great number of alternative models, that now have to be put to the test with observations. To do so, it is necessary to take into account the effects of the non-linear dynamics of the gravitational collapse process. This thesis is placed in this context, using N-body simulations as a tool to link observations to the theory of cosmic structure formation in non-linear regime. On one side we are going to explore the impact of non-linear effects on the estimation of cosmological parameters in a statistical framework. This requires the computation of the covariance matrix of the matter power spectrum. The estimation of this matrix using simulations allows the quantification of the importance of non-linear effects that, if neglected, can bias the results or lead to an under-estimation of the statistical errors on the cosmological parameters. On the other side, we are going to present the numerical methods to solve the evolution of a dark energy fluid with perturbations that have a very low speed of propagation with respect to the speed of light. Collapsing dark energy perturbations leave a distinctive imprint on the distribution of matter in the universe. In this case, dark energy cannot be treated as a homogeneous fluid and its evolution has to be followed in the non-linear regime together with the dark matter component. These numerical methods, once

coupled to an N-body code, will allow the production of the first simulations of the evolution of an inhomogeneous dark energy model.

## **Keywords**

Cosmology, Large Scale Structure, Dark Energy, numerical methods

Cette thèse a été préparée au sein du LUTh - Observatoire de Paris,  
Meudon



Laboratoire de l'Univers et de ses Théories



# Contents

<b>1</b>	<b>Introduction</b>	<b>1</b>
1.1	A brief history of modern Cosmology . . . . .	2
1.2	State-of-the-art Cosmology . . . . .	6
1.2.1	Dark Matter . . . . .	6
1.2.2	Dark Energy . . . . .	8
1.3	Plan of the thesis . . . . .	9
<b>I</b>	<b>Theoretical Cosmology</b>	<b>11</b>
<b>2</b>	<b>Cosmological models</b>	<b>13</b>
2.1	Distances in cosmology . . . . .	13
2.2	Hubble’s law . . . . .	16
2.3	Hot Big Bang model . . . . .	17
2.3.1	Big Bang singularity . . . . .	19
2.3.2	Cosmological horizons . . . . .	20
2.3.3	Thermal history of the universe . . . . .	20
2.4	Einstein–de Sitter universe . . . . .	23
2.5	$\Lambda$ CDM scenario . . . . .	24
2.6	Scalar field models of Dark Energy . . . . .	25
2.6.1	Quintessence . . . . .	26
2.6.2	K-essence . . . . .	27
<b>3</b>	<b>Structure formation</b>	<b>29</b>
3.1	Statistical treatment of perturbations . . . . .	30
3.2	Linear Perturbation Theory . . . . .	34
3.2.1	Power spectrum evolution in linear regime . . . . .	40
3.3	Non-linear regime . . . . .	41
3.3.1	The Zel’dovich approximation . . . . .	43
3.3.2	Spherical collapse . . . . .	46

<b>4</b>	<b>Numerical simulations</b>	<b>49</b>
4.1	N-body techniques . . . . .	50
4.2	Eulerian hydrodynamics . . . . .	52
4.3	Generation of initial conditions . . . . .	55
4.4	Power spectrum estimation . . . . .	56
<b>II</b>	<b>Cosmology with large volume galaxy surveys</b>	<b>61</b>
<b>5</b>	<b>Cosmological dependence of the large scale structure of the universe</b>	<b>63</b>
5.1	Galaxy power spectrum . . . . .	64
5.2	Baryon Acoustic Oscillations . . . . .	65
5.2.1	Non-linear effects on BAO . . . . .	66
5.3	Bayesian methods for cosmological parameter inference . . . . .	67
5.3.1	Maximum Likelihood Estimator . . . . .	69
5.3.2	Fisher matrix . . . . .	70
5.3.3	Information content of galaxy surveys . . . . .	71
5.4	Contributions of this thesis . . . . .	72
<b>6</b>	<b>Matter power spectrum covariance matrices from the DEUS-PUR simulations</b>	<b>73</b>
6.1	N-body dataset . . . . .	74
6.2	Power Spectrum & Covariance Matrix Estimators . . . . .	76
6.3	Numerical Simulation Mass Resolution Errors . . . . .	77
6.4	Fourier Mode Correlations . . . . .	84
6.5	Probability Distribution of the Power Spectrum Estimator . . . . .	86
<b>7</b>	<b>Non-linear covariance matrix errors and cosmological parameter uncertainties for Euclid-like surveys</b>	<b>93</b>
7.1	Signal-to-Noise . . . . .	93
7.2	Covariance and Precision Matrix Errors . . . . .	96
7.2.1	Precision Matrix Bias . . . . .	97
7.2.2	Variance of Sample Covariance . . . . .	98
7.2.3	Variance of Sample Precision Matrix . . . . .	100
7.3	Covariance Estimation Errors and Parameter Forecast . . . . .	104
<b>III</b>	<b>Numerical methods for Dark Energy simulations</b>	<b>111</b>
<b>8</b>	<b>Numerical methods for clustering Dark Energy simulations</b>	<b>113</b>
8.1	Euler Equations for Dark Energy Fluids . . . . .	115

8.2	The Riemann Problem . . . . .	117
8.2.1	Generalised Riemann Invariants . . . . .	120
8.2.2	Rarefaction Waves . . . . .	120
8.2.3	Shock Waves . . . . .	122
8.2.4	Exact Riemann Solver . . . . .	123
8.2.5	Approximate Riemann Solvers . . . . .	127
8.2.6	Specificities of the Riemann Problem for Dark Fluids . . . . .	128
8.3	Wave structure in 3D . . . . .	129
8.4	Upwind Numerical Schemes . . . . .	132
8.4.1	Conservative Hyperbolic Methods . . . . .	132
8.4.2	MUSCL-Hancock Method . . . . .	134
8.4.3	Piecewise Linear Method (PLM) . . . . .	136
8.4.4	Piecewise Parabolic Method (PPM) . . . . .	139
8.5	Euler Equations in Supercomoving Variables . . . . .	139
8.6	Euler Equations in Spherical Symmetry . . . . .	142
<b>9</b>	<b>Future prospects</b>	<b>145</b>



# Chapter 1

## Introduction

Cosmology is the branch of physical sciences that studies the universe as a single physical system. Over the course of history the origin and fate of the universe have stimulated the minds of great thinkers, however it is only at the beginning of the 20th century that cosmology has emerged as a scientific discipline. In the last hundred years we have gathered an impressive amount of information on the properties of our universe. Our understanding of what we observe has improved along with the quality of the data, thanks to great theoretical advancements. Nowadays, we have a standard cosmological model that fits very well the data: the so called  $\Lambda$ CDM model. It is also called the concordance model, since a set of redundant observational tests agree very well on the values of its parameters. Nevertheless, this model remains problematic since it relies on the existence of two “dark” components: Dark Matter and Dark Energy, the latter being identified with the cosmological constant  $\Lambda$  of the Einstein equations of General Relativity (GR). The cosmological community is nowadays mostly devoted to understand these mysterious components, both theoretically and observationally. This thesis finds its place in this effort: making use of numerical techniques we will bridge theoretical models of dark energy to observations of the large scale structure of the universe.

In this first chapter we will put the work of this thesis in a historical perspective: we will outline the history of 20th century cosmology in §1.1 and discuss the problems left open in §1.2, where we will present the main unknowns of cosmological theories today: Dark Matter and Dark Energy.

## 1.1 A brief history of modern Cosmology

In the first half of the 20th century the emergence of two new physical theories revolutionised the way we think about our Universe. Einstein's relativity theory defined a new framework for the study of gravitational interactions while Quantum Field Theory (QFT) emerged as the framework to describe electromagnetism and subsequently the weak and strong nuclear forces which were later discovered. Following Einstein's formulation of the theory of GR, it became clear that this could be used to study the universe as a whole, since at large scales gravity is the predominant force ruling the distribution of matter. The first cosmological model was in fact proposed by Einstein himself in 1917 [61]. It described a stationary universe filled with matter homogeneously and isotropically distributed. Homogeneity and isotropy constitute the so called Cosmological Principle: every observer sees the same properties of the universe when looking at it from different locations and in different directions. In this solution space has positive curvature and is thus closed, i.e. a 3-D sphere and is unstable since the self-gravitational attraction of matter leads the universe to collapse. Einstein proposed the introduction of a new term in the field equations, the cosmological constant  $\Lambda$ , that could stabilise his solution and achieve stationarity in the presence of matter. De Sitter published in 1917 a concurrent solution that described a static empty universe [57]. In this model galaxies are observed with a redshift, a prediction that later drew Hubble's attention to a cosmological explanation of his redshift-distance relation. In the following decade other solutions of the Einstein equations (with or without the cosmological constant term) were found by Friedmann [69, 70], Lemaître [100], Robertson [138] and Walker [181] independently, corresponding to expanding or contracting universes.

On the observational side, the pioneering observational programs by Shapley and Hubble used Cepheids for the first time to infer distances to other star systems [150], revealing not only that the Galaxy is much larger than previously thought [151], but also that there are other galaxies in our universe, at huge distances from our own [85]. In 1917, Slipher used spectroscopic observations of faint galaxies to measure the Doppler shift of their spectral lines [153]. Interpreting this shift to be due to the relative velocity between the observer and the source, he deduced unexpectedly high velocities for all the galaxies and observed that most of them were receding from the solar system. Wirtz suggested in 1922 that with a suitable averaging procedure it could be seen an approximately linear relation between redshift and apparent magnitude of galaxies [184], but it was only by combining Humanson's observations of redshifts with estimates of the distances to these galaxies that

Hubble was able to formulate the linear redshift-distance relation known as Hubble's law in 1929 [86]. Hubble also realised that he could use the distribution of galaxies to test the homogeneity assumption, which he found consistent with the observed magnitude distribution of catalogs of galaxies [87].

On its own, Hubble's law does not imply that the universe is expanding. In fact, as stated above, De Sitter's model predicted a red-shift in the frequency of light proportional to the distance of the source. The problem with this solution is that it holds only for matter densities very close to zero, a fact ruled out by updated estimates of the mass of the Galaxy. The apparent recession of galaxies can instead be the result of the expansion of space-time itself, as described by Lemaître in his work of 1927 [100]. The expansion of the universe was considered as an established fact by the early 1930s. At this point the cosmological constant term was discarded because unnecessary, and was later defined by Einstein himself as "very ugly" [62] since it introduces a logically independent additive constant in a theory of interactions, which is usually determined only by the strength of the interaction, i.e. a multiplicative constant.

Lemaître was probably the first to mention the possibility of a Big Bang, by describing the beginning of the universe as the "explosion" of an unstable quantum [101]. He pointed out that if we extrapolate the expansion back in time, we can get to a state where the entire energy of the universe is contained in a single quantum. At this scale, according to Heisenberg uncertainty principle, space and time do not make sense anymore, thus the fragmentation of this quantum can be thought as the beginning of the universe. In 1946 Gamow proposed the Big Bang Nucleosynthesis (BBN) model [73] for the formation of chemical elements in the early universe by neutron capture, starting from a sea of protons, neutrons, electrons and radiation. The model successfully predicted the abundances of Hydrogen and Helium but failed to get sensible results for heavier elements. It was later realised that there are no stable elements with atomic number 5 or 8, thus making neutron capture an inefficient mechanism to build elements beyond Lithium. Those elements can instead be created through chains of nuclear reactions in the interior of stars or in SuperNovae explosions [33].

Taking further the calculations of Gamow for the evolution of the early universe, Alpher and Herman predicted the existence of a cosmic black body radiation with temperature of  $\sim 5^\circ \text{K}$  [7]. The success of the Big Bang theory was then consolidated by the discovery of this so called Cosmic Microwave

Background (CMB) in the 1960s [125, 58]. By this time, cosmology was an increasingly observationally-driven discipline, while philosophical a-priori like the static nature of our universe were falling under the weight of observational evidences.

The first hint of the next puzzle in cosmology dates to the 1930s, when Zwicky observed that the radial velocities of galaxies in the Coma cluster are so large that galaxies should fly away from the cluster, since the gravitational attraction due to the visible mass of galaxies cannot keep the system bounded [191, 192]. Most of the astronomers at the time thought that this was to ascribe to some observational error. Although Zwicky under-estimated the visible mass of the cluster, the difference was still not sufficient to explain the observations. Further observational evidence of some form of “missing mass” came with the measurement of the rotation curve of stars in spiral galaxies. This resulted to be nearly flat up to very large radii. The first of such observations is the rotation curve of Andromeda published by Rubin and Ford in 1970 [139]. By the end of the 1970s most of the astronomers and cosmologists were convinced of the necessity of an invisible form of matter [see e.g. 67], that was called Dark Matter (DM), a name suggested by Zwicky himself in 1933 [191].

Despite the success of the Hot Big Bang model in describing the primordial universe, some inconsistencies with observations were concerning the cosmologists of that time. In fact, given the estimated age of the universe, only solutions with flat geometry can account for the presence of complex structures as we observe them. It is also possible to show that if the universe is very close to being flat today, it must have always been so to an extreme precision. On the other hand, even revised estimates of the matter energy density of the universe with the inclusion of DM accounted only for 20% of the total energy density of a flat universe [60, 122].

The flatness of the universe also raised some philosophical questions. The universe must in fact be born with a very peculiar value of its energy content, out of the infinite possibilities: the only value for which its geometry is flat. This concept is commonly referred to as “fine-tuning”, and it is recurrent in modern cosmology. In 1981 Guth presented his theory of inflation, where an accelerated phase of exponential expansion takes place in the very early universe [78]. If this phase lasted long enough, the extreme stretching of space-time can explain the fact that we observe a universe with a geometry very close to flat.

Inflation solved other problems of the Hot Big Bang model as well. The scale at which the homogeneity of the abundance of light elements is tested is much larger than the size of a causality-connected region (the horizon) of the universe at the time of BBN. The same argument can be made for the homogeneity of CMB radiation on scales much larger than the size of the horizon when it was emitted. The fact that regions that have never been in causal contact have the same density and are highly homogeneous requires again a fine-tuning of initial conditions to a very homogeneous state. During inflation, though, the horizon may have been expanded to scales that are much larger than the size of the horizon today, thus explaining the observed homogeneity on very large scales. Inflation also allows small quantum fluctuations to be stretched to macroscopic scales, thus seeding the formation of structures and leaving an imprint of the CMB photons.

The COBE satellite was launched in 1989 and carried an instrument to measure the spectrum of CMB (FIRAS) and another one to detect the predicted tiny temperature fluctuations of cosmological origin (DMR). The first-year data of DRM were released in 1992 [155] and showed the existence of temperature fluctuations of a part in  $10^5$  at large angular scales, thus opening the possibility to test inflationary models. The data from FIRAS showed with high accuracy the black body nature of CMB spectrum [110], confirming that CMB is of cosmological origin. Later CMB experiments were able to measure the power spectrum of temperature fluctuations with higher accuracy and down to smaller scales, yielding values of the spectral index in agreement with predictions of most inflationary models. COBE observations marked the beginning of what we now call “precision cosmology”: a data-driven discipline with a standard model which is robust to observational tests.

The last piece of the puzzle for the currently accepted cosmological model made its entrance in 1999, when two independent experiments announced having detected the evidence of an accelerated expansion at late times, which is still ongoing [135, 128]. The observations were measurements of the apparent magnitude of SuperNova events of type Ia. In a similar way of Cepheids, this type of SuperNovæ can be calibrated to yield an estimate of their distance, thus probing the redshift-distance relation. They are much brighter than Cepheids, allowing to probe the relation up to higher redshifts. Solutions of the Einstein equations for a universe composed of matter and radiation cannot have an accelerated expansion rate. Nonetheless, the acceleration can be explained by re-introducing the cosmological constant term in the Einstein equations and adjusting the value of its energy density to

account for the missing energy to make the universe flat. This solution raises again physical and epistemological problems which we will discuss in some details in §1.2.2. The year after, balloon CMB experiments provided a strong evidence for the spatial flatness of the universe [55, 80].

## 1.2 State-of-the-art Cosmology

The Hot Big Bang model, together with the theory of inflation, provides a successful theoretical framework in which to interpret observations. As we have seen in the previous section the 20th century has left us with two big mysteries to solve: the “missing mass” problem and the acceleration problem. The solution to the first one is sought in particle physics models, since new particle types that do not interact with the Standard Model sector if not through gravitational forces can explain the lack of visible mass. The mass of these particles determines the behaviour of density perturbations in the DM component and has important implications for the growth of structures in our universe, as we will see in Chapter 3. We will briefly describe the phenomenological classification of DM candidates in the next section. The solution to the acceleration problem is on the other hand more complicated to tackle. As already mentioned the cosmological constant solution raises many questions, making it an unsatisfying solution. In recent years a great number of alternative models to account for the observed accelerated expansion have been proposed. They can mainly fit into two broad categories: Dark Energy models and Modified Gravity models. In the first category the acceleration is driven by a new component that contributes to the stress-energy tensor (i.e. the right-hand side of the Einstein equation), while the second kind of models modifies the theory of gravity by extending General Relativity. We will present the problems of the Cosmological Constant solution and the motivations for alternative solutions in §1.2.2.

### 1.2.1 Dark Matter

The common assumption of most DM models is that DM particles have been in thermal equilibrium with the other components in the early universe, allowing to use the Boltzmann equation to make predictions on their cosmological evolution. Thermal DM can be classified as Cold or Hot Dark Matter (CDM or HDM), depending on whether particles were relativistic at the time they decoupled from the other components. There are models of non-thermal DM, like monopoles, axions and cosmic strings, but there is no general treatment for this type of DM.

The property of DM particle candidates that is most relevant for cosmology is their mass. In fact, more massive particles become non-relativistic earlier in the history of the universe and have a larger clustering strength. This affects the growth of structures, as we will see in §3.2. Particles with mass  $m_{DM} \gtrsim 1$  eV become non-relativistic before decoupling and lead to a structure formation scenario which significantly differs from that of lighter particles that become non-relativistic later, such as massive neutrinos, which are HDM candidates. Perturbations in HDM density are quickly erased due to the high velocity dispersion of particles while they are still relativistic, determining the scale of the first structure to collapse in HDM dominated cosmologies (see §3.2). These cosmologies are currently ruled out by observations since they predict a structure formation history that starts at the scales of clusters of galaxies, that then host the formation of smaller structures. This is contradicted by the presence of galaxies up to very high redshifts, which would not have had the time to form in HDM cosmologies. The recent experimental confirmation of the non-zero mass of neutrinos [160, 161], together with upper bounds coming from cosmological observations [104], indicate that a small fraction of HDM should nevertheless be taken into account to yield accurate results on the growth of structures.

CDM scenarios are the standard in present day cosmology. They are not exempt of problems though. The leading particle candidates are the so called Weakly Interacting Massive Particles (WIMPs), but direct searches with particle colliders or underground experiments are not succeeding in agreeing on any new particle detection. Moreover, numerical simulations of structure formation in  $\Lambda$ CDM scenarios show clustering properties at small scales which differ significantly from the observed ones [117, 95, 31]. In particular, the abundance of small structures in such simulations does not agree with observations of the Milky Way satellites.

A Warm Dark Matter scenario has also been proposed, motivated by sterile neutrino models. This kind of particles have intermediate velocity dispersion between CDM and HDM, which allows to form less small structures than in CDM and at least alleviate the discrepancy with observations. This kind of particles, though, are strongly constrained by observations of high redshift Lyman- $\alpha$  forest measurements, which seem to rule out most of WDM candidates that would solve the small scale problems of CDM [8].

The missing mass problem is far from being solved, but a number of efforts are ongoing in order to shed light on this elusive form of matter. Direct

search experiments are exploring larger areas of the parameter space, while further observational investigations of local group galaxies can exclude the statistical improbability of the Milky Way as an explanation for the missing satellites problem. On the theoretical side many alternative models, like Self-Interacting Dark Matter (SIDM) [158] or Late-Forming Dark Matter (LFDm) [53], are being proposed and their predictions on structure abundances are being computed thanks to numerical simulations [180, 4].

### 1.2.2 Dark Energy

Adding the cosmological constant  $\Lambda$  term to the Einstein equations yields a solution that fits all current observational data. Physically, it corresponds to the introduction of a component with constant energy density and negative pressure. When this component dominates the energy budget of the universe, the negative pressure acts repulsively on space-time, driving the acceleration of the expansion. It has a characteristic value of the ratio between pressure and energy density of  $w = P_\Lambda/\rho_\Lambda = -1$ , and the value of the energy density inferred from observations is:

$$\rho_\Lambda c^2 \simeq (3 \times 10^{-3} \text{eV})^4. \quad (1.1)$$

Lemaître has been the first to propose that the cosmological constant term can be interpreted as the gravitating energy of the vacuum [102]. This idea was independently developed decades later by Sakharov and Zel'dovich on the basis of QFT [141, 188]. In quantum field theory the vacuum is not empty, but it is permeated by a sea of virtual particles that are continuously created and annihilated. As a consequence, the energy of the vacuum is not zero and according to General Relativity it should gravitate. An attempt to evaluate this energy by computing the contribution of all possible virtual particles gives enormous values. The contribution of the electron alone would amount to  $(5 \times 10^5 \text{eV})^4$ . Explaining why the measured value of the cosmological constant is so small compared to the value expected from quantum field theory considerations poses an unprecedented fine-tuning problem: in fact it would require a staggering precise cancellation of quantum-vacuum diagrams. This would be possible if a symmetry enforcing the cancellation to be exact (no vacuum energy) is spontaneously broken such that vacuum energy is non-zero but small. This consideration has led to the formulation of supersymmetric models, in which contributions to the vacuum energy from bosons and fermions exactly cancel because of the symmetry. The supersymmetric models that could solve the fine-tuning problem though are currently ruled out by particle colliders experiments.

Another approach to the cosmological constant problem could be to consider  $\Lambda$  as a constant of nature, like the gravitational constant  $G$ . As already stated above Einstein himself found this solution unappealing, since this would be the only additive constant of nature involved in a theory of interactions. This is as if at cosmological scale gravitational dynamics was ruled by  $\Lambda$ , while locally gravitational interactions were determined by their strength  $G$ . Moreover, fine-tuning of the value of  $\Lambda$  is necessary to achieve the level of clustering of structures that we currently observe.

Cosmological observations agree very well with a cosmological constant [129], but the problems here exposed motivated many to propose alternative models to explain the acceleration, and their predictions are being tested against observations. Given that the moment in which dark energy influences the most the evolution of the universe is at late times, CMB observations are rather insensitive to the details of the competing Dark Energy or Modified Gravity models. This is why a lot of efforts are going towards making predictions for these models in the non-linear regime, in order to compare predictions of the large scale structure of the universe with data of large volume galaxy surveys. It is in the context of this effort that the work of this thesis is framed.

### 1.3 Plan of the thesis

The thesis is divided in three parts. The first part introduces cosmological and structure formation models as well as numerical simulations. We will begin by reviewing the standard cosmological model and some of its extensions in Chapter 2. We will then apply these results to structure formation models: in Chapter 3 we will review the solutions of these models in the linear regime, where they can be obtained analytically, while in Chapter 4 we will present some numerical methods to study structure formation in the non-linear regime.

The second part concerns some cosmological applications of large galaxy surveys. In particular we will concentrate on the matter power spectrum observable, which is at the basis of many large scale structure observables, and we will model its estimator in the non-linear regime of gravitational collapse using N-body simulations. In Chapter 5 we will introduce the observables of interest for this thesis and the statistical tools used to infer cosmological parameters from observations. In Chapter 6 we will study the non-linear effects on the matter power spectrum covariance matrix using a large set of

N-body simulations. We will concentrate on numerical systematics related to the mass resolution of the simulations and propose an empirical statistical correction for the covariance. The work presented in this Chapter has been published in Ref. [26]. In Chapter 7 we will study the errors associated to the estimation of the covariance and its inverse, the precision matrix, using large samples of N-body simulations and we will show how these errors impact the estimation of cosmological parameters. Moreover, using the Fisher matrix technique we will confirm that non-linearities in the covariance induce larger errors on the cosmological parameters with respect to those obtained in the linear approximation. The content of this Chapter is the result of a collaboration with Thomas Kitching and Luca Amendola and will be submitted for publication in the next months [27].

The third part of the thesis is dedicated to numerical methods for simulations of clustering dark energy cosmologies. In particular we will describe in Chapter 8 Godunov hydrodynamical methods for dark fluids characterised by a constant equation of state parameter and speed of sound. These methods will be presented in Ref. [46] that will be submitted for publication in the next months together with a companion paper on the spherical collapse of DM in presence of DE perturbations [25]. We will conclude in Chapter 9 with an outline of future prospects of the work presented in this thesis.

Part I  
Theoretical Cosmology



# Chapter 2

## Cosmological models

In this chapter we present the basic equations describing the evolution of our universe in the framework of General Relativity. The chapter is structured as follows: in §2.1 we introduce various definition of distances in cosmology and we discuss Hubble's law in §2.2, then in §2.3 we describe the Hot Big Bang model which forms the basis upon which the current cosmological model is built. The Einstein-de Sitter model, for which it is possible to find analytical solutions, is presented in §2.4 while the  $\Lambda$ CDM standard model is discussed in §2.5. We close this chapter with an overview of the Dark Energy models that are relevant to this thesis in §2.6.

### 2.1 Distances in cosmology

Assuming the Cosmological Principle the distance between two points in an expanding space-time is given by the Friedmann-Lemaître-Robertson-Walker (FLRW) metric, which in polar coordinates  $(\varrho, \theta, \varphi)$  reads:

$$ds^2 = g_{\alpha\beta} dx^\alpha dx^\beta = (c dt)^2 - a(t)^2 \left[ \frac{dr^2}{1 - kr^2} + r^2 (d\theta^2 + \sin^2 \theta d\varphi^2) \right], \quad (2.1)$$

where  $\varrho = a(t) r$ ,  $a(t)$  is the expansion factor and  $k$  is the curvature parameter that takes values of  $-1$ ,  $0$  and  $1$  for an open, flat and closed geometry respectively.

In cosmology it is possible to define various types of distance, depending on how the cosmic distance is measured. We will in general be interested in measuring the distance from an observer located at the origin of the spatial coordinate system to a source located at  $(a r, 0, 0)$ . By combining measurements of two or more types of distances for the same object it is possible to infer constraints on the geometry and expansion of the universe.

## Proper and comoving distances

We can define the proper distance between two points in space-time as the distance measured at a fixed time. It is defined as:

$$d_p \equiv \int_0^r \frac{a \, dr}{(1 - k r^2)^{1/2}} = a f(r), \quad (2.2)$$

where:

$$f(r) = \begin{cases} \arcsin r & \text{if } k = 1 \\ r & \text{if } k = 0 \\ \operatorname{arcsinh} r & \text{if } k = -1. \end{cases} \quad (2.3)$$

The proper distance measured today is called comoving distance:

$$d_c = \frac{a_0}{a(t)} d_p, \quad (2.4)$$

where  $a_0$  is the expansion factor today.

## Redshift

The redshift of a light source is defined as the relative change of wavelength that a photon emitted from the source at time  $t_e$  has experienced because of the expansion, when it reaches an observer at time  $t_0$ :

$$z \equiv \frac{\lambda_0 - \lambda_e}{\lambda_e}, \quad (2.5)$$

where  $\lambda_e$  and  $\lambda_0$  are the wavelengths of the photon at emission and observation time respectively. Since photons travel along null geodesics from the source to the observer, the comoving distance traveled by the photon is given by:

$$\int_{t_e}^{t_0} \frac{c \, dt}{a(t)} = \int_0^r \frac{dr}{(1 - k r^2)^{1/2}} = f(r). \quad (2.6)$$

If a second photon is emitted after a time  $\delta t_e$ , the distance traveled by the second photon would be:

$$\int_{t_e + \delta t_e}^{t_0 + \delta t_0} \frac{c \, dt}{a(t)} = \int_{t_e}^{t_0} \frac{c \, dt}{a(t)} = f(r). \quad (2.7)$$

By subtracting the two integrals we get:

$$\int_{t_0}^{t_0 + \delta t_0} \frac{c \, dt}{a(t)} = \int_{t_e}^{t_e + \delta t_e} \frac{c \, dt}{a(t)}, \quad (2.8)$$

If the time between the emission of the two photons is a wave period  $\delta t_e = 1/\nu_e$ , which is much smaller than the characteristic time-scale of the expansion, we can consider  $a$  as constant in time and integrate Eq.(2.8) to:

$$\nu_0 a_0 = \nu_e a_e. \quad (2.9)$$

From this we can derive the relation between redshift and the expansion factor:

$$1 + z = \frac{a_0}{a_e}. \quad (2.10)$$

### Luminosity distance

The luminosity distance  $d_L$  is defined through the relation:

$$l_0 \equiv \frac{L}{4\pi d_L^2}, \quad (2.11)$$

where  $l_0$  is the apparent luminosity of a source with absolute luminosity  $L$ , or equivalently the flux received by an observer at time  $t_0$ . The area of a sphere centred on the source and passing through the observer at time  $t_0$  is  $4\pi a_0^2 r^2$ . The absolute luminosity is the energy emitted by the source in a time  $\delta t$ . By the time photons reach the observer, their frequency has been redshifted by a factor  $a/a_0$  and the time interval has been spread to  $\delta t_0 = a_0/a \delta t$ , so Eq.(2.11) can be written as:

$$l_0 = \frac{L}{4\pi a_0^2 r^2} \left( \frac{a}{a_0} \right)^2, \quad (2.12)$$

from which we can read:

$$d_L = a_0^2 \frac{r}{a} = a_0 (1 + z) r. \quad (2.13)$$

### Angular diameter distance

The angular diameter distance  $d_A$  is defined as the ratio of the proper diameter of a source  $D_p$  and the angle  $\Delta\theta$  under which it is seen by an observer:

$$d_A \equiv \frac{D_p}{\Delta\theta}. \quad (2.14)$$

The proper diameter is found by integrating the metric Eq.(2.1) with  $dt = dr = d\varphi = 0$  and is given by:

$$D_p = a r \Delta\theta, \quad (2.15)$$

from which we read:

$$d_A = a r = \frac{d_L}{(1+z)^2}, \quad (2.16)$$

where the last equality is a consequence of Eq.(2.13). Notice that for a flat universe  $d_A = d_p$ .

## 2.2 Hubble's law

By deriving Eq.(2.2) with respect to time we get the apparent radial recession velocity of an object at distance  $d_p$  from the observer due to the expansion of space-time:

$$v_H = \dot{a} f(r) = \frac{\dot{a}}{a} d_p = H d_p, \quad (2.17)$$

which is usually called Hubble flow. Here  $H = \dot{a}/a$  is the Hubble parameter. If the observer is at time  $t_0$  we get the Hubble law:

$$v = H_0 d_c. \quad (2.18)$$

Notice that Hubble in 1929 derived this law using the luminosity distance of Cepheids and redshift as a proxy for velocity, but for small redshifts it can be shown that the relation  $c z \simeq H_0 d_L$  holds. This can be seen by expanding  $a(t)$  in a Taylor series around  $a_0$ :

$$a(t) = a_0 \left[ 1 + H_0(t - t_0) - \frac{1}{2} H_0^2 q_0 (t - t_0)^2 + \dots \right], \quad (2.19)$$

where  $q$  is the deceleration parameter:

$$q \equiv -\frac{\ddot{a} a}{\dot{a}^2}. \quad (2.20)$$

Using Eq.(2.10) we get an expansion for  $z$ :

$$z(t) = H_0 (t - t_0) + \left(1 + \frac{q_0}{2}\right) H_0^2 (t - t_0)^2 + \dots \quad (2.21)$$

For a photon the integration of the metric gives:

$$\frac{c}{a_0} \int_t^{t_0} (1 + z(t)) dt = f(r). \quad (2.22)$$

Using Eq.(2.21) and expanding  $f(r)$  around  $r = 0$  we get to:

$$r = \frac{c}{a_0 H_0} \left( z - \frac{1}{2} (1 + q_0) z^2 + \dots \right), \quad (2.23)$$

from which we can derive:

$$d_L = a_0^2 \frac{r}{a} \simeq \frac{c}{H_0} \left( z + \frac{1}{2}(1 - q_0)z^2 + \dots \right). \quad (2.24)$$

At first order we recover the Hubble law for the luminosity distance  $d_L = v/H_0$ , where  $v = cz$  is the apparent recession velocity.

## 2.3 Hot Big Bang model

The equations that describe the evolution of a relativistic system are the Einstein equations:

$$R_{\alpha\beta} - \frac{1}{2}g_{\alpha\beta}R = \frac{8\pi G}{c^4}T_{\alpha\beta}, \quad (2.25)$$

where  $\alpha, \beta = \{0, 1, 2, 3\}$  indicate time and space components,  $R_{\alpha\beta}$  is the Ricci curvature tensor,  $R$  is the scalar curvature,  $g_{\alpha\beta}$  is the metric tensor,  $c$  is the speed of light,  $G$  is the gravitational constant and  $T_{\alpha\beta}$  is the stress-energy tensor. Assuming homogeneity and isotropy,  $T_{\alpha\beta}$  has two degrees of freedom: the energy density  $\rho c^2$  and the pressure  $P$ , which depend only on time. It is in the form:

$$T_{\alpha\beta} = -P g_{\alpha\beta} + (P + \rho c^2)u_\alpha u_\beta, \quad (2.26)$$

where  $u$  is the 4-velocity of a comoving element of the fluid as viewed from an observer in a local inertial reference system. If we introduce the cosmological constant term  $\Lambda$  the Einstein equations read:

$$R_{\alpha\beta} - \frac{1}{2}g_{\alpha\beta}R - \Lambda g_{\alpha\beta} = \frac{8\pi G}{c^4}T_{\alpha\beta}. \quad (2.27)$$

The contribution of  $\Lambda$  can be incorporated into the stress-energy tensor:

$$\tilde{T}_{\alpha\beta} = T_{\alpha\beta} + \frac{\Lambda c^4}{8\pi G} g_{\alpha\beta} \quad (2.28)$$

and the corresponding pressure and density are:

$$\tilde{P} = P - \frac{\Lambda c^4}{8\pi G}, \quad (2.29)$$

$$\tilde{\rho} = \rho + \frac{\Lambda c^2}{8\pi G}. \quad (2.30)$$

As we will see later, the negative term on the right-hand side of Eq.(2.29) can account for the observed accelerated expansion.

It is reasonable to treat the universe as an isolated system and assume that the expansion is adiabatic. In this case we have the condition:

$$dU = -P dV, \quad (2.31)$$

where  $U$  is the internal energy and  $V$  is the volume. If we assume that the internal energy is dominated by the mass energy then this condition can be written as:

$$d(\rho c^2 a^3) = -P da^3. \quad (2.32)$$

The Einstein equations for the FLRW metric (2.1) with these assumptions can be written as:

$$\dot{a}^2 + k c^2 = \frac{8\pi G}{3} \rho a^2, \quad (2.33)$$

$$\ddot{a} = -\frac{4\pi G}{3} \left( \rho + \frac{3P}{c^2} \right) a, \quad (2.34)$$

which are called the Friedmann equations. These are not completely independent, but one can be recovered from the other using Eq.(2.32). From Eq.(2.33) we can see that there is a critical density for which the universe is flat that is given by:

$$\rho_{crit} \equiv \frac{3 H^2}{8 \pi G}, \quad (2.35)$$

so that if the total density is  $\rho_{tot} > \rho_{crit}$  the universe is spatially closed while if  $\rho_{tot} < \rho_{crit}$  it is spatially open. Using this definition we can construct the dimensionless density parameter :

$$\Omega = \rho / \rho_{crit}. \quad (2.36)$$

The system of Friedmann equations is closed by adding the equation of state (EoS) that relates pressure and density of the fluid. If we consider the universe as composed of matter, described as a perfect fluid, and radiation we can write:

$$P_{tot} = P_m + P_r = \frac{\rho_m c^2 k_B T}{m_p c^2} + \frac{1}{3} \rho_r c^2, \quad (2.37)$$

where  $k_B$  is the Boltzmann constant and the subscripts  $m$  and  $r$  indicate matter and radiation respectively. Since the thermal energy of matter is negligible compared to its mass energy, we can approximate  $P_m \simeq 0$ . We can thus write a generic EoS in the form:

$$P = w \rho c^2, \quad (2.38)$$

where  $w$  is called the EoS parameter and takes the values of 0, 1/3 and  $-1$  for matter, radiation and cosmological constant respectively. Note that relativistic matter has the same EoS of radiation. It is possible to define an adiabatic speed of sound:

$$c_{sA}^2 = \left( \frac{\partial P}{\partial \rho} \right)_S = w c^2, \quad (2.39)$$

where the subscript  $S$  means at constant entropy. By requiring that  $0 \leq c_{sA} \leq c$  we get a condition on the EoS parameter  $0 \leq w \leq 1$  that is called the Zel'dovich interval.

Substituting Eq.(2.38) into Eq.(2.34) we obtain:

$$\ddot{a} = -\frac{4\pi G}{3} \rho (1 + 3w) a. \quad (2.40)$$

We can see that in the Zel'dovich interval the universe is always decelerating. The cosmological constant has an EoS that is not in this interval and can in fact change the sign of the deceleration parameter  $q$ . We can see this by considering a universe composed of matter and cosmological constant (as we will see in §2.5 these are the only relevant components in the epoch when  $q$  changes sign) and compute the deceleration parameter Eq.(2.20) as:

$$q = \frac{\ddot{a}}{a H^2} = \left( \frac{4}{3} \pi G \rho_m - \frac{\Lambda c^2}{3} \right) \frac{1}{H^2} = \frac{1}{2} \Omega_m - \Omega_\Lambda. \quad (2.41)$$

If  $\Omega_{\Lambda,0} > \frac{1}{2} \Omega_{m,0}$  the present expansion of the universe is accelerated.

### 2.3.1 Big Bang singularity

Substituting Eq.(2.38) into Eq.(2.32) we find the evolution of density with respect to the scale factor:

$$\rho = \rho_0 \left( \frac{a_0}{a} \right)^{3(1+w)}. \quad (2.42)$$

From this it is clear that for  $w > -1$  if we extrapolate the expansion back in time  $a \rightarrow 0$ , the density grows towards a singularity  $\rho \rightarrow \infty$ . The way in which the density approaches the singularity depends on the function  $a(t)$ : if  $w > -\frac{1}{3}$ ,  $a(t)$  is a monotonically increasing concave down function so the singularity is reached in a finite time in the past. An accelerating phase could help avoiding such singularity but as we will see in §2.5 the estimated value of the cosmological constant today indicates that the current accelerated phase started not long ago, so it is not effective in removing the Big Bang singularity from the model.

### 2.3.2 Cosmological horizons

Given that light has a finite speed, if the universe is finite in time there can be a maximum distance that a photon can travel. In particular, if the universe is finite in the past the maximum distance that a photon can have traveled at a given time  $t$  is:

$$R_H(t) = a(t) \int_0^t \frac{c dt}{a(t)}, \quad (2.43)$$

which is called the particle horizon, or simply the horizon. This can be thought of as the radius of the sphere enclosing all events that have been in causal contact with us. We can also define an event horizon, that represents the region of space that will come in causal contact with us in the future:

$$R_e(t) = a(t) \int_t^\infty \frac{c dt}{a(t)}. \quad (2.44)$$

For models in which  $a$  grows faster than  $t$  this quantity is finite.

### 2.3.3 Thermal history of the universe

From Eq.(2.42) we see that  $\rho_r$  evolves more rapidly with  $a$  than  $\rho_m$ . Since today we observe that  $\rho_{r,0} \ll \rho_{m,0}$  (see §2.5), there is a moment in the past when the two components had the same energy density. This moment is called equivalence and is estimated to be of the order of  $z_{eq} \simeq 5 \cdot 10^3$ . Before equivalence, the energy density of radiation was dominating the energy budget of the universe, thus driving the evolution of  $a(t)$ . This period is thus called the radiation era, while the one after equivalence is called the matter dominated era.

Today, the characteristic time between two collisions of photons with matter particles is much longer than the characteristic time of the expansion, so matter and radiation components are not in thermal equilibrium. This condition can be written as:

$$\tau_{coll} \simeq \frac{1}{n \sigma_T c} \gg \tau_{exp} \simeq \frac{1}{H_0}, \quad (2.45)$$

where  $n$  is the mean number density of matter particles and  $\sigma_T$  is the Thomson scattering cross-section. In all viable cosmologies  $\tau_{coll}$  evolves more rapidly than  $\tau_{exp}$ , so we can find a redshift in the past where matter and radiation were in thermal equilibrium. This redshift is estimated to  $z_{dec} \simeq 10^3$ , where  $dec$  stands for decoupling, and is in general  $z_{dec} < z_{eq}$ , so that decoupling happens during matter era.

From Eq.(2.31) we can derive the scaling of the temperature of matter and radiation with respect to the scale factor. For the matter component this gives:

$$d \left( \rho_m c^2 a^3 + \frac{3}{2} \frac{\rho_m}{m_p} k_B T_m a^3 \right) = - \frac{\rho_m}{m_p} k_B T_m da^3, \quad \text{thus:} \quad (2.46)$$

$$T_m = T_{m,0} \left( \frac{a_0}{a} \right)^2. \quad (2.47)$$

For the radiation component, if we approximate its spectrum to a black body, the energy density is  $\rho_r c^2 = \sigma_{SB} T^4$ , where  $\sigma_{SB}$  is the Stephan-Boltzmann constant. Thus:

$$d \left( \sigma_{SB} T_r^4 a^3 \right) = - \frac{1}{3} \sigma_{SB} T_r^4 da^3 \quad (2.48)$$

$$\text{and } T_r = T_{r,0} \left( \frac{a_0}{a} \right). \quad (2.49)$$

After decoupling the temperature of the two components evolves independently following these scalings. Before decoupling the two fluids were tightly coupled by electromagnetic interactions and had a common temperature  $T$ , whose evolution can again be recovered from the adiabatic condition:

$$d \left( \rho_m c^2 a^3 + \frac{3}{2} \frac{\rho_m}{m_p} k_B T a^3 + \sigma_{SB} T^4 a^3 \right) = - \left( \frac{\rho_m}{m_p} k_B T + \frac{1}{3} \sigma_{SB} T^4 \right) da^3. \quad (2.50)$$

Defining the dimensionless quantity

$$\sigma_{rad} \equiv \frac{4 m_p \sigma_{SB} T^3}{3 k_B \rho_m} \quad (2.51)$$

we can simplify Eq.(2.50) as:

$$\frac{dT}{T} = - \frac{da}{a} \left( \frac{1 + \sigma_{rad}}{\frac{1}{2} + \sigma_{rad}} \right). \quad (2.52)$$

We can compute the value of  $\sigma_{rad}$  after decoupling by using  $T = T_r$ :

$$\sigma_{rad}(t) \propto \frac{T_r^3}{\rho_m} = \text{const.} = \sigma_{rad,0}, \quad (2.53)$$

which is estimated to  $\sigma_{rad,0} = 1,35 \cdot 10^8 (\Omega_{m,0} h^2)^{-1}$ , where  $h$  is the value of the Hubble parameter today normalised to  $100 \text{ km s}^{-1} \text{ Mpc}^{-1}$ . Knowing that at decoupling  $\sigma_{rad} \gg 1$  Eq.(2.52) can be integrated to obtain:

$$T \propto a^{-1}, \quad (2.54)$$

so the universe before decoupling behaves like a radiation universe.

The temperature of the universe also determines the matter constituents. At the beginning of the matter era, temperatures are so high that all the atoms are fully ionised. As the temperature drops, the interactions between photons and electrons become less frequent and the electrons start to combine with protons to make Hydrogen atoms. The time between the first combination and the moment in which Hydrogen is completely neutral is called recombination. The drop in density of free electrons makes the Thomson scattering inefficient and photons are almost completely free to travel through the mainly empty space. This sea of photons released at decoupling is what we observe today as the CMB. As soon as the first stars start forming their surroundings are re-ionised by the emitted radiation and part of the CMB photons are re-absorbed. In fact, CMB observations can provide constraints on the optical depth of the medium at the time of re-ionisation.

At the beginning of the radiation era, temperature is above the threshold that triggers nuclear reactions. The efficient reactions in this era are the  $p + \alpha$  and the  $\alpha + \alpha$  reactions, where  $p$  is a proton and  $\alpha$  is a  $^4\text{Helium}$  nucleus. Since stable elements with atomic number of 5 or 8 do not exist, only elements lighter than  $^7\text{Li}$  are formed. In fact, density in this era is not high enough for unstable  $^8\text{Be}$  atoms to efficiently combine with  $\alpha$  particles to form  $^{12}\text{C}$  atoms. This process is called Big Bang Nucleosynthesis and is supported by observations of the abundance of Hydrogen and Helium. In particular, the abundance of Helium today is too high to be explained by nucleosynthesis in the interior of stars. There is though a problem with the prediction of the abundance of  $^7\text{Li}$ , which yields values three times higher than the measured ones (but see [130]).

Going further back in time, the temperature of the universe can reach a value  $T_x$  where:

$$k_B T_x = 2 m_x c^2, \quad (2.55)$$

where  $m_x$  is the mass of a given particle type  $x$ , for example electrons. Above this temperature a significant amount of couples  $e^+ e^-$  are created, and similarly at higher temperatures couples of heavier leptons, then hadrons and quarks are created. The following eras are defined:

- Lepton era:  $k_B T_e = 0,5 \text{ MeV} < k_B T < k_B T_\pi = 130 \text{ MeV}$
- Hadron era:  $k_B T_\pi < k_B T < 200 - 300 \text{ MeV}$
- Quark era:  $k_B T > 200 - 300 \text{ MeV}$

## 2.4 Einstein–de Sitter universe

The Einstein–de Sitter (EdS) model describes a flat universe without cosmological constant. In this model the Friedmann equations for a single component can be integrated analytically. We will review here the main results because as we will see in §2.5 these results can be used to approximate the evolution of the universe at given epochs.

Let us rewrite Eq.(2.33) in different forms that will be useful in the following. By dividing Eq.(2.33) by  $a_0$  and evaluating it today we get:

$$H_0^2 (1 - \Omega_0) = -\frac{k c^2}{a_0^2}. \quad (2.56)$$

By inserting this expression for  $k c^2/a_0^2$  into Eq.(2.33) we get:

$$\left(\frac{\dot{a}}{a_0}\right)^2 = H_0^2 \left[1 - \Omega_0 + \Omega_0 \left(\frac{a_0}{a}\right)^{3w+1}\right]. \quad (2.57)$$

which can be re-casted as an evolution equation for the Hubble parameter by dividing it by  $(a/a_0)^2$ :

$$H^2 = H_0^2 \left(\frac{a_0}{a}\right)^2 \left[1 - \Omega_0 + \Omega_0 \left(\frac{a_0}{a}\right)^{3w+1}\right] \quad (2.58)$$

In the EdS model  $\Omega_0 = 1$  so Eq.(2.57) gives:

$$\dot{a} = a_0 H_0 \left(\frac{a_0}{a}\right)^{\frac{1+3w}{2}}, \quad (2.59)$$

which once integrated yields:

$$a = a_0 \left(\frac{t}{t_0}\right)^{\frac{2}{3(1+w)}}. \quad (2.60)$$

The Hubble parameter evolves in time as:

$$H = \frac{1}{3(1+w)t}, \quad (2.61)$$

while the deceleration parameter turns out to be constant:

$$q = \frac{1+3w}{2}. \quad (2.62)$$

Combining Eq.(2.42) and Eq.(2.60) we can find the evolution of density:

$$\rho = \rho_0 \left( \frac{t}{t_0} \right)^{-2}, \quad (2.63)$$

but since  $\rho = \rho_c$  we can write:

$$\rho = \frac{1}{6(1+w)^2 \pi G t^2}. \quad (2.64)$$

The horizon evolves as:

$$R_H = \frac{w+1}{w+\frac{1}{3}} ct. \quad (2.65)$$

## 2.5 $\Lambda$ CDM scenario

The  $\Lambda$ CDM model describes a flat universe whose components are DM, baryonic matter, radiation and the cosmological constant. The relative abundances of such components in terms of energy density are given by the  $\Omega$  parameters (see Eq.(2.36)), that are measured today at  $\Omega_{0,DM} \simeq 0.27$ ,  $\Omega_{0,b} \simeq 0.05$ ,  $\Omega_{0,r} \simeq 5 \times 10^{-5}$  and  $\Omega_{0,\Lambda} \simeq 0.68$  [129]. These values determine the important epochs of the history of the universe. The dominant component today is the cosmological constant. It is possible to define a redshift of equivalence between matter and cosmological constant as:

$$\Omega_{0,\Lambda} = \Omega_{0,m}(1+z_\Lambda)^3 \quad (2.66)$$

where  $\Omega_{0,m} = \Omega_{0,DM} + \Omega_{0,b}$ , from which we get  $z_\Lambda \simeq 0.3$ . The deceleration parameter is measured today at  $q_0 \simeq -0.55$ , from SN Ia observations mainly, indicating that the universe is currently accelerating. From Eq.(2.41) we can find the redshift at which the acceleration started by requiring that  $q = 0$ , so:

$$\Omega_{0,m}(1+z_{acc})^3 = 2\Omega_{0,\Lambda} \quad (2.67)$$

from which we get  $z_{acc} \simeq 0,6$ . The redshift of equivalence is instead given by:

$$\Omega_{0,m}(1+z_{eq})^3 = \Omega_{0,r}(1+z_{eq})^4, \quad (2.68)$$

from which we get  $z_{eq} \simeq 6400$ . If we consider a time well inside the matter era  $6400 \ll z \ll 0.3$ , the universe can be described by an Einstein-de Sitter universe filled with matter. Similarly, well inside the radiation era the evolution of the universe is well described by an Einstein-de Sitter universe filled with radiation. Near the transitions  $z_{eq}$  and  $z_\Lambda$  both components (matter

and radiation and matter and cosmological constant respectively) contribute with similar importance, so two components models have to be used to compute the relevant quantities.

The  $\Lambda$ CDM model is specified by 6 independent parameters  $\{H_0, \Omega_b, \Omega_m, n_s, A_s, \tau\}$ , where  $A_s$  and  $n_s$  are the spectral parameters (see §3.1) and  $\tau$  is the optical depth of re-ionisation. All the other parameters can be derived from this set. This model is also called the “concordance” model, since a wealth of observational evidences converge in a small region of the parameter space. The main observables are the CMB power spectrum (see §3.1), the distance-redshift relation probed by standard candles, the Baryon Acoustic Oscillations (BAO, see §5.2) and the cluster mass function (see §3.1). In particular, the Hubble parameter is directly probed by the redshift-distance relation and it is measured to be  $H_0 = 73.8 \pm 2.4 \text{ km s}^{-1} \text{ Mpc}^{-1}$  [136]. There is currently a tension between this value and the inferred value of  $H_0$  from CMB data of the Planck satellite, which gives  $H_0 = 67.4 \pm 1.4 \text{ km s}^{-1} \text{ Mpc}^{-1}$  [129]. The inclusion of massive neutrinos could help reduce this tension [20] but the issue is not yet solved and will be the object of further investigation in the coming years.

## 2.6 Scalar field models of Dark Energy

The simplest models of Dark Energy are those in which the additional component is represented by a dynamical scalar field  $\varphi$  minimally coupled to gravity. We can in general write the action of a scalar field as:

$$\mathcal{S} = \int \mathcal{L}(X, \varphi) \sqrt{-g} d^4x, \quad (2.69)$$

where  $\sqrt{-g}$  is the determinant of the metric and  $\mathcal{L}$  is the Lagrangian, that is an arbitrary function of the field  $\varphi$  and the kinetic term:

$$X = \frac{g^{\mu\nu} \varphi_{,\mu} \varphi_{,\nu}}{2}. \quad (2.70)$$

Here the comma denotes a derivative, e.g.  $\varphi_{,\mu} = \partial_\mu \varphi$ . The stress energy tensor of the field is obtained by varying the action Eq.(2.69) with respect to  $g^{\mu\nu}$  and gives:

$$T_{\mu\nu} = \mathcal{L}_{,X} \varphi_{,\mu} \varphi_{,\nu} - \mathcal{L} g_{\mu\nu}. \quad (2.71)$$

It is possible to rewrite  $T_{\mu\nu}$  in the form of Eq.(2.26) by defining:

$$\rho = 2 X \mathcal{L}_{,X} - \mathcal{L}, \quad (2.72)$$

$$P = \mathcal{L}, \quad (2.73)$$

$$u_\mu = \frac{\varphi_{,\mu}}{\sqrt{2X}}. \quad (2.74)$$

The EoS parameter is thus:

$$w = \frac{\mathcal{L}}{2 X \mathcal{L}_{,X} - \mathcal{L}}. \quad (2.75)$$

For a generic Dark Energy model the acceleration Friedmann equation near the transition redshift  $z_{acc}$  can be written as:

$$\ddot{a} = -\frac{4\pi G}{3}(\rho_m + \rho_{DE} + 3P_{DE}) = -\frac{4\pi G}{3}(\rho_m + \rho_{DE}(1 + 3w)), \quad (2.76)$$

from which we can compute the deceleration parameter:

$$q = -\frac{\ddot{a}}{a H^2} = \frac{1}{2}(\Omega_m + \Omega_{DE}(1 + 3w)). \quad (2.77)$$

So the condition to get an accelerated solution is:

$$w < -\frac{1}{3\Omega_{DE}}(\Omega_{DE} + \Omega_m) \simeq -\frac{1}{3\Omega_{DE}}. \quad (2.78)$$

### 2.6.1 Quintessence

In quintessence models  $\varphi$  is a canonical scalar field with:

$$\mathcal{L}_\varphi = X + V(\varphi), \quad (2.79)$$

where  $V$  is the potential. In a flat space-time with FLRW metric Eq.(2.1) the variation of the action Eq.(2.69) with respect to  $\varphi$  gives:

$$\ddot{\varphi} + 3H\dot{\varphi} + \frac{dV}{d\varphi} = 0. \quad (2.80)$$

The stress-energy tensor is in this case:

$$T_{\mu\nu} = \varphi_{,\mu} \varphi_{,\nu} - \mathcal{L}_\varphi g_{\mu\nu}. \quad (2.81)$$

From this we can compute the two independent degrees of freedom:

$$\rho = T_0^0 = \frac{\dot{\varphi}^2}{2} + V(\varphi), \quad (2.82)$$

$$P = -T_i^i = \frac{\dot{\varphi}^2}{2} - V(\varphi), \quad (2.83)$$

from which we get:

$$w = \frac{\frac{\dot{\varphi}^2}{2} - V(\varphi)}{\frac{\dot{\varphi}^2}{2} + V(\varphi)}. \quad (2.84)$$

To get an EoS parameter  $w \simeq -1$  the field has to be slowly varying, i.e.  $\dot{\varphi}^2/2 \ll V(\varphi)$ . In general  $w$  can take any value between -1 and +1, and varies in time.

### 2.6.2 K-essence

In these models the accelerated phase is realised by the kinetic energy of the scalar field, which is a function of  $X$ . In this case the action is written as:

$$\mathcal{S} = \int P(X, \varphi) \sqrt{-g} d^4x, \quad (2.85)$$

where  $P(X, \varphi)$  corresponds to a pressure density and  $\rho = 2XP_{,X} - P$ . The EoS parameter is then:

$$w = \frac{P}{2XP_{,X} - P}, \quad (2.86)$$

from which we see that  $w \simeq -1$  if  $|2XP_{,X}| \ll |P|$ .



# Chapter 3

## Structure formation

In the previous Chapter we have derived relations that characterise a homogeneous and isotropic space-time. However, matter in the universe is only approximately homogeneously distributed. At small scale matter is clustered in stars and galaxies, while on the large scales and at early times deviations from homogeneity are small. The CMB reveals in fact that at the time of decoupling the universe was homogeneous up to a part on  $10^5$ , i.e. fluctuations of the density field were of the order of  $\delta \sim 10^{-5}$ .

The theory of gravitational instability of density perturbations was first formulated by Jeans in 1902 [89]: he showed that, if the effect of pressure is not able to oppose the tendency of over-densities to collapse under self-gravity, perturbations can grow in time. The scale over which fluctuations can grow is called Jeans length of the fluid. Jeans limited his analysis to a homogenous and static fluid, but Bonnor extended it to the case of an expanding background in 1957 [30]. This was further developed into a cosmological linear perturbation theory in the following years [see e.g. 152, 124]. In this framework the scaling of the Jeans length in time gives us information about the growth of structures in the different epochs of the history of the universe.

As already mentioned, density fluctuations are believed to be sourced by quantum fluctuations stretched to macroscopic scales during inflation. We will thus describe the fluctuations as a stochastic field, as outlined in §3.1, and follow the evolution of the density field with the Euler equations for an adiabatic fluid. We will first derive the evolution equations in linear regime in §3.2 followed by some insights on the evolution in non-linear regime and some approximated solutions in §3.3. We mainly follow Ref.s [43, 124] in this Chapter.

### 3.1 Statistical treatment of perturbations

The most generic quantity that describes a stochastic field is the joint probability density for the realisation of the field  $\phi$  at all points. This quantity can be represented as a functional  $p[\phi]$ , and allows us to define the expectation value of an observable  $f$  as:

$$\langle f \rangle = \int \mathcal{D}\phi p[\phi] f[\phi]. \quad (3.1)$$

This is an infinite-dimensional integral, but expectation values can be understood as the limit of a finite-dimensional average defined as:

$$\langle f \rangle = \int d^n\phi p(\phi_1, \dots, \phi_n) f(\phi_1, \dots, \phi_n) \quad (3.2)$$

over a large finite sample of the field. In the field formalism, the Cosmological Principle translates into the invariance of the density function under translation and rotation transformations.

The expectation values are not measurable unless we have access to several realisations of the field, which is obviously not the case in cosmology. We thus borrow a theorem from statistical physics, the ergodic theorem, to introduce an additional assumption. In cosmological context this theorem states that we can replace the ensemble averages with space averages over large volumes if the correlations of the field decay sufficiently rapidly in space. In other words: sufficiently large volumes of one realisation can be treated as independent realisations of the underlying field. This is why this assumption is often referred to as the fair sample hypothesis. Let us introduce at this point the concept of cosmic variance: since we can only access a finite volume of the universe with observations, we measure expectation values with a finite error. Analogously to sample variance for a finite number of realisations, cosmic variance can be seen as due to the finite volume of the observable universe.

The observable of interest for cosmology is in general the density fluctuation field:

$$\delta(\mathbf{x}) = \frac{\rho(\mathbf{x}) - \bar{\rho}}{\bar{\rho}}, \quad (3.3)$$

where  $\bar{\rho}$  is the mean density of the universe. In particular, we will be mainly interested in the  $N$ -point functions of the fluctuation field, i.e. the connected part of the  $N$ -point moments of  $\delta$ . Those can be defined using the generating

function formalism: the  $N$ -point moments of the field can be written as derivatives of the generating functional  $Z$

$$\langle \delta(x_1) \dots \delta(x_N) \rangle = \frac{1}{i^N} \frac{\partial^N}{\partial J(x_1) \dots \partial J(x_N)} Z[J] \Big|_{J=0}, \quad (3.4)$$

where

$$Z[J] \equiv \left\langle \exp \left( i \int d^n x J(x) \delta(x) \right) \right\rangle. \quad (3.5)$$

In words, Eq.(3.4) means that the  $N$ -point moments can be considered as the terms of a power series expansion of  $Z$  around  $J = 0$ . The connected  $N$ -point correlation functions are then defined as follows:

$$\xi_N(x_1, \dots, x_N) = \frac{1}{i^N} \frac{\partial^N}{\partial J(x_1) \dots \partial J(x_N)} \ln Z[J] \Big|_{J=0}. \quad (3.6)$$

The connected 2- and 3-point functions coincide with the first moments of the  $\delta$  field:

$$\xi_2(x_1, x_2) \equiv \xi(x_1, x_2) = \langle \delta(x_1) \delta(x_2) \rangle, \quad (3.7)$$

$$\xi_3(x_1, x_2, x_3) = \langle \delta(x_1) \delta(x_2) \delta(x_3) \rangle, \quad (3.8)$$

while for higher  $N$  only the connected part of the moments contribute to the  $N$ -point functions.

In the standard cosmological model density perturbations have originated from the amplification of quantum fluctuations during inflation. Quantum fluctuations are uncorrelated and random, thus the resulting field is the sum of a great number of stochastic variables and, for the central limit theorem, has a Gaussian probability distribution. This prediction of inflationary models has been confirmed by CMB observations. The mean of the field  $\delta(\mathbf{x})$  is 0 by definition, so the probability distribution at a given point  $\mathbf{x}$  is given by:

$$p(\delta(\mathbf{x})) = \frac{1}{\sqrt{2\pi} \sigma^2(\mathbf{x})} \exp \left( -\frac{\delta(\mathbf{x})^2}{2 \sigma^2(\mathbf{x})} \right), \quad (3.9)$$

where  $\sigma^2(\mathbf{x})$  is the variance. The joint probability density function for  $\delta$  on  $N$  points is then a multivariate Gaussian distribution, that can be written as:

$$p(\delta_1, \dots, \delta_N) = \frac{1}{2\pi^{N/2} \det(\mathbf{C})^{1/2}} \exp \left( -\frac{1}{2} \mathbf{d}^T \cdot \mathbf{C}^{-1} \cdot \mathbf{d} \right), \quad (3.10)$$

where  $\mathbf{C} = \langle \delta_1 \dots \delta_N \rangle$  is the covariance and  $\mathbf{d} = (\delta_1, \dots, \delta_N)$  is the vector of the  $N$  values of  $\delta$  at  $(\mathbf{x}_1, \dots, \mathbf{x}_N)$ . For  $N = 2$  the covariance is  $\mathbf{C} = \langle \delta_1 \delta_2 \rangle = \xi(x_1 - x_2)$ . The generating functional for such a field is:

$$Z[J] = \exp \left( -\frac{1}{2} \int d^n x \int d^n y J(x) \xi(x-y) J(y) \right), \quad (3.11)$$

from which we see that  $\ln Z[J]$  is a polynomial of second order in  $J$ . It is then evident from Eq.(3.6) that the  $N$ -point functions for  $N > 2$  vanish, so that the multivariate Gaussian distribution is fully determined by its 1 and 2-point functions.

The translational invariance of the density field allows us to expand  $\delta$  in terms of harmonics. In 3-dimensional space:

$$\tilde{\delta}(\mathbf{k}) = \int d^3 x \delta(\mathbf{x}) e^{-i\mathbf{k}\cdot\mathbf{x}}, \quad (3.12)$$

where  $\tilde{\delta}(\mathbf{k})$  is the Fourier transform of the fluctuation field, which is a complex field, and  $\mathbf{k}$  is a 3-dimensional vector. Since  $\delta$  is real, its Fourier transform satisfies:

$$\tilde{\delta}^*(\mathbf{k}) = \tilde{\delta}(-\mathbf{k}), \quad (3.13)$$

where  $*$  denotes the complex conjugate. In the following we will omit the tilde superscript on Fourier transforms.

The Fourier transform of a Gaussian random field is a complex Gaussian random field, i.e. its real and imaginary parts are jointly Gaussian random fields. If we write  $\delta(\mathbf{k}) = a_{\mathbf{k}} + i b_{\mathbf{k}}$  then:

$$p(\delta(\mathbf{k})) = \frac{1}{\pi \sigma(\mathbf{k})^2} \exp \left( -\frac{a_{\mathbf{k}}^2 + b_{\mathbf{k}}^2}{\sigma(\mathbf{k})^2} \right). \quad (3.14)$$

Complex numbers can also be written as  $\delta(\mathbf{k}) = \delta_{\mathbf{k}} e^{i\theta}$ , where  $\delta_{\mathbf{k}} = \sqrt{a_{\mathbf{k}}^2 + b_{\mathbf{k}}^2}$  is the modulus and  $\theta$  is the phase. If  $\delta(\mathbf{k})$  follows the distribution in Eq.(3.14) then:

$$p(\delta_{\mathbf{k}}, \theta) d\delta_{\mathbf{k}} d\theta = \frac{2\delta_{\mathbf{k}} d\delta_{\mathbf{k}}}{\sigma^2(\mathbf{k})} \left( \frac{d\theta}{2\pi} \right) \exp \left( -\frac{\delta_{\mathbf{k}}^2}{\sigma^2(\mathbf{k})} \right), \quad (3.15)$$

from which we can infer that the modulus follows an exponential distribution while the phase is uniformly distributed in the interval  $(0, 2\pi)$ .

For a statistically homogenous field we can define the power spectrum  $P(\mathbf{k})$  as :

$$\langle \delta(\mathbf{k}) \delta(\mathbf{k}') \rangle = (2\pi)^3 P(\mathbf{k}) \delta_D(\mathbf{k} + \mathbf{k}'), \quad (3.16)$$

where  $\delta_D$  is the Dirac delta function. The power spectrum is the Fourier transform of the 2-point correlation function, in fact:

$$\xi(\mathbf{r}) = \frac{1}{(2\pi)^6} \int d^3k d^3k' \langle \delta(\mathbf{k}) \delta(\mathbf{k}') \rangle e^{-i\mathbf{k}\cdot\mathbf{x} - i\mathbf{k}'\cdot(\mathbf{x}+\mathbf{r})} = \frac{1}{(2\pi)^3} \int d^3k P(\mathbf{k}) e^{i\mathbf{k}\cdot\mathbf{r}}. \quad (3.17)$$

Using the condition in Eq.(3.13) we can write:

$$\langle \delta(\mathbf{k}) \delta^*(\mathbf{k}') \rangle = (2\pi)^3 P(\mathbf{k}) \delta_D(\mathbf{k} - \mathbf{k}'). \quad (3.18)$$

If we take  $\mathbf{k} = \mathbf{k}'$ :

$$\langle |\delta(\mathbf{k})|^2 \rangle = (2\pi)^3 P(\mathbf{k}) \delta_D(0) = P(\mathbf{k}) V_\infty, \quad (3.19)$$

where  $V_\infty$  is the formally infinite volume of integration, which can be considered in practice as the volume of the universe. Notice that  $\langle |\delta(\mathbf{k})|^2 \rangle = \sigma^2(\mathbf{k})$  of Eq.(3.14), so this relation basically states that the power spectrum is proportional to the variance of fluctuations at a given wave-number  $\mathbf{k}$ . This means that if we know the power spectrum we can reconstruct the full probability distribution function of the  $\delta$  field, as already noted above.

Analogously, we can define the bi- and tri-spectrum as:

$$\langle \delta(\mathbf{k}_1) \delta(\mathbf{k}_2) \delta(\mathbf{k}_3) \rangle = (2\pi)^3 \delta_D(\mathbf{k}_{123}) B(\mathbf{k}_1, \mathbf{k}_2, \mathbf{k}_3), \quad (3.20)$$

$$\langle \delta(\mathbf{k}_1) \delta(\mathbf{k}_2) \delta(\mathbf{k}_3) \delta(\mathbf{k}_4) \rangle_c = (2\pi)^3 \delta_D(\mathbf{k}_{1234}) T(\mathbf{k}_1, \mathbf{k}_2, \mathbf{k}_3, \mathbf{k}_4), \quad (3.21)$$

where the subscript  $c$  stands for the connected part.

Enforcing isotropy means that the  $N$ -point functions depend only on the  $N - 1$  distances between the points. For  $N = 2$  the correlation function  $\xi(r)$  depends only on  $r = \|\mathbf{r}\|$  and the power spectrum only depends on  $k = \|\mathbf{k}\|$ . Most of the inflationary models predict that the power spectrum has a power-law form  $P(k) = A_s k^{n_s}$  with  $n_s$  very close to 1, i.e. a scale-free spectrum. These models, though, do not give any information about  $A_s$ , that has to be estimated from observations.

Using the Parseval theorem and the fair sample hypothesis, it is possible to relate the variance of the density field to the power spectrum as:

$$\sigma^2(\mathbf{x}) = \frac{1}{V_\infty} \int d^3x \langle \delta^2(\mathbf{x}) \rangle = \frac{1}{(2\pi)^3} \int d^3k P(k). \quad (3.22)$$

This is what is called the punctual variance, that requires knowledge of the density field in every point of the volume  $V_\infty$  to be computed. To define an observable quantity we can filter the field over a given scale  $R$  to get a mass variance:

$$\sigma_M^2 = \left\langle \frac{\delta M}{M} \right\rangle = \frac{1}{V_\infty} \int d^3x \langle (\delta(\mathbf{x}) * W(\mathbf{x}, R))^2 \rangle = \frac{1}{(2\pi)^3} \int d^3k P(k) \tilde{W}^2(\mathbf{k}, R), \quad (3.23)$$

where  $M$  is the mass contained inside the radius  $R$ :

$$M = \bar{\rho} V(R), \quad (3.24)$$

$$V(R) = \int d^3x W(x, R) \quad (3.25)$$

and  $W$  is a window function. The most used window functions in cosmology are the Gaussian and top-hat filters. Top-hat windows are of easier interpretation because they filter the information contained in the scales smaller than  $R$  sharply, but have complicated Fourier transforms. The Gaussian filter instead remains Gaussian in Fourier space, making calculations much easier.

As we mentioned above the normalisation of the matter power spectrum has to be determined by observations. There are many observables that are sensitive to the normalisation at two different epochs, e.g. CMB, the galaxy power spectrum and the cluster mass function. The amplitude of the spectrum of the CMB gives a constraint on  $A_s$  at the time of decoupling. The mass function is instead proportional to the mass variance filtered with a spherical top-hat in real space on the scale of a cluster, that for historical reasons has been fixed at  $8 \text{ Mpc } h^{-1}$ ,  $\sigma_8^2 \equiv \sigma^2(8 \text{ Mpc } h^{-1})$ . The measurement of  $\sigma_8$  or of the normalisation of the galaxy power spectrum give constraints on the amplitude of the matter power spectrum at low redshift.

## 3.2 Linear Perturbation Theory

The idea behind Linear Perturbation Theory (LPT) is to treat matter density fluctuations as small perturbations around a homogeneous and isotropic distribution, then in the regime  $\delta \ll 1$  the equations that regulate the evolution of the fluid can be linearised and solved. We will outline here the main results, and we refer to Ref.s [43, 124] for further details. The usual

conservation laws for adiabatic fluids are expressed by the Euler equations:

$$\frac{\partial \rho}{\partial t} + \nabla \cdot (\rho \mathbf{v}) = 0, \quad (3.26)$$

$$\frac{\partial \mathbf{v}}{\partial t} + (\mathbf{v} \cdot \nabla) \mathbf{v} + \frac{\nabla P}{\rho} + \nabla \phi = 0, \quad (3.27)$$

$$\frac{\partial s}{\partial t} + \mathbf{v} \cdot \nabla s = 0, \quad (3.28)$$

where  $\phi$  is the Newtonian gravitational potential and is given by the Poisson equation:

$$\nabla^2 \phi = 4\pi G \rho. \quad (3.29)$$

Starting from the homogeneous and static solution  $\rho = \rho_0$ ,  $\mathbf{v} = 0$ ,  $s = s_0$ ,  $P = P_0$  and  $\nabla \phi = 0$ , a perturbation is added and the system is linearised. More specifically, for  $\rho = \rho_0 + \delta\rho$ ,  $\mathbf{v} = \delta\mathbf{v}$ ,  $s = s_0 + \delta s$ ,  $P = P_0 + \delta P$  and  $\phi = \phi_0 + \delta\phi$  we obtain :

$$\frac{\partial \delta\rho}{\partial t} + \rho_0 \nabla \cdot \delta\mathbf{v} = 0, \quad (3.30)$$

$$\frac{\partial \delta\mathbf{v}}{\partial t} + \frac{1}{\rho_0} \left( \frac{\partial P}{\partial \rho} \right)_s \nabla \delta\rho + \frac{1}{\rho_0} \left( \frac{\partial P}{\partial s} \right)_\rho \nabla \delta s + \nabla \delta\phi = 0, \quad (3.31)$$

$$\nabla^2 \delta\phi - 4\pi G \delta\rho = 0, \quad (3.32)$$

$$\frac{\partial \delta s}{\partial t} = 0. \quad (3.33)$$

If we look for solutions in the form of plane waves:

$$\delta\rho(t) = \delta\rho(\mathbf{k}) \exp(i\mathbf{k} \cdot \mathbf{x} + i\omega t) \quad (3.34)$$

$$\delta\mathbf{v}(t) = \delta\mathbf{v}(\mathbf{k}) \exp(i\mathbf{k} \cdot \mathbf{x} + i\omega t) \quad (3.35)$$

$$\delta\phi(t) = \delta\phi(\mathbf{k}) \exp(i\mathbf{k} \cdot \mathbf{x} + i\omega t) \quad (3.36)$$

we find the dispersion relation:

$$\omega^2 = c_s^2 k^2 - 4\pi G \rho_0. \quad (3.37)$$

This equation has two types of solutions depending on whether the wavelength is greater or smaller than the Jeans length:

$$\lambda_J \equiv c_s \left( \frac{\pi}{G\rho_0} \right)^{1/2}. \quad (3.38)$$

If  $\lambda < \lambda_J$  then the frequency  $\omega$  is real and the perturbation is an acoustic wave that propagates with fixed amplitude, while if  $\lambda > \lambda_J$   $\omega$  is imaginary

and the amplitude of the perturbation  $\delta\rho = \delta\rho(\mathbf{k}) \exp(\pm|\omega|t) \exp(i\mathbf{k}\cdot\mathbf{r})$  varies with time exponentially. One of the two modes decays over time, while the other grows exponentially.

We can get an idea of how an over-density in an expanding universe can grow by considering a spherical perturbation as a small closed universe inside a flat background universe. The mean density inside the perturbation  $\rho_1$  is larger than the background mean density  $\rho_0$ . If we consider scales that are much larger than the Jeans length we can neglect pressure terms and the first Friedmann equation for the two reads:

$$H_0^2 = \frac{8}{3}\pi G \rho_0 \quad (3.39)$$

$$H_1^2 = \frac{8}{3}\pi G \rho_1 - \frac{c^2}{a^2}. \quad (3.40)$$

By defining  $\delta = (\rho_1 - \rho_0)/\rho_0$ , when  $H_0 = H_1$ :

$$\delta = \frac{3c^2}{8\pi G \rho_0 a^2}. \quad (3.41)$$

For a flat universe  $\rho_0 \propto a^{-3(1+w)}$ , so the evolution of  $\delta$  is given by:

$$\delta \propto a^{1+3w}. \quad (3.42)$$

This means that in the radiation era the evolution of perturbations is:

$$\delta(t) \simeq \delta_r(t) \propto a(t)^2, \quad (3.43)$$

while after equivalence:

$$\delta(t) \simeq \delta_m(t) \propto a(t). \quad (3.44)$$

For a more insightful treatment, if we restrict to scales much smaller than the horizon, we can write Eq.s (3.26)-(3.29) in the Post-Newtonian approximation [107]:

$$\left. \frac{\partial\rho}{\partial t} \right|_{\mathbf{r}} + \nabla_{\mathbf{r}} \cdot (\rho\mathbf{u}) + \frac{P}{c^2} \nabla_{\mathbf{r}} \cdot \mathbf{u} = 0, \quad (3.45)$$

$$\left. \frac{\partial\mathbf{u}}{\partial t} \right|_{\mathbf{r}} + (\mathbf{u} \cdot \nabla_{\mathbf{r}})\mathbf{u} + \left( \rho + \frac{P}{c^2} \right)^{-1} \nabla_{\mathbf{r}} P + \nabla_{\mathbf{r}} \phi = 0, \quad (3.46)$$

$$\nabla_{\mathbf{r}}^2 \phi - 4\pi G \rho = 0, \quad (3.47)$$

where  $\mathbf{r} = a\mathbf{x}$  is the proper coordinate,  $\mathbf{x}$  is the comoving coordinate,  $\mathbf{u} = H\mathbf{r} + \mathbf{v}$  is the proper velocity and  $\mathbf{v}$  is the peculiar velocity, i.e. the velocity

of the fluid element once we subtract the Hubble flow. For non-relativistic fluids the terms  $P/c^2$  can be considered negligible. We consider an expanding homogeneous and isotropic solution with small perturbations in the form:

$$\rho = \rho_0(1 + \delta), \quad (3.48)$$

$$\mathbf{u} = H\mathbf{r} + \mathbf{v}, \quad (3.49)$$

$$P = P_0 + \delta P, \quad (3.50)$$

$$\phi = \phi_0 + \delta\phi. \quad (3.51)$$

The corresponding linearised system of equations, neglecting relativistic pressure terms, is:

$$\frac{\partial \delta\rho}{\partial t} + H(\mathbf{r} \cdot \nabla_{\mathbf{r}} \delta\rho + 3\delta\rho) + \rho_0 \nabla_{\mathbf{r}} \cdot \mathbf{v} = 0, \quad (3.52)$$

$$\frac{\partial \mathbf{v}}{\partial t} + H\mathbf{v} + (H\mathbf{r} \cdot \nabla_{\mathbf{r}})\mathbf{v} + \frac{1}{\rho_0} \nabla_{\mathbf{r}} \delta P + \nabla_{\mathbf{r}} \delta\phi = 0, \quad (3.53)$$

$$\nabla_{\mathbf{r}}^2 \delta\phi - 4\pi G \delta\rho = 0. \quad (3.54)$$

By changing from proper to comoving coordinates we get:

$$\frac{\partial \delta\rho}{\partial t} + 3H\delta\rho + \frac{\rho_0}{a} \nabla_{\mathbf{x}} \cdot \mathbf{v} = 0, \quad (3.55)$$

$$\frac{\partial \mathbf{v}}{\partial t} + H\mathbf{v} + \frac{1}{a\rho_0} \nabla_{\mathbf{x}} \delta P + \frac{1}{a} \nabla_{\mathbf{x}} \delta\phi = 0, \quad (3.56)$$

$$\frac{1}{a^2} \nabla_{\mathbf{x}}^2 \delta\phi - 4\pi G \delta\rho = 0. \quad (3.57)$$

Looking for solutions in the form of plane waves (Eq.s (3.34)-(3.36)) and defining  $\delta_k(t) = \delta\rho(\mathbf{k}) \exp(i\omega t)$ , we find the dispersion relations:

$$\ddot{\delta}_k + 2\frac{\dot{a}}{a}\dot{\delta}_k + \delta_k \left( k^2 c_s^2 - \frac{32}{3} \pi G \rho_0 \right) = 0 \quad \text{for } a < a_{eq}, \quad (3.58)$$

$$\ddot{\delta}_k + 2\frac{\dot{a}}{a}\dot{\delta}_k + \delta_k (k^2 c_s^2 - 4\pi G \rho_0) = 0 \quad \text{for } a > a_{eq}, \quad (3.59)$$

where the relation for the radiation era is obtained by considering also the pressure terms. Assuming solutions of power-law type  $\delta_k = \alpha t^\beta$  we find the Jeans length to be:

$$\lambda_{J,r} = c_s \sqrt{\frac{3\pi}{8G\rho_0}} \quad \text{for } a < a_{eq}, \quad (3.60)$$

$$\lambda_{J,m} = \frac{c_s}{5} \sqrt{\frac{24\pi}{G\rho_0}} \quad \text{for } a > a_{eq}. \quad (3.61)$$

Comparing the Jeans length with the size of the horizon Eq.(2.65) one can note that during the radiation era  $\lambda_{J,r} > R_H$ . In fact:

$$\lambda_{J,r} = \frac{2\pi c t}{\sqrt{3}} > 2ct, \quad (3.62)$$

this means that fluctuations in the density field on scales smaller than the horizon do not grow until the time of matter-radiation equivalence.

This analysis can also be applied to the DM component, that is a collisionless fluid, by substituting  $c_s$  with the velocity dispersion  $\sigma_v$ . In this case what opposes the collapsing tendency due to self-gravity is the stochastic diffusion of the particles, that tends to smear out and eventually damp the fluctuations.

The relations obtained above are only valid for the dominant component of each era. It is possible to gain some insight in the growth of perturbations of sub-dominant components by considering a multi-component fluid [77]. The dispersion relation for the dark matter component in the radiation era is then given by:

$$\ddot{\delta}_{k,DM} + 2\frac{\dot{a}}{a}\dot{\delta}_{k,DM} + k^2\sigma_v^2\delta_{k,DM} - 4\pi G\sum_i\rho_{0,i}\delta_{k,i} = 0, \quad (3.63)$$

where the sum in the last term runs on all the components. As we have seen radiation perturbations do not grow in this era and since the baryonic component is still coupled to radiation its perturbations do not grow either. Eq.(3.63) then reduces to:

$$\ddot{\delta}_{k,DM} + 2\frac{\dot{a}}{a}\dot{\delta}_{k,DM} + k^2\sigma_v^2\delta_{k,DM} - 4\pi G\rho_{0,DM}\delta_{k,DM} = 0. \quad (3.64)$$

If we restrict to scales well above the Jeans length we can neglect the third term and solve for the growing mode of  $\delta_{k,DM}$ :

$$D_{+,DM} = 1 + \frac{3a}{2a_{eq}}. \quad (3.65)$$

From this we can see that DM perturbations that enter the horizon at a time  $t_{hor}$  before equivalence grow by a factor of:

$$\frac{D_+(t_{eq})}{D_+(t_{hor})} = \frac{5/2}{1 + 3a_{hor}/(2a_{eq})} \quad (3.66)$$

which is smaller than 2.5. This stagnation of DM perturbations is called Meszaros effect [114]. After equivalence DM becomes the dominant component and DM fluctuations begin to grow as in Eq.(3.44).

Similarly, we can write the dispersion relation for baryonic matter after decoupling as:

$$\ddot{\delta}_{k,b} + 2\frac{\dot{a}}{a}\dot{\delta}_{k,b} + k^2 c_s^2 \delta_{k,b} - 4\pi G \rho_{0,DM} \delta_{k,DM} = 0, \quad (3.67)$$

and solve for the growing mode:

$$D_{+,b} = D_{+,DM} (1 - a_{dec}/a). \quad (3.68)$$

This is smaller than  $D_{+,DM}$  but tends to it with growing  $a$ . This means that as soon as baryonic matter decouples from radiation its fluctuations have an accelerated growth with respect to DM ones. This phenomenon is called baryon catch up. As it is often phrased, DM perturbations collapse first, forming potential wells in which baryonic matter subsequently falls.

The Jeans length has a corresponding mass scale, called the Jeans mass, that discriminates whether a fluctuation of a given mass will collapse or not. The Jeans mass is defined as:

$$M_J = \frac{4\pi}{3} \rho_M \lambda_J^3 \quad (3.69)$$

for baryonic matter and

$$M_J = \frac{4\pi}{3} m_{DM} n_{DM} \lambda_J^3 \quad (3.70)$$

for DM, where  $m_{DM}$  is the mass of DM particles and  $n_{DM}$  is their number density. In a collisionless fluid, fluctuations on scales  $< M_J$  can be damped by two physical processes: in the ultra-relativistic regime, when the particle velocities are all of order  $v \simeq c$ , the amplitude of a perturbation decays because particles move with a large dispersion from over-dense to under-dense regions, and vice versa; in the non-relativistic regime there is on the other hand a considerable spread in the particle velocities which tends to smear out the perturbation. In both cases, after a time  $t$ , perturbations are dissipated on a scale  $\lambda < \lambda_{fs}$ , where  $\lambda_{fs}$  is the free-streaming scale:

$$\lambda_{fs} = a(t) \int_0^t \frac{v(t')}{a(t')} dt'. \quad (3.71)$$

Analogously to the Jeans case, a free-streaming mass can be defined:

$$M_{fs} = \frac{4\pi}{3} m_{DM} n_{DM} \lambda_{fs}^3. \quad (3.72)$$

It is found that both for CDM and HDM  $M_{fs}$  equals  $M_J$  soon after equivalence, so the phenomenon of free-streaming erodes all the fluctuations with masses below the Jeans mass.

In the baryonic component viscosity and thermal diffusion due to the interaction with photons before equivalence dissipate all perturbations below the scale:

$$\lambda_S \simeq 2,3 c (\tau_{\gamma e} t)^{\frac{1}{2}}, \quad (3.73)$$

where  $\tau_{\gamma e}$  is the rate of interactions between photons and electrons. The related Silk mass is:

$$M_S \simeq 8 \times 10^7 (\Omega_b h^2)^{-5} \left( \frac{1+z}{1+z_{eq}} \right)^{-\frac{15}{4}} M_{\odot} \quad (3.74)$$

This dissipative process causes a decrease of the amplitude of an acoustic wave on a mass scale  $M < M_J$ , with a rate that depends on  $M$ .

Since at the time of decoupling the value of the free-streaming mass is equal to the value of the Jeans mass, the type of DM particles determines the scenario of structure formation:

**Bottom-up** the least massive structures collapse first, then the bigger ones form by merging;

**Top-down** the most massive structures collapse first, then the smaller ones form by fragmentation of the bigger ones.

If the DM is cold, a bottom-up scenario is preferred, since the first collapsed objects have a mass  $M_J(z_{dec}) \sim 10^5 - 10^6 M_{\odot}$ ; vice versa, if the DM is hot, structure formation would happen with a top-down hierarchy, starting from objects with mass  $M_{J,max} \simeq 3.5 \cdot 10^{15} (\Omega_{HDM} h^2)^{-2} M_{\odot}$ .

### 3.2.1 Power spectrum evolution in linear regime

In the linear regime each Fourier mode evolves independently so the evolution of the shape of the power spectrum is described by a simple function of the scale  $T(k)$ , called transfer function. The processed power spectrum  $P(k, t)$  is related to the primordial power spectrum  $P_{ini}(k) = P(k, t_{ini})$  as:

$$P(k, t) = P_{ini}(k) D_+^2(k, t). \quad (3.75)$$

For scales larger than the Jeans length the growing factor  $D_+$  does not depend on  $k$  so:

$$P(k, t) = P_{ini}(k)D_+^2(t). \quad (3.76)$$

As seen above, the growing factor has a different trend before and after equivalence:

$$D_+ \propto \begin{cases} a^2 & a < a_{eq}, \\ a & a > a_{eq}. \end{cases} \quad (3.77)$$

Matter fluctuations that enter the horizon before equivalence suffer from Meszaros effect until equivalence, while fluctuations on scales large enough to remain outside the horizon until equivalence continue to grow as  $a^2$ . This different behaviour distorts the initial power spectrum in a predictable way. Indicating the moment when a given fluctuation enters the horizon with  $a_H$ , the amplitude at equivalence is given by:

$$\delta(k, a_{eq}) = \begin{cases} \delta(k, a_{ini}) \left(\frac{a_H}{a_{ini}}\right)^2 \propto \delta(k, a_{ini})k^{-2} & \text{for } a_H < a_{eq}, \\ \delta(k, a_{ini}) \left(\frac{a_{eq}}{a_{ini}}\right)^2 \propto \delta(k, a_{ini}) & \text{for } a_H > a_{eq}, \end{cases} \quad (3.78)$$

where  $a_{ini}$  is the expansion factor calculated at  $t_{ini}$ . Thus, the power spectrum at equivalence is given by:

$$P(k, a_{eq}) \propto \delta^2(k, a_{eq}) = \begin{cases} \delta^2(k, a_{ini})k^{-4} \propto k^{n_s-4} & \text{for } a_H < a_{eq}, \\ \delta^2(k, a_{ini}) \propto k^{n_s} & \text{for } a_H > a_{eq}. \end{cases} \quad (3.79)$$

The matter transfer function at equivalence is shown in Figure 3.1 for different species of DM. The point in which the slope changes indicates the value of  $k$  corresponding to the scale of the horizon at equivalence. The main difference between the predicted power spectrum for hot and CDM is that in the former case free-streaming erodes all the fluctuations on small scales.

### 3.3 Non-linear regime

When the fluctuation field becomes  $|\delta| \sim 1$  the linear approximation is no longer valid and higher-order terms of the expansion become important. At second order some of the additional terms induce the coupling of modes on different scales, thus Fourier modes do not evolve independently anymore [124].

The Jeans length as given by Eq.s (3.60) and (3.61) grows in time, hence increasingly larger scales begin to collapse. Modes that collapse spawn higher

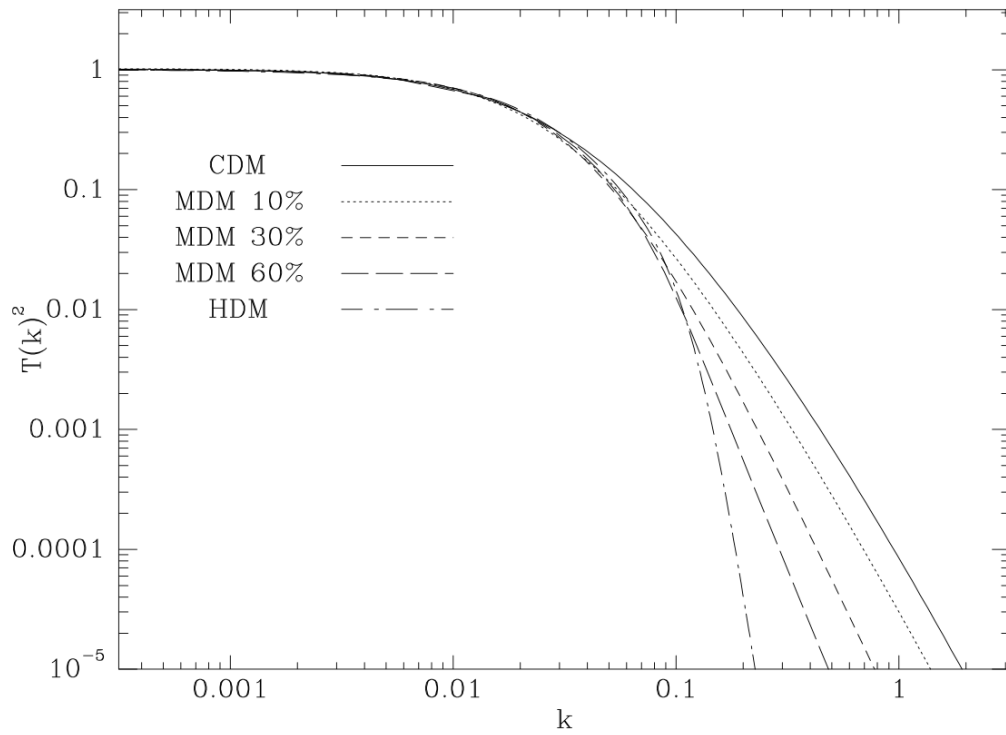


**Figure 3.1:** Square of the matter transfer function for the HDM, mixed DM (the indicated percentage refers to the HDM fraction) and CDM cases. From Ref. [44].

frequency perturbations (harmonics) in phase with the original. These harmonics then interact with other modes leading to the coordination of phases between modes of different amplitudes [149]. This breaks the uniform distribution of  $\theta$ , meaning that the  $\delta(\mathbf{x})$  field is no longer Gaussian. In Fourier space modes on large scales can still be considered as Gaussian distributed, while at small scales the departure from Gaussianity is not negligible and grows in time.

As we mentioned in §3.2, Gaussian fields can be fully specified by their power spectrum. When non-gaussianities become important, the power spectrum is not sufficient and higher-order correlation functions are sourced. We will get back on this in Chapter 5. Notice however that these higher-order statistics focus on the information content of the modulus of the fluctuation field and are strongly correlated with the power spectrum, yielding few independent information. Various statistics of the phases have been proposed, which aim at the information content of the phases of the field. See e.g. [37, 121] and references therein.

The power spectrum is itself distorted by the non-linear evolution of the mode amplitudes, so its evolution cannot be described by a simple transfer function. In particular, the modes generated by the collapse enhance the power spectrum at high  $k$ , as it is shown in Figure 3.2.

In this regime the evolution of the fluctuation field cannot be solved analytically, unless simplifying approximations are introduced. Perturbation Theory (PT) is the natural extension of LPT to higher orders in the expansion of the  $\delta$  field around a homogeneous and isotropic background solution. There exists various versions of PT, the exposition of which is beyond the scope of this thesis. We refer to [22, 35] for a review of the topic.

In the following we will describe two approximate solutions, the Zel'dovich approximation and the Spherical Collapse model.

### 3.3.1 The Zel'dovich approximation

In analogy with fluid dynamics, it is possible to define a Lagrangian reference frame for cosmic fluids where the coordinates are constant along the fluid flow. These are related to the Eulerian coordinates through a transformation that is in general non-linear. The Zel'dovich approximation [189] is essentially a prescription on this transformation where the Eulerian position of a fluid

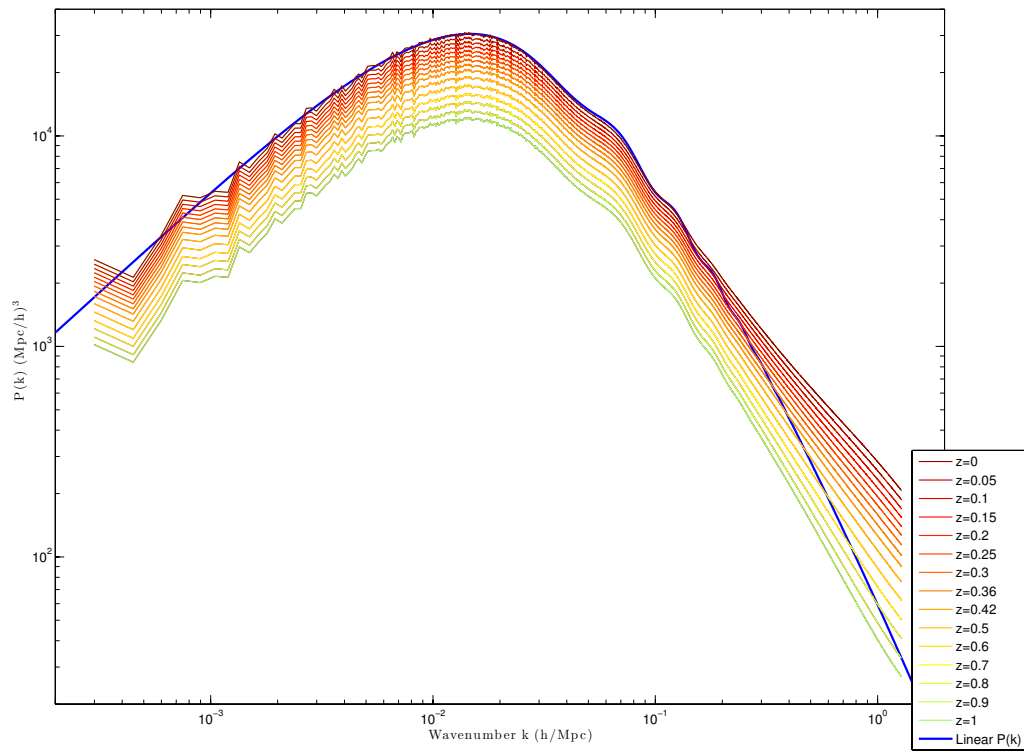


**Figure 3.2:** Matter power spectrum evolution in the non-linear regime from the DEUS FUR simulation [134]. The solid blue curve shows the linear prediction for the matter power spectrum at  $z = 0$ .

element is a function of the initial Lagrangian position and time only:

$$r(q, t) = a(t) q + F(q, t), \quad (3.80)$$

where  $q$  is the initial Lagrangian position and  $F(q, t)$  is the displacement field. In the Zel'dovich approximation  $F$  is a separable function:

$$F(q, t) = f(t) G(q). \quad (3.81)$$

Calibrating  $f$  and  $G$  on the linear solution, we get to:

$$r(q, t) = a(t) [q - D_+(t) \nabla_q \Phi_0(q)], \quad (3.82)$$

where  $\Phi_0$  is called the peculiar velocity potential. Its name comes from the consideration that:

$$v = \frac{dr}{dt} - H r = -a(t) \dot{D}_+(t) \nabla_q \Phi_0(q). \quad (3.83)$$

Using the conservation of mass it is possible to relate the density in the Lagrangian and Eulerian coordinate system. In fact:

$$dM = \rho_0 d^3q = \rho(x, t) d^3x, \quad (3.84)$$

where  $x = r/a$  is the comoving Eulerian coordinate. From this we infer that:

$$\rho(x, t) = \rho_0 \frac{d^3q}{d^3x}. \quad (3.85)$$

The quantity  $d^3x/d^3q$  is the determinant of the Jacobian of the transformation Eq.(3.82):

$$J \left[ \frac{\partial x}{\partial q} \right] = a^3 \left[ \delta_{ij} - D_+ \frac{\partial^2 \Phi_0}{\partial q_i \partial q_j} \right], \quad (3.86)$$

where

$$\frac{\partial^2 \Phi_0}{\partial q_i \partial q_j} \quad (3.87)$$

is the deformation tensor. Since it is a symmetric tensor it is always possible to diagonalise it and the Eulerian density results to be:

$$\rho(x, t) = \frac{\rho_0}{a^3} \prod_{i=1}^3 [1 - D_+ \lambda_i(q)]^{-1}, \quad (3.88)$$

where  $\lambda_i$  are the eigenvalues of the deformation tensor. Writing the density in this form makes evident that the evolution is determined by the sign of

the eigenvalues. In particular, when at least one of the eigenvalues is positive one obtains  $\rho(x, t) \rightarrow \infty$  for  $D_+ \lambda_i \rightarrow 1$ .

We can interpret the Zel'dovich solution as an approximation of the dynamics of a collapsing (or expanding) region due to local gravitational effects, with the deformation tensor playing the role of the tidal tensor. In fully non-linear dynamics this evolves in time, while here it is completely determined by the initial configuration of the fluid elements. The eigenvalues of the deformation tensor, once ordered  $\lambda_1 \leq \lambda_2 \leq \lambda_3$ , can be used to identify the regions of Lagrangian space that will give rise to different types of structures:

- Void:  $\lambda_1 \leq \lambda_2 \leq \lambda_3 < 0$ , the fluid element expands along all the eigenvectors of the deformation tensor,
- Sheet:  $\lambda_1 \leq \lambda_2 < 0 \leq \lambda_3$  the fluid element expands along two and collapses along one of the eigenvectors of the deformation tensor,
- Filament:  $\lambda_1 < 0 \leq \lambda_2 \leq \lambda_3$  the fluid element expands along one and collapses along two of the eigenvectors of the deformation tensor,
- Halo:  $0 < \lambda_1 \leq \lambda_2 \leq \lambda_3$  the fluid element collapses along all the eigenvectors of the deformation tensor.

In practice when the collapse starts in one of the directions the denominator of Eq.(3.88) may vanish and the density predicted with this approximation is divergent. This can be understood by considering the trajectories of the fluid elements described by the displacement field: the elements follow the trajectories imprinted by the gravitational field at the initial moment but they cannot interact, so they cross each other trajectories and the mapping between Lagrangian and Eulerian spaces becomes singular, leading to the formation of caustics, where the density is infinite. The moment of the formation of the first caustic is called shell crossing and is considered as the limit at which the Zel'dovich approximation breaks down.

### 3.3.2 Spherical collapse

The Spherical Collapse is an exact solution to a highly idealised case: the collapse of a perfectly spherical matter over-density in an expanding background with vanishing initial relative velocity. We can consider the over-density as a closed matter universe and use the Friedmann equations to compute its evolution. This solution can be used to compare deviations from linearity at the time of collapse by comparison with predictions from linear theory.

For simplicity let us consider a spherical perturbation during the matter dominated era, which is in any case the period in which most of the perturbations begin to grow. Since in this era  $a \propto t^{2/3}$  we can write the time dependence of  $\delta$  as:

$$\delta(t) = D_+(t_i) \left(\frac{t}{t_i}\right)^{2/3} + D_-(t_i) \left(\frac{t}{t_i}\right)^{-1}, \quad (3.89)$$

where we have included the decaying mode, that in this era scales as  $a^{-3/2}$ . Let us also assume that  $\delta(t_i) < 1$ , so that we can use the linearised continuity equations to compute the velocity:

$$v = i \frac{\dot{\delta}_k}{k} = \frac{i}{k_i t_i} \left[ \frac{2}{3} D_+ \left(\frac{t}{t_i}\right)^{\frac{1}{3}} - D_- \left(\frac{t}{t_i}\right)^{-\frac{4}{3}} \right], \quad (3.90)$$

where  $k = k_i/a$  is the comoving wavenumber. We have assumed that  $v(t_i) = 0$  so  $D_-(t_i) = \frac{2}{3} D_+(t_i)$  and we get:

$$\delta_i = D_+(t_i) + D_-(t_i) = \frac{5}{3} D_+(t_i). \quad (3.91)$$

This means that the three fifths of the initial over-density remain in the growing mode while the rest decays.

To see how the perturbation collapse let us write the Friedmann equation:

$$\left(\frac{\dot{R}}{R_i}\right)^2 = H_i^2 \left[ \Omega_P(t_i) \frac{R_i}{R} + 1 - \Omega_P(t_i) \right], \quad (3.92)$$

where  $R$  is the scale factor of the perturbation, that can be interpreted as its radius, and  $\Omega_P(t_i) = (1 + \delta_i)\Omega(t_i)$  is the perturbation density parameter. If we look for the maximum of  $R$ , i.e.  $\dot{R}_M = 0$ , we find:

$$\frac{R_M}{R_i} = \frac{\Omega_P(t_i)}{\Omega_P(t_i) - 1}. \quad (3.93)$$

Since  $\rho \propto R^3$  we have:

$$\rho(R_M) = \rho_c(t_i) \Omega_P(t_i) \left( \frac{\Omega_P(t_i) - 1}{\Omega_P(t_i)} \right)^3. \quad (3.94)$$

There exists an exact parametric solution to the Friedmann equations for a closed matter universe which reads:

$$R(\theta) = R_i \frac{\Omega_P(t_i)}{2(\Omega_P(t_i) - 1)} (1 - \cos \theta), \quad (3.95)$$

$$t(\theta) = \frac{1}{2 H_i} \frac{\Omega_P(t_i)}{(\Omega_P(t_i) - 1)^{3/2}} (\theta - \sin \theta). \quad (3.96)$$

The maximum of  $R$  corresponds to  $\theta_M = \pi$ , so we find:

$$t_M = \frac{\pi}{2 H_i} \frac{\Omega_P(t_i)}{(\Omega_P(t_i) - 1)^{3/2}} = \left[ \frac{3\pi}{32 G \rho_P(t_M)} \right]^{\frac{1}{2}}, \quad (3.97)$$

where we have used Eq.(3.94). The background density at the maximum is:

$$\rho(t_M) = \frac{1}{6\pi G t_M^2}, \quad (3.98)$$

so that  $D_+(t_M) \simeq 4, 6$ . The prediction for the growing factor in the linear theory is:

$$D_+(t_M) = D_+(t_i) \left( \frac{t_M}{t_i} \right)^{\frac{2}{3}} \simeq 1.07, \quad (3.99)$$

showing that the linear prediction is already a factor of four smaller than the non-linear solution at the time of maximum expansion.

When the perturbation reaches its maximum size it begins to collapse. The solution Eq.(3.95) indicates that the perturbation should collapse to a point of infinite density at a time  $t_c = 2 t_M$ . In reality when the density is high shock waves are formed and the heating due to dissipation of such shocks drives the perturbation to the virial equilibrium thus halting the collapse. The virial theorem states that:

$$2T + V = 0 \quad (3.100)$$

where  $T$  is the kinetic energy and  $V$  is the potential energy. This means that the total energy is:

$$E = -T = \frac{V}{2}. \quad (3.101)$$

At the time of virialisation  $t_{vir}$  we have:

$$E(t_{vir}) = \frac{1}{2} \left( -\frac{3 G M^2}{5 R_{vir}} \right), \quad (3.102)$$

while at  $t_M$  the kinetic energy is 0 so:

$$E(t_M) = -\frac{3 G M^2}{5 R_M} \quad (3.103)$$

and  $\rho_P(t_{vir}) = 8\rho_P(t_M) \simeq \rho_P(t_c)$ . This means that  $\delta(t_c) \sim 200$  while the linear theory prediction is  $D_+(t_c) \simeq 1.686$ , two orders of magnitude away from the non-linear solution.

# Chapter 4

## Numerical simulations

In the previous Chapter we have seen that an analytical treatment of the collapse of matter in the non-linear regime is only possible in approximate cases which are not applicable to follow the clustering of the density field in the full non-linear regime. This requires cosmological simulations which allow to follow the evolution of the density and velocity fields over a large range of scales and times. These consist of a discretised representation of large volumes of the universe evolved from a set of initial conditions at high redshift in a given cosmological setup. The evolution of ordinary matter under the action of gravity can be solved with hydrodynamical methods, on the other hand the DM fluid is collisionless to good approximation on astrophysical scales and thus requires different numerical techniques. Most of the existing cosmological codes make use of N-body techniques, which will be presented in §4.1. The computational domain of such simulations is usually a cube of side  $L$ , which for modern simulations varies from hundreds of  $\text{Mpc } h^{-1}$  to tens of  $\text{Gpc } h^{-1}$ . As we will see fields can be discretised on this computational domain either as particles or on a grid. In both cases the number of computational elements is bounded by memory and time requirements, limiting the range of scales that can be explored with simulations and introducing systematic errors.

In §4.2-4.4 we will briefly describe numerical methods employed for the simulations used in this thesis. We outline Eulerian hydrodynamics methods in §4.2, as an introduction to numerical methods for clustering Dark Fluids simulations, discussed in Chapter 8. In §4.3 we present the basic method to generate initial conditions for N-body simulations, while in §4.4 we discuss the estimation of the matter power spectrum from simulations, including an overview of numerical systematic errors related to this estimation.

## 4.1 N-body techniques

A collisionless self-gravitating gas of particles of mass  $m$  is described in phase space by its distribution function  $f(t, \mathbf{x}, \mathbf{p})$ , where  $\mathbf{p}$  is the momentum, and its evolution is given by the collisionless Boltzmann's equation [24]:

$$\frac{df(t, \mathbf{x}, \mathbf{p})}{dt} = \frac{\partial f}{\partial t} + \frac{\mathbf{p}}{m a^2} \cdot \nabla_{\mathbf{x}} f - m \nabla_{\mathbf{x}} \phi \cdot \nabla_{\mathbf{p}} f = 0, \quad (4.1)$$

with the gravitational potential  $\phi$  obeying the Poisson equation:

$$\nabla^2 \phi = \frac{4\pi G m_{DM}}{a} \left( \int d^3 p f - \bar{n} \right), \quad (4.2)$$

where  $\bar{n}$  is the mean number of DM particles in the universe. These equations forms the so called Vlasov-Poisson system. In the case of CDM the thermal velocity dispersion is much smaller than the bulk velocity due to gravitational interactions, so its velocity distribution has negligible width. This confines the evolution of  $f$  in a sheet in phase space and reduces the dimensionality of the problem, allowing to solve the Vlasov-Poisson system in 3D configuration space. In linear regime the sheet does not fold, so in each point  $\mathbf{x}$  the velocity is single-valued and DM can be treated as a perfect fluid with  $P \approx 0$  [189]. As soon as shell crossing occurs multiple streams with different velocities pass through the points where caustics form and the fluid can no longer be described by bulk quantities.

The solution of Eq.(4.1) can be represented by an infinite set of characteristics. N-body techniques rely on a coarse-graining of the distribution function, which corresponds to sampling the characteristics with a finite number  $N$  of tracers. The distribution function of these tracers is [94, 59]:

$$f_N(t, \mathbf{x}, \mathbf{p}) = \sum_{i=1}^N \delta_D(\mathbf{x} - \mathbf{x}_i(t)) \delta_D(\mathbf{p} - \mathbf{p}_i(t)). \quad (4.3)$$

Substituting Eq.(4.3) in (4.1) we can see that  $f_N$  is conserved along the characteristics:

$$\frac{d\mathbf{x}_p}{dt} = \mathbf{v}_p, \quad (4.4)$$

$$\frac{d\mathbf{v}_p}{dt} = -\nabla \phi, \quad (4.5)$$

where  $\mathbf{x}_p$  and  $\mathbf{v}_p$  are the position and velocity of the tracers. These tracers can be viewed as particles representing a discrete volume  $\delta V$  containing a

mass  $m$  of microscopic DM particles. In N-body techniques at each time-step particles are displaced following the equations of motion Eq.s (4.4)-(4.5) and the force field  $\nabla\phi$  generated by the new configuration of particles is computed using Poisson solver algorithms. N-body methods differ mainly in this second step.

The simplest approach to compute the gravitational force acting on particles is called direct summation or Particle-Particle (PP)[2]: the sum

$$\mathbf{f}(\mathbf{x}_j) = m_j \sum_{i \neq j} G m_i \frac{\mathbf{x}_i - \mathbf{x}_j}{|\mathbf{x}_i - \mathbf{x}_j|^3} \quad (4.6)$$

is performed for each particle  $j$  summing over all the other  $N - 1$  particles  $i$ . This method has a computational cost of the order of  $N^2$ , making it unaffordable for cosmological simulations, where the number of particles ranges from  $10^6$  to  $10^{12}$ . Moreover, this method diverges when close encounters occur between two particles, so a “smoothing” of the force is required [1]. This is done by substituting the Newtonian force with a force  $\mathbf{f}_{ij}^{soft}$  that tends to  $\mathbf{f}_{ij}^{newt}$  when  $|\mathbf{x}_i - \mathbf{x}_j| \rightarrow \infty$  and tends to 0 when  $|\mathbf{x}_i - \mathbf{x}_j| \rightarrow 0$ . A simple example of such a smoothed force is:

$$\mathbf{f}_{ij}^{soft} = G m_i m_j \frac{\mathbf{x}_i - \mathbf{x}_j}{(|\mathbf{x}_i - \mathbf{x}_j|^2 - \epsilon^2)^{3/2}}, \quad (4.7)$$

where  $\epsilon$  is called softening length and can be interpreted as the size of the particles. Unphysical two-body interactions can arise if the softening length is smaller than the mean inter-particle separation [112], leading to departures from the collisionless nature of the Vlasov-Poisson system.

The so called Hierarchical Tree methods [16] alleviate the computational cost of the Poisson solver by using direct summation only for particles that are below a certain distance, while the force due to long range interactions is approximated by expanding the gravitational field in multipoles and truncating the expansion to a given order. The computational cost of these algorithms is of the order of  $N \log N$ . In these methods, particles are assigned to a tree of computational cells, which is constructed by iterative subdivision of the volume of each cell in 8 parts, halting the procedure when the number of particles in the cell goes below a threshold. An opening angle parameter for the tree is defined so that smaller distances correspond to larger opening angles. This procedure assures high resolution of the force in high density regions but is inefficient for low contrast mass distribution.

Particle-mesh (PM) methods [83] take a different approach to solve the Poisson equation. In these methods a grid is superimposed to the particle distribution and physical quantities like density and velocity are interpolated from particle positions to grid nodes. Imposing periodic boundary conditions allows one to use Fast Fourier Transform algorithms [132] to compute the potential. In fact, in Fourier space the Poisson equation is:

$$\phi(\mathbf{k}) = G(\mathbf{k}) \rho(\mathbf{k}), \quad (4.8)$$

where  $G(\mathbf{k})$  is the Green function, whose form depends on the discretisation scheme. PM algorithms first transform  $\rho(\mathbf{x}) \rightarrow \rho(\mathbf{k})$  using forward FFT, multiply it by the Green function to obtain  $\phi(\mathbf{k})$  and then transform  $\phi(\mathbf{k}) \rightarrow \phi(\mathbf{x})$  using backwards FFT. The potential is then interpolated back to the particle positions. The advantage of this approach is that grid methods have a “natural” softening length given by the spacing of the grid points, which also sets the resolution scale of the simulation. This also means that the numerical error on the force with this method is more predictable than with PP or Tree methods. In the limit of vanishing spacing ( $N_g \rightarrow \infty$ ) we recover the Vlasov-Poisson system. The computational cost of PM methods is of order  $N$  for particle displacements and  $N_g \log N_g$  for the Poisson solver, where  $N_g$  is the number of grid nodes.

Tree and PM methods are the basis upon which currently used algorithms have been built. TreePM hybrid methods use the Tree algorithm for small-range interactions and exploit the speed of FFT to compute long-range gravitational forces with the PM algorithm. Adaptive Mesh Refinement (AMR) methods allow to reach higher accuracy in high density regions with respect to PM methods by introducing sub-grids with finer spacing where the density in the grid cells exceeds a given threshold. The potential at refined levels of the grid is computed with relaxation methods, using the solution interpolated from the previous level as initial guess and as boundary conditions, while at coarse level the potential is computed using standard FFT methods [96, 170]. The RAMSES code [170], used in this thesis, is an AMR code.

## 4.2 Eulerian hydrodynamics

For collisional fluids, like baryonic matter, the Boltzmann equation can be expanded in its moment series and truncated with the introduction of an equation of state. The moments are found by integrating the Boltzmann

equation as:

$$\int Q(\mathbf{p}) \left( \frac{\partial f}{\partial t} + \frac{\mathbf{p}}{m a^2} \cdot \nabla_{\mathbf{x}} f - m \nabla_{\mathbf{x}} \phi \cdot \nabla_{\mathbf{p}} f \right) d^3 p = 0, \quad (4.9)$$

where  $Q(\mathbf{p})$  is a conserved quantity. In particular, three moments with  $Q(\mathbf{p}) = (m, \mathbf{p}, \mathbf{p}^2/2m)$  are sufficient to fully characterise the system if the equation of state is in the form  $P = P(\rho, e)$ , where  $e$  is the specific total energy of the fluid. The resulting equation system in proper coordinates and in the so called conservative form reads as:

$$\frac{\partial \rho}{\partial t} + \nabla \cdot (\rho \mathbf{u}) = 0, \quad (4.10)$$

$$\frac{\partial \rho \mathbf{u}}{\partial t} + \nabla \cdot (\rho \mathbf{u} \otimes \mathbf{u}) + \nabla P = -\rho \nabla \phi, \quad (4.11)$$

$$\frac{\partial \rho e}{\partial t} + \nabla \cdot [\rho \mathbf{u} (e + P/\rho)] = -\rho \mathbf{u} \cdot \nabla \phi, \quad (4.12)$$

$$P = P(\rho, \rho e). \quad (4.13)$$

Neglecting gravitational source terms these equations express the conservation of the quantities  $(\rho, \rho \mathbf{u}, \rho e)$ , i.e. mass, momentum and total energy per unit volume, respectively.

When writing this set of equations in comoving coordinates, using conformal time  $\tau$  and peculiar velocities  $\mathbf{v} = \mathbf{u} - H\mathbf{r}$ , new terms due to the expansion appear in the equations. Cosmological simulations usually employ super-comoving variables [109], that are defined so that the expansion of the background does not appear explicitly in the equations. By defining:

$$d\tilde{\tau} = H_0 \frac{d\tau}{a^2}, \quad (4.14)$$

$$\tilde{x} = \frac{1}{a} \frac{x}{L}, \quad (4.15)$$

$$\tilde{\rho} = a^3 \frac{\rho}{\Omega_m \rho_c}, \quad (4.16)$$

$$\tilde{P} = a^5 \frac{P}{\Omega_m \rho_c H_0^2 L^2}, \quad (4.17)$$

$$\tilde{v} = a \frac{v}{H_0 L}, \quad (4.18)$$

$$\tilde{\phi} = a^2 \frac{\phi}{H_0^2 L^2}, \quad (4.19)$$

it is possible to show that all the equations remain in the form given in Eq.s (4.10)-(4.12) except for a friction term in the energy equation, that can be

treated as a source, while the Poisson equation reads:

$$\nabla^2 \tilde{\phi} = \frac{3}{2} a \Omega_m (\tilde{\rho} - 1). \quad (4.20)$$

In the context of cosmological simulations Eulerian methods for fluids are coupled to PM methods (or AMR methods) for DM, so that the components share the same grid, and the Poisson equation is sourced by the total energy density.

Eq.s (4.10)-(4.12) can be written in compact form as:

$$\mathbf{U}_\tau + \mathbf{F}_x(\mathbf{U}) = \mathbf{S}(\mathbf{U}), \quad (4.21)$$

where indices denote derivatives. This can be solved by splitting the problem in two steps: the solution of the homogeneous system  $\mathbf{U}_\tau + \mathbf{F}_x(\mathbf{U}) = 0$  and of the ODE  $\mathbf{U}_\tau = \mathbf{S}(\mathbf{U})$ . In the RAMSES code the homogenous system is solved using a second-order Godunov scheme and the ODE with a predictor-corrector scheme. We introduce these methods here since we are going to use similar methods for clustering Dark Fluids presented in Chapter 8.

Godunov methods are finite volume methods that rely on the evaluation of state variables ( $\rho, \rho \mathbf{u}, \rho e$ ) at cell interfaces by solving the associated Riemann problem. The fluxes are computed using these evaluated states and their spatial derivatives are then computed with finite differences. Let us restrict for simplicity to the 1D case. Eq.(4.21) is discretised at first order as:

$$\tilde{\mathbf{U}}_i^{n+1} = \mathbf{U}_i^n + \frac{\Delta t}{\Delta x} (\mathbf{F}_{i+1/2}^n - \mathbf{F}_{i-1/2}^n) \quad (4.22)$$

$$\mathbf{U}_i^{n+1} = \tilde{\mathbf{U}}_i^{n+1} + \Delta t \mathbf{S}(\tilde{\mathbf{U}}_i^{n+1}) \quad (4.23)$$

where  $\mathbf{U}_i^n$  is the value of the state variables at time-step  $n$  at the centre of the grid cell  $i$ . The fluxes  $\mathbf{F}_{i+1/2}^n$  are computed as  $\mathbf{F}(\mathbf{U}_{i+1/2}^n)$ , where  $\mathbf{U}_{i+1/2}^n$  is obtained by sampling at  $x_{i+1/2}$  the solution of the Riemann problem:

$$\mathbf{U}_\tau + \mathbf{F}_x(\mathbf{U}) = 0 \quad (4.24)$$

$$\mathbf{U}(x, 0) = \begin{cases} \mathbf{U}_L & \text{if } x - x_{i+1/2} < 0 \\ \mathbf{U}_R & \text{if } x - x_{i+1/2} > 0 \end{cases} \quad (4.25)$$

where  $\mathbf{U}_L$  and  $\mathbf{U}_R$  are the values of the state variables at the left and right of the interfaces. The solution of the Riemann problem is a system of  $l$  waves, where  $l$  is the number of equations of the system, that propagate

from the interface at different velocities depending on their nature (i.e. shock, rarefaction or contact waves). By imposing the CFL condition:

$$\Delta t = \frac{C_{cfl}\Delta x}{S_{max}}, \quad (4.26)$$

where the coefficient  $0 < C_{cfl} \leq 1$  and  $S_{max}$  is the maximum wave speed, we make sure that waves arising at the interfaces do not travel for more than  $\Delta x$ .

The simplest method to evaluate  $\mathbf{U}_L$  and  $\mathbf{U}_R$  at  $x_{i+1/2}$  is to consider the states as constant inside the cells, so that  $\mathbf{U}_L = \mathbf{U}_i$  and  $\mathbf{U}_R = \mathbf{U}_{i+1}$ . This method is called Piecewise Constant Method and is first-order accurate. Second-order Godunov methods reconstruct the value of the state at the interface using different approximations: the Piecewise Linear Method uses first order Taylor expansions of the data to reconstruct the state at  $i+1/2$  and  $n+1/2$ , while the Piecewise Parabolic Method uses parabolic reconstruction. These reconstructed states are then used as initial conditions for the Riemann Problem. The order of the method used to solve the ODE problem  $\mathbf{U}_\tau = \mathbf{S}(\mathbf{U})$  must be the same of the Godunov method, thus at second order the typical discretisation scheme is:

$$\mathbf{U}_i^{n+1/2} = \mathbf{U}_i^n + \frac{1}{2}\Delta t \mathbf{S}(\mathbf{U}_i^n) \quad (4.27)$$

$$\tilde{\mathbf{U}}_i^{n+1} = \mathbf{U}_i^{n+1/2} + \frac{\Delta t}{\Delta x} (\mathbf{F}_{i+1/2}^{n+1/2} - \mathbf{F}_{i-1/2}^{n+1/2}) \quad (4.28)$$

$$\mathbf{U}_i^{n+1} = \tilde{\mathbf{U}}_i^{n+1} + \frac{1}{2}\Delta t \mathbf{S}(\tilde{\mathbf{U}}_i^{n+1}) \quad (4.29)$$

where we have used Strang splitting for source terms [159]. For a detailed presentation of Godunov methods see [171].

### 4.3 Generation of initial conditions

Initial conditions for cosmological simulations are generated at high redshift, usually  $> 30$ , where the Zel'dovich approximation is still valid on the scales of interest. As we have seen in §3.1 at early times the fluctuation field  $\delta$  is a homogeneous and isotropic Gaussian random field. For such a field, a particular realisation can be written as:

$$\delta(\mathbf{x}) = \frac{1}{(2\pi)^3} \int d^3k \sqrt{P(k)} \lambda_{\mathbf{k}} e^{i\mathbf{k}\cdot\mathbf{x}}, \quad (4.30)$$

where  $\lambda_{\mathbf{k}}$  is a white noise field, i.e. a complex Gaussian random field that satisfies the independence condition:

$$\langle \lambda_{\mathbf{k}_1} \lambda_{\mathbf{k}_2}^* \rangle = (2\pi)^3 \delta_D(\mathbf{k}_2 - \mathbf{k}_1). \quad (4.31)$$

Since  $\delta(\mathbf{x})$  is real the white noise is also subject to the Hermitian condition:

$$\lambda_{\mathbf{k}}^* = \lambda_{-\mathbf{k}}. \quad (4.32)$$

Eq.(4.30) is used in the Zel'dovich approximation to generate the initial particle displacement. A realisation of the  $\lambda_{\mathbf{k}}$  field can be obtained by drawing Gaussian random numbers with zero mean and unity variance at each grid-point. This field is then multiplied by the square-root of linear power spectrum for the desired cosmology, which can be computed using Boltzmann codes like CAMB [105] or CLASS [103]. Once the density field is constructed, the velocity field is computed using linear theory:

$$\mathbf{v} = -i a \frac{\dot{D}_+}{D_+} \frac{\mathbf{k}}{k^2} \delta. \quad (4.33)$$

FFT methods are used to Fourier transform the obtained density and velocity fields in configuration space. Once chosen a pre-initial configuration of particles, positions and velocities are evolved to the initial redshift of the simulation using Zel'dovich approximation. The displacement field is computed as:

$$\mathbf{s} = \frac{\mathbf{v}}{a \dot{D}_+}, \quad (4.34)$$

and particle positions and velocities are given by:

$$\mathbf{x}_p(a) = \mathbf{q} + D_+ \mathbf{s}(\mathbf{q}), \quad (4.35)$$

$$\mathbf{v}_p(a) = a \dot{D}_+ \mathbf{s}(\mathbf{q}), \quad (4.36)$$

where  $\mathbf{q}$  is the pre-initial position of the particle. In the simplest approach particles are placed at the position of grid-points, but in some cases their pre-initial configuration can be chosen not to coincide with the grid (e.g. glass configurations [183]). In such cases an additional interpolation of the velocity field to particle positions is required to compute the displacement.

## 4.4 Power spectrum estimation

The power spectrum defined in Eq.(3.16) is a continuous quantity, but for all practical purposes it is discretised in  $k$  bins of finite width  $\Delta k$ . Common

binning strategies include linear and logarithmic binning, the number of bins depending on the application. For cosmological simulations the binned power spectrum is obtained by Fourier transforming the density field and taking the average of its amplitude for all the wave-vectors that fall in a given  $k$  bin. The discrete version of the 3D Fourier transform for the density field is:

$$\tilde{\rho}_{lmn} = \sum_i^{N_g} \sum_j^{N_g} \sum_k^{N_g} \rho_{ijk} e^{i \frac{2\pi}{N_g} (il+jm+kn)}, \quad (4.37)$$

where  $\rho_{ijk}$  is the value at the grid-point  $(i, j, k)$  and  $\tilde{\rho}_{lmn}$  is its Fourier transform at the eigenvector:

$$\mathbf{k} = \frac{2\pi}{L}(l, m, n). \quad (4.38)$$

We define the estimator of the power spectrum as:

$$\hat{P}(k) = \langle |\tilde{\rho}_{lmn}|^2 \rangle_{k \in \Delta_k}, \quad (4.39)$$

where:

$$k = \frac{2\pi}{L} \sqrt{l^2 + m^2 + n^2} \quad (4.40)$$

$$\text{and } \Delta_k = \left\{ k - \frac{\Delta k}{2}, k + \frac{\Delta k}{2} \right\}. \quad (4.41)$$

In this approach the largest wavenumber one can sample is determined by the Nyquist frequency of the grid  $k_{max} = \pi N_g/L$ , while the smallest is set by the fundamental mode of the grid  $k_{min} = 2\pi/L$ .

The power spectrum measured from N-body simulations is affected by numerical systematics, due to the fact that simulations follow the evolution in a smaller volume than the observable universe, and due to the discrete representation of the density field with particles. In a finite box a mode of amplitude  $k$  is sampled a number of times given by:

$$N_k = \frac{V_{shell}}{V_f} \approx \frac{4\pi k^2}{\Delta k^2}, \quad (4.42)$$

where  $V_{shell}$  is the volume of a spherical shell in Fourier space of radius  $k$  and width  $\Delta k$  and  $V_f$  is the fundamental volume in  $k$ -space given by  $\Delta k^3$ . This means that the power spectrum estimate is affected by sampling error, that for a Gaussian density field is given by:

$$\sigma_P(k) = \sqrt{\frac{2}{N_k}} P(k). \quad (4.43)$$

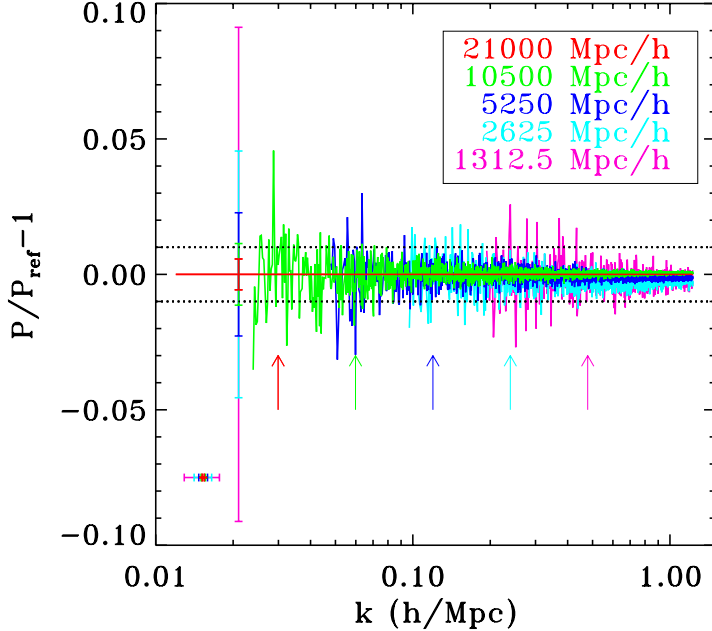


**Figure 4.1:** Relative difference of the matter power spectra at  $z = 0$  from simulations of different box-lengths with respect to that from DEUS-FUR with  $L = 21000 \text{ Mpc } h^{-1}$  (red line). The various lines correspond to the simulations with box-length  $L = 10500 \text{ Mpc } h^{-1}$  (green line),  $L = 5250 \text{ Mpc } h^{-1}$  (light-blue line),  $L = 2625 \text{ Mpc } h^{-1}$  (dark-blue line) and  $L = 1312.5 \text{ Mpc } h^{-1}$  (magenta line) respectively. All curves are truncated outside the range where  $\sigma_P/P > 0.01$ . The vertical error bars at  $k = 0.02 \text{ Mpc } h^{-1}$  show  $\sigma_P$ , while the horizontal ones give the wavenumber bin size for the different simulation box-lengths respectively. The arrows mark the wavenumber values where  $\Delta k$  is 1% of  $k$ . From Ref. [134].

This approximation is not valid for high  $k$ , where, as we will see in Chapter 5, strong deviations from Eq.(4.43) arise due to coupling of modes that develop during the non-linear regime. At low  $k$  the modes are sampled few times, giving rise to large sample variance. Figure 4.1 shows the relative difference between power spectra from simulations of different box-lengths with respect to the spectrum of the largest one. Spectra are truncated at the  $k$  value above which sampling variance is below the 1% level. We can see the increasing level of noise at fixed  $k$  with decreasing box-lengths. Sample variance can be reduced by using volumes much larger than the scales of interest or running several realisations of the same cosmological model and averaging the power spectra. Another type of finite volume effect is due to the absence of modes

larger than the box size in the simulation. For relatively small box-lengths (below  $250 \text{ Mpc } h^{-1}$ ) these modes are coupled to small scale modes at low redshift, where non-linearities become important. The missing coupling contribution delays the onset of non-linearities at scales close to the box size [82]. This results in a suppression of power at small  $k$ , that is usually buried under the noise due to sample variance. This effect is shown in Figure 4.2, where multiple realisations are averaged to achieve the same low level of sample variance for the different box-lengths.

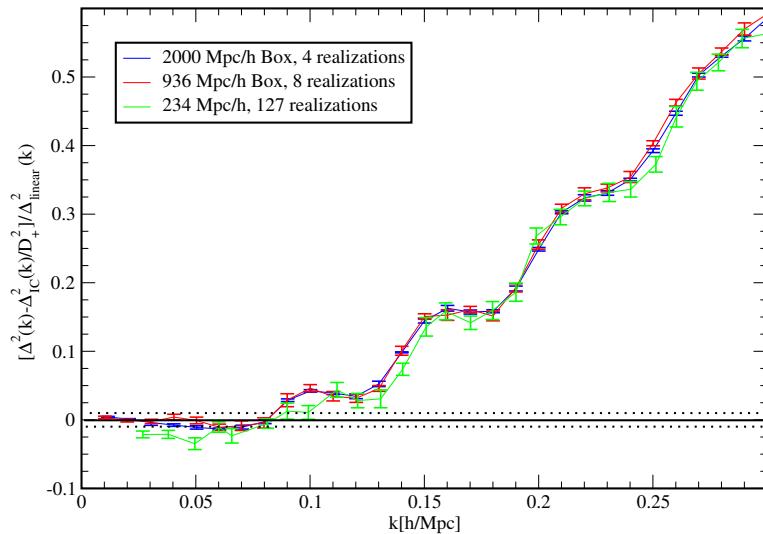


**Figure 4.2:** Comparison of power spectra from three different box sizes,  $2000 \text{ Mpc } h^{-1}$  (blue),  $936 \text{ Mpc } h^{-1}$  (red) and  $234 \text{ Mpc } h^{-1}$  (green). The initial power spectrum scaled to  $z = 0$  is subtracted from the final power spectrum and the result is averaged over all realisations (4 for the big box, 8 for the medium box, and 127 for the small box), and divided by the smooth prediction from linear theory. The error bars show the standard deviation. The overall agreement of  $\Delta^2(k)$  from the two large box sizes is better than 1% on scales below  $k \sim 0.1 \text{ h Mpc}^{-1}$  (the 1% limit is shown by the dotted lines). The small box result displays an overall suppression of the power spectrum at low  $k$ . From Ref. [82].

Discreteness effects in PM codes are due to errors in the computation of the force, which are controlled by the size of the grid cell. At high redshift most of the volume is occupied by matter with density close to the mean. In this low density contrast regime the errors are the largest since small overdensities are spread over the volume of a cell, thus diluting the gravitational attraction towards that cell. Nevertheless, AMR techniques allow to refine

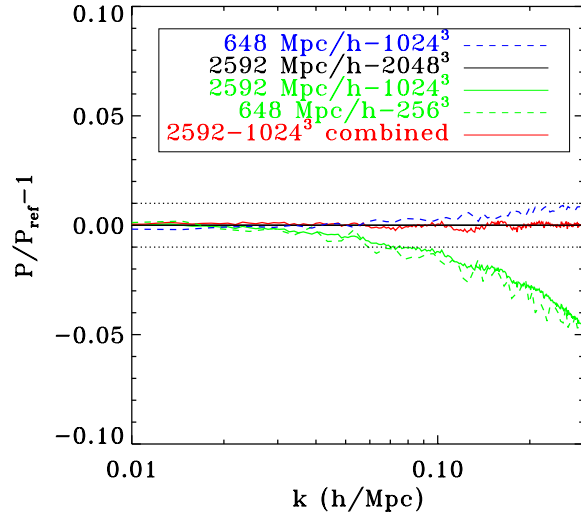


**Figure 4.3:** Relative difference of the matter power spectra at  $z = 0$  from simulations with  $m_p = 1.2 \times 10^{12} h^{-1} M_\odot$  (green lines),  $m_p = 1.5 \times 10^{11} h^{-1} M_\odot$  (black line) and  $m_p = 1.8 \times 10^{10} h^{-1} M_\odot$  (blue line) respectively. The reference spectrum is given by the simulation with  $m_p = 1.5 \times 10^{11} h^{-1} M_\odot$ . The red line corresponds to spectrum of the simulation with  $1024^3$  particles and  $2592 h^{-1} \text{Mpc}$  box-length corrected for the mass resolution effect. From Ref. [134].

the computation of the force in high density regions, giving rise to a more accurate estimation of the power spectrum at low redshift, where most of the matter is in collapsed structures. It is customary for cosmological AMR simulations to set the number of coarse grid cells to be equal to the number of particles, thus casting this problem in a mass resolution error framework. Moreover, refinement criteria are based on the number of particles in the cell, linking the mass resolution to the accuracy of the computation of the force. This mass resolution effect manifests as a depletion of power at high  $k$ , as shown in Figure 4.3, and is more important at higher redshifts. In Ref. [134] the spectrum of low resolution runs has been corrected using the spectrum of higher resolution ones. The mass resolution effect is in fact a smooth function of  $k$ , so it can be estimated by taking the ratio of the spectra of two simulations with the same volume and different mass resolution and then fitting it with a polynomial function. The correction yields an accurate spectrum, as it can be seen from the red curve in Figure 4.3. As we will see in the next Chapter mass resolution effects also affect the power spectrum covariance matrix computed from low resolution simulations.

## Part II

# Cosmology with large volume galaxy surveys



## Chapter 5

# Cosmological dependence of the large scale structure of the universe

The galaxy distribution contains cosmological information. In fact galaxies result from the collapse of the baryonic gas in the potential well generated by matter density fluctuations. Thus, luminous matter in the universe is a tracer of the underlying matter density field, so that measurements of the statistical properties of the galaxy distribution provide information on those of the matter field. Surveys of the large scale structures have been providing insightful data for more than a decade now. Observational projects such as the 2-degree Field Galaxy Redshift Survey (2dFGRS) [127, 39] and the Sloan Digital Sky Survey (SDSS) [167] have yielded unprecedented measurements of the clustering of matter on the large scales. The success of these projects has opened the way to a new generation of survey programs. In the years to come the Dark Energy Survey<sup>1</sup> (DES), the Large Synoptic Survey Telescope<sup>2</sup> (LSST) or the Euclid mission<sup>3</sup> will map the distribution of galaxies in larger cosmic volumes and with higher sensitivity.

In this thesis we focus on two particular Large Scale Structure (LSS) observables: the galaxy power spectrum, that we will describe in §5.1, and the Baryon Acoustic Oscillations (BAO) in §5.2. Our goal is to use numerical N-body simulations to study non-linear effects of the late time clustering of matter on both probes.

---

<sup>1</sup>[www.darkenergysurvey.org](http://www.darkenergysurvey.org)

<sup>2</sup>[www.lsst.org](http://www.lsst.org)

<sup>3</sup>[www.euclid-ec.org](http://www.euclid-ec.org)

To infer constraints on the cosmological parameters from these observables it is necessary to interpret the data in a statistical framework. Bayesian techniques are the standard ones in cosmology since they allow to incorporate previous constraints through priors and combine different probes in a statistically consistent way. We will present these techniques in §5.3.

## 5.1 Galaxy power spectrum

Luminous matter is a biased tracer of the matter density field, since it is more probable for galaxies to form in over-density regions than in under-dense ones. Moreover, the clustering of galaxies may differ depending on galaxy properties (e.g. type, luminosity, colour), thus leading to different bias effects [see e.g. 187]. Galaxy bias is usually modelled linearly as  $\delta_g = b \delta_m$ , where  $\delta_g$  is the galaxy number density contrast and  $b$  is the bias factor. Using semi-analytical methods it is possible to show that at early times galaxies form in high-density peaks which are more strongly clustered than the underlying dark matter field [15] so that  $b > 1$ . At later times this bias decreases, making galaxies a better tracer over time [71, 168]. In general the bias factor is scale-dependent but this dependence is weak and is well approximated by a constant factor at large scales [108]. In principle the bias of a given galaxy sample can be estimated by taking the ratio of the clustering of the observed sample to the one of dark matter in a cosmological simulation. However, such an estimate is cosmology-dependent, with  $b$  being strongly degenerate with the  $\sigma_8$  parameter, thus extracting cosmological information from the sample using this method can bias the analysis. For this reason  $b$  is usually treated as a “nuisance” parameter and fitted together with the cosmological parameters.

In addition to bias, galaxies are discrete samples of the density field. Hence, measurements of their statistical properties are affected by shot-noise errors. Under the assumption that galaxies form a Poisson sample of the density field [124] the contribution of shot-noise to the power spectrum is a term  $1/\bar{n}$ , where  $\bar{n}$  is the mean galaxy density. We can thus model the estimator for the galaxy power spectrum as:

$$\hat{P}_g(k) = b^2 \langle |\delta_m(k)|^2 \rangle - \frac{1}{\bar{n}}. \quad (5.1)$$

Given the level of shot-noise of current galaxy surveys, only the largest scales can be used to infer cosmological parameters. Since these scales are in linear or mildly non-linear regime, predictions from LPT or higher-order PT are sufficient to make accurate theoretical predictions that can be compared to the data. On the other hand, smaller scales are sampled with lower

cosmic variance errors and also carry cosmological information, however for these to be accessible will require taking into account complex effects such as non-linearities and baryonic feedback [see e.g. 140]. This is crucial since upcoming surveys will observe larger numbers of galaxies, bringing shot noise errors below the level of sample variance especially at small scales.

For the purposes of this thesis we will assume that both bias and baryonic effects can be treated as nuisance parameters and focus on the effect of non-linearities on the matter power spectrum and its covariance matrix.

## 5.2 Baryon Acoustic Oscillations

Prior to recombination small scale perturbations in the baryonic component propagate as acoustic waves, which then stall at decoupling and start accumulating baryons at fixed distances from the original perturbations [17, 18] leaving a characteristic imprint on the matter distribution. We can define the sound horizon as the maximum distance that such waves can travel until recombination:

$$s = \int_0^{t(z_{rec})} c_s(1+z)dt, \quad (5.2)$$

where  $c_s$  is the sound speed of the baryon-photon plasma:

$$c_s = \frac{c}{[3(1+\eta)]^{1/2}} \quad (5.3)$$

and  $\eta = 3\rho_b/4\rho_\gamma$  is the ratio of the baryon to photon momentum density. The scale  $s$  is imprinted in the matter correlation function as a single peak at  $s \sim 100 \text{ Mpc } h^{-1}$ , while on the power spectrum it manifests as a series of peaks and troughs at wave-numbers  $k = n\pi/2s$  for  $n = 5, 9, 13, \dots$  and  $n = 3, 7, 11, \dots$  respectively. This is similar to the Fourier transform of the step function being spread over a series of damped oscillations in Fourier space.

Since we have a precise estimate of the scale  $s$  at recombination thanks to CMB observations, we can calibrate the scale of the BAO to be a standard ruler. The comoving size of an extended object or feature in the directions perpendicular and orthogonal to the line-of-sight is given by:

$$r_{\parallel} = \frac{c\Delta z}{H(z)}, \quad (5.4)$$

$$r_{\perp} = (1+z)D_A(z)\Delta\theta, \quad (5.5)$$

thus by measuring the scale of the BAO at redshifts probed by galaxy surveys in these two directions we can estimate  $H(z)$  and  $D_A(z)$  as a function of redshift. The BAO feature has first been detected in the SDSS and 2dFGRS surveys [63, 126], yielding estimates of the distance to the redshift of the surveys with a few % precision. The Baryon Oscillation Spectroscopic Survey [BOSS, 54] has recently determined the cosmic distance scale to one percent accuracy from measurements of the BAO spectrum in the range of modes  $0.01 < k[h \text{ Mpc}^{-1}] < 0.30$  [9]. Future surveys such as LSST or Euclid will push these measurements even further, aiming to achieve sub-percent precisions. This requires to address a series of effects of different nature, such as Silk damping, redshift-space distortions and non-linearities, that shift and damp the oscillations. Current measurements rely on reconstruction techniques [65], where non-linear effects are erased to gain signal, but as we will see in the next section these signatures carry cosmological information, and if modelled accurately can give independent cosmological constraints.

### 5.2.1 Non-linear effects on BAO

Non-linear processing of the matter power spectrum in the epoch between recombination and the redshifts probed by galaxy surveys distorts the signal of the BAO in two ways: the oscillations are damped and the overall slope of the spectrum is modified, causing a shift of the oscillatory pattern in a  $k$  dependent way. In Ref. [134] a careful assessment of the non-linear effects on the BAO pattern has been made using the DEUS-FUR large volume numerical simulations. These simulations have a volume of  $21 \text{ Gpc } h^{-1}$  that contains the scale of the horizon today. This allows to have cosmic variance limited estimates of the BAO feature in the matter power spectrum and thus to study non-linear effects with great accuracy. The BAO signal of the DEUS-FUR  $\Lambda\text{CDM}$  simulation at  $z = 0$  is shown in Fig. 5.1, where the smooth power spectrum has been subtracted to isolate the oscillatory pattern. Predictions of some approximated methods are shown for comparison. Here the smooth power spectrum is found by running a simulation with a wigggle-free initial power spectrum given by the Eisenstein & Hu fitting formulae [64]. The main difference between the various methods is the predicted broad-band slope of the spectrum, thus it is useful to show the difference between the full power spectrum and the smooth one predicted by each model, shown in Fig. 5.2. This highlights the difference in the predictions of the BAO oscillations alone. By comparing the measured signal in the simulation with the linear prediction we see that the shift in the peaks position due to non-linearities is a few per cent effect at all redshifts, while damping is the dominant effect and grows from high to low redshift. This is illustrated in Fig. 5.3, where the

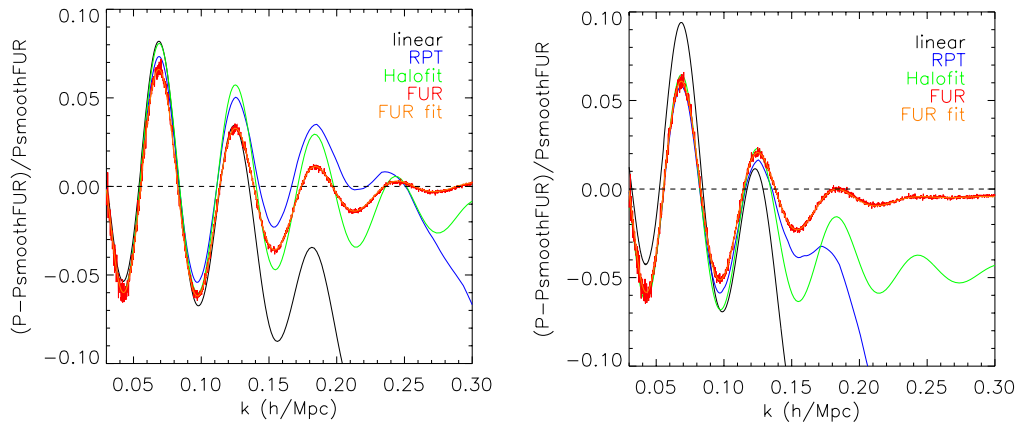


**Figure 5.1:** Relative difference of the BAO power spectrum to  $P_{\text{smooth}}^{\text{FUR}}(k)$  at  $z = 1$  (left panel) and  $0$  (right panel). The different lines correspond to the linear prediction (black line), RegPT (blue line), Halofit (green line), DEUS-FUR (red line) and DEUS-FUR fit (orange line) respectively. From Ref. [134].

shift and damping are shown for all the detectable peaks and troughs. The second trough and the third peak are the most stable features, making them the most suited for precise cosmological parameter inference. Perturbation theory predicts that damping evolves as the square of the linear growth factor [52, 123, 148], which is shown as dashed lines in the right panel of Fig. 5.3. These are in good agreement with the results from the simulation. Thus, by measuring the damping of the BAO oscillations in the observed spectra of future surveys it will be possible to have an additional independent cosmological constraint.

### 5.3 Bayesian methods for cosmological parameter inference

Modern cosmological data analysis is performed in a Bayesian inference framework. This allows to incorporate observational errors and combine different observables in a statistically consistent way. In this context the parameters  $\boldsymbol{\theta}$  of a given model  $M$  are taken as random variables and the Bayes theorem is formulated as:

$$P(\boldsymbol{\theta}|\mathbf{D}, M) = \frac{P(\mathbf{D}|\boldsymbol{\theta}, M) P(\boldsymbol{\theta}|M)}{P(\mathbf{D}|M)}, \quad (5.6)$$

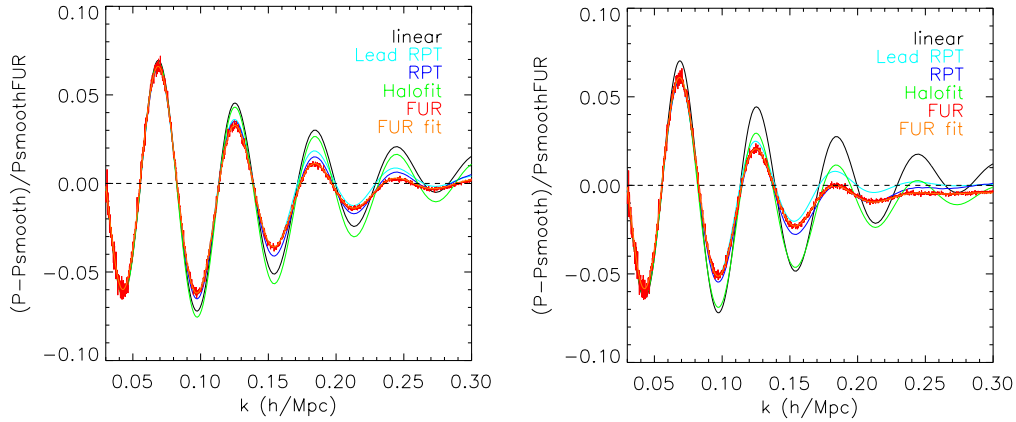


**Figure 5.2:** Difference with respect to the smooth spectrum of each model normalised to  $P_{\text{smooth}}^{\text{FUR}}(k)$  at  $z = 1$  (left panel) and  $0$  (right panel). The different lines correspond to the linear prediction (black line), RegPT (blue line), Halofit (green line), the leading term from Renormalized Perturbation Theory (light blue line), DEUS-FUR (red line) and DEUS-FUR fit (orange line) respectively. From Ref. [134].

where  $\boldsymbol{\theta}$  is the set of parameters,  $\mathbf{D}$  are the data,  $P(\boldsymbol{\theta}|\mathbf{D}, M)$  is the posterior,  $P(\mathbf{D}|\boldsymbol{\theta}, M)$  is the likelihood,  $P(\boldsymbol{\theta}|M)$  is the prior and  $P(\mathbf{D}|M)$  is the model evidence. The prior contains the previous knowledge about the model, coming either from theoretical considerations or from past data, and the posterior represents the state of knowledge of the parameters  $\boldsymbol{\theta}$  updated with the data  $\mathbf{D}$ . The likelihood function has to be constructed from a statistical model of the data and the instrumental errors. Here the model evidence can be considered as a normalisation constant. The maximum of the posterior probability in the parameter space represents the best fit parameters of the model. It is possible to draw contours of credibility that encompass the 68% or 95% of the posterior probability around the maximum.

It is possible to extend this formalism to “model selection” problems, where different models  $M_i$  with different sets of parameters  $\boldsymbol{\theta}_i$  can be compared by means of their evidence:

$$P(\mathbf{D}|M_i) = \int P(\mathbf{D}|\boldsymbol{\theta}_i, M_i)P(\boldsymbol{\theta}_i|M_i)d\boldsymbol{\theta}_i, \quad (5.7)$$

where each model has its set of priors  $P(\boldsymbol{\theta}_i|M_i)$ . The model posterior is then built using Bayes theorem in the form:

$$P(M_i|\mathbf{D}) \propto P(\mathbf{D}|M_i)P(M_i), \quad (5.8)$$

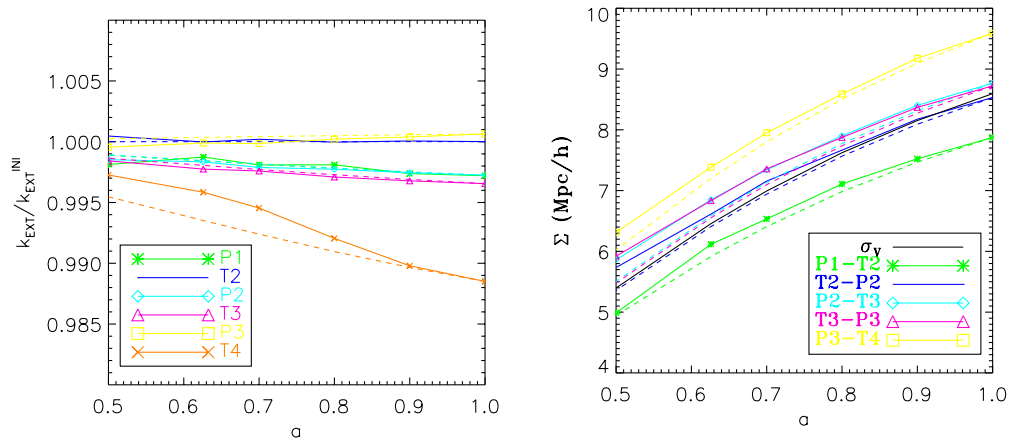


**Figure 5.3:** Left panel: evolution of the shift of BAO extrema as a function of the scale factor  $a$ . The different solid lines correspond to peaks (P) and troughs (T) as in the legend, while the dashed lines show the square of the linear growth function  $D_+^2(a)$  from perturbation theory. Right panel: evolution of the damping factor of BAO extrema as a function of the scale factor. The black solid line shows the evolution of the effective one-dimensional amplitude of large-scale velocity flow  $\sigma_v(a)$ , while the dashed lines corresponds to  $D_+(a)$  scaling of the damping of the BAO extrema as expected from perturbation theory. From Ref. [134].

where  $P(M_i)$  is the prior on the model. This method can be useful when comparing models with different numbers of parameters, e.g. for distinguishing dynamical DE models from  $\Lambda$ CDM [119].

### 5.3.1 Maximum Likelihood Estimator

Suppose that we want to estimate the most probable value for a parameter  $\theta_\alpha$  given a dataset  $\mathbf{D}$ . When we look at a fixed dataset we can think at the likelihood as a function of the parameters, i.e.  $L(\mathbf{D}; \theta_\alpha)$ . The Best Unbiased Estimator (BUE) is the one that is unbiased, i.e.  $\langle \hat{\theta} \rangle = \theta$ , and minimises the error  $\Delta\theta = (\langle \hat{\theta}^2 \rangle - \langle \hat{\theta} \rangle^2)^{1/2}$ . The estimator that maximises the likelihood is called Maximum Likelihood Estimator (MLE) and has two properties [see e.g. 169]:

- if there is a BUE this is  $\hat{\theta}_{MLE}$  or a function of it,
- the MLE is asymptotically the BUE, i.e.  $\hat{\theta}_{MLE} \rightarrow \hat{\theta}_{BUE}$  for increasing data sample size.

Given the large volumes of data coming from galaxy surveys,  $\hat{\theta}_{MLE}$  represents the best approach to build a BUE.

From Eq.(5.6) it is clear that for uniform priors the maximum of the posterior probability coincides with the MLE.

### 5.3.2 Fisher matrix

The Fisher matrix is a measure of the information content in a given dataset  $\mathbf{D}$  on the parameters  $\boldsymbol{\theta}$  and is defined as:

$$F_{\alpha\beta} = \left\langle \frac{\partial^2 \mathcal{L}(\mathbf{D}; \boldsymbol{\theta})}{\partial \theta_\alpha \partial \theta_\beta} \right\rangle, \quad (5.9)$$

where  $\mathcal{L}(\mathbf{D}; \boldsymbol{\theta}) = -\ln L(\mathbf{D}; \boldsymbol{\theta})$  is the log-likelihood. The Cramer-Rao inequality gives us a lower limit for the variance of any unbiased estimator of a parameter:

$$\sigma^2(\hat{\theta}_\alpha) \geq [F^{-1}]_{\alpha\alpha}, \quad (5.10)$$

so that the inverse of the Fisher matrix can be considered as the best precision achievable for a parameter estimate. The equality is reached when the estimator is the BUE.

The Fisher matrix is used for forecasting the ability of a given survey to constrain the parameters of a given model. The idea is to simulate the data by including instrumental errors and study the shape of the posterior around the true parameter values. Expanding the likelihood in a Taylor series around the MLE, i.e. in the variable  $\delta\boldsymbol{\theta} = \hat{\boldsymbol{\theta}}_{MLE} - \boldsymbol{\theta}$ , at second order we get:

$$L(\mathbf{D}; \boldsymbol{\theta}) \sim \exp\left(-\frac{1}{2} \sum_{\alpha\beta} F_{\alpha\beta} \delta\theta_\alpha \delta\theta_\beta\right), \quad (5.11)$$

which corresponds to a Gaussian likelihood with zero mean and covariance given by the inverse of the Fisher matrix:

$$F_{\alpha\beta} = \sum_{ij} \frac{\partial D_i}{\partial \theta_\alpha} [\text{cov}^{-1}]_{ij} \frac{\partial D_j}{\partial \theta_\beta}, \quad (5.12)$$

where cov is the data covariance. The error on a parameter  $\theta_\alpha$  is then  $\sigma(\theta_\alpha) = ([F^{-1}]_{\alpha\alpha})^{1/2}$ . Notice that this estimate of the error depends on the fiducial model parameters, i.e. our best guess of the MLE parameters  $\hat{\boldsymbol{\theta}}_{MLE}$ . This means that these errors cannot be used to forecast the ability of an experiment to rule out a given model, but rather to have an estimate of the minimum achievable error-bars on the parameters within a given model.

See Ref. [119] for an extension of Fisher parameter forecast to model selection using Bayes factors.

In the Gaussian likelihood approximation, assuming that we have perfect knowledge of a parameter comes down to eliminating the corresponding row and column of the Fisher matrix, while marginalising over a parameter is done by eliminating the corresponding row and column of the inverse of the Fisher matrix. This simplicity is what makes Fisher matrix forecasts so popular. Moreover, for the Central Limit theorem the likelihood will tend to a Gaussian distribution for large data-sets, justifying the approximation Eq. 5.11.

### 5.3.3 Information content of galaxy surveys

If we make the more realistic assumption that the parameters  $\boldsymbol{\theta}$  will be estimated through an observable  $O(\mathbf{D})$ , which is a function of the data, with a given unbiased estimator  $\hat{O}$ , the Cramer-Rao inequality reads:

$$\text{cov}(\hat{O}) \geq \left[ \frac{\partial O}{\partial \boldsymbol{\theta}} \right]^T F^{-1} \frac{\partial O}{\partial \boldsymbol{\theta}}, \quad (5.13)$$

where  $^T$  stands for transpose. This can be recast as:

$$F(\boldsymbol{\theta}) \geq \left[ \frac{\partial O}{\partial \boldsymbol{\theta}} \right]^T \text{cov}(\hat{O})^{-1} \frac{\partial O}{\partial \boldsymbol{\theta}}. \quad (5.14)$$

From Eq.(5.14) we can see that the information content on a given observable  $O$  (the right-hand side) is always less than the total information content of the data on the parameters (the left-hand side). This expression can be generalised to a set of observables  $\mathbf{O}$  as:

$$F(\boldsymbol{\theta}) \geq \sum_{ij} \frac{\partial O_i}{\partial \boldsymbol{\theta}} [\text{cov}^{-1}]_{ij} \frac{\partial O_j}{\partial \boldsymbol{\theta}}. \quad (5.15)$$

As we have seen in §3.1, the density contrast field can be decomposed in a series of connected N-point correlation functions, or connected moments of the field. It can be shown that if we consider as observables  $\mathbf{O}$  the series of correlation functions, Eq.(5.15) becomes an equality, provided that the moment series is determinate, that is to say that the density can be uniquely recovered from the moment series [42, 36]. For Gaussian distributed density fields this means that the full information can be recovered from measurements of the first two moments. Non-linearities distort the distribution function of  $\delta$

making it more tailed towards high  $\delta$  values. In general for tailed distribution the information content in the moment hierarchy converges less rapidly (or is not determinate, thus never converges), making it an inefficient set of observables to extract information about the  $\delta$  field [36].

## 5.4 Contributions of this thesis

In Chapter 6 we present a study of the estimator of the band-averaged matter power spectrum (or band-powers) using N-body simulations. Weak-lensing observables, BAO and the galaxy power spectrum measurements all rely on modelling of the matter power spectrum to make theoretical predictions. We place ourselves in the formalism of §5.3.2, where the simulated spectra are considered as data, so that their distribution over a set of realisations is proportional to the likelihood  $P(D|\theta, M)$ . We show that in non-linear regime the band-powers have highly correlated errors, making estimation of their covariance matrix necessary for unbiased parameter inference. Moreover, the probability distribution function deviates significantly from the Gaussian distribution, indicating that the likelihood is not well approximated by Eq. (5.11). This means that data analysis of future galaxy surveys will require estimates of the shape of the likelihood function for observables in the non-linear regime. We leave a detailed study of the impact of non-Gaussianities on parameter estimation to future work.

In Chapter 7 we focus on the sample covariance estimator for the data covariance matrix and its inverse, the precision matrix. Assuming that the sample covariance computed from a set of more than  $10^4$  simulations is the true covariance we study the dispersion and bias of the estimator when varying the number of simulations used, both for the covariance and the precision matrices. These can be predicted analytically for Gaussian distributed independent errors, since in this case the sample covariance is Wishart-distributed while its inverse follows an inverse-Wishart distribution. Comparison with these predictions show that the deviations from Gaussianity of the power spectrum estimator impact the distribution of the sample covariance and precision estimators, increasing their dispersion in the large  $k$  range. Finally, we use the Fisher matrix formalism to quantify the impact of correlations on the forecasted parameter errors for Euclid-like surveys. We show that using the linear prediction for the power spectrum covariance under-estimates the error on the cosmological parameters and changes the direction of degeneracies.

# Chapter 6

## Matter power spectrum covariance matrices from the DEUS-PUR simulations

An unbiased statistical analysis of measurements of the power spectrum requires estimates of the band-averaged power spectrum covariance matrix. In fact, while in the linear regime Fourier modes of the density field evolve independently and the covariance of the matter power spectrum has a simple diagonal form, at small scales and late times the covariance develops non-vanishing off-diagonal terms which account for the mode coupling caused by the non-linear regime of gravitational collapse. In such a case the errors on band powers become correlated causing a larger dispersion on power spectrum measurements [111]. Neglecting such correlations may lead to biased results as shown by several studies of weak lensing observables [see e.g. 182, 147, 99, 93] and to a biased determination of BAO parameters [see e.g. 164, 120]. Hence, the future generation of large scale structure surveys will need estimates of the covariance matrix which require sampling the matter power spectrum from large samples of N-body simulations [166].

Let us consider the formal expression of the matter power spectrum covariance matrix [see e.g. 144]:

$$\begin{aligned} \text{cov}(k_1, k_2) &= \frac{2}{N_{k_1}} P^2(k_1) \delta_{k_1, k_2} + \\ &+ \frac{1}{V} \int_{\Delta_{k_1}} \int_{\Delta_{k_2}} \frac{d^3 \mathbf{k}'_1}{V_{k_1}} \frac{d^3 \mathbf{k}'_2}{V_{k_2}} T(\mathbf{k}'_1, -\mathbf{k}'_1, \mathbf{k}'_2, -\mathbf{k}'_2), \end{aligned} \quad (6.1)$$

where  $P(k)$  is the matter power spectrum,  $N_k = V_k/V_f$  is the number of  $k$ -modes in the volume  $V$  (see Eq.(4.42) for the definition of  $V_k$  and  $V_f$ ),  $\Delta_{k_i}$

is the band power integration interval centred on the mode  $k_i$  and  $V_{k_i}$  is the integration volume in Fourier space; the integrand  $T(\mathbf{k}'_1, \mathbf{k}'_2, \mathbf{k}'_3, \mathbf{k}'_4)$  is the trispectrum of the density fluctuation field (see Eq.(3.21)). The first term in Eq.(6.1) represents the Gaussian contribution to the covariance: for a Gaussian density field the power spectrum covariance is diagonal with amplitude  $2P^2(k)/N_k$ . The second term in Eq.(6.1) represents the contribution of non-Gaussianity arising during the non-linear regime of gravitational collapse at small scales and in general is non-diagonal.

Eq.(6.1) can be rewritten as:

$$\text{cov}(k_1, k_2) = V_f \left[ \frac{2}{V_{k_1}} P^2(k_1) \delta_{k_1, k_2} + \bar{T}(k_1, k_2) \right], \quad (6.2)$$

where  $\bar{T}(k_1, k_2) = \int_{\Delta_{k_1}} \int_{\Delta_{k_2}} \frac{d^3 \mathbf{k}'_1}{V_{k_1}} \frac{d^3 \mathbf{k}'_2}{V_{k_2}} T(\mathbf{k}'_1, -\mathbf{k}'_1, \mathbf{k}'_2, -\mathbf{k}'_2)$  is the bin-averaged trispectrum. In this form it is evident that both terms of the covariance have the same scaling with the volume of the survey  $V = (2\pi)^3/V_f$ , while only the Gaussian term has an inverse dependence on the volume of the bin-shell  $V_k$ . This means that to reduce sample variance in a given survey, enlarging the volume  $V$  is more effective than reducing the size of the bins in  $k$ .

The estimation of the covariance matrix by sampling the matter power spectrum from a large ensemble of numerical N-body simulations is not exempt of systematic uncertainties. For instance, the finite volume of simulations is source of non-Gaussian errors [137] and as shown in Ref. [163] this can introduce large uncertainties even on weakly non-linear scales. We leave a detailed study of this effect to a forthcoming work. In the following, we focus on systematic errors due to the mass resolution of the simulations, which have been neglected in previous studies.

## 6.1 N-body dataset

We use the N-body simulation dataset from DEUS-PUR project. This consists of 12288 simulations of a flat  $\Lambda$ CDM model with parameters (see Table 6.1) calibrated to the WMAP-7yr data [157] of a cosmological volume of  $(656 h^{-1} \text{Mpc})^3$  with  $256^3$  particles, for a formal mass resolution of  $1.2 \times 10^{12} h^{-1} M_\odot$  (Set A), and 96 simulations of the same cosmological model and equal volume with  $1024^3$  particles, corresponding to a mass resolution of  $2 \times 10^{10} h^{-1} M_\odot$  (Set B). These runs have been realised with "A Multiple purpose Application for Dark Energy Universe Simulation" (AMADEUS)

$h$	$\Omega_m h^2$	$\Omega_b h^2$	$n_s$	$\sigma_8$
0.72	0.1334	0.02258	0.963	0.801

**Table 6.1:** DEUS-PUR cosmological model parameter values.

[5]. This workflow application includes a dynamical solver based on RAMSES [170], where the refinement criterion is set such as to allow up to 6 levels of refinement. The quoted mass resolutions are computed for the coarse level of the simulations, but where the grid is refined the effective mass resolution is higher.

The initial conditions of the simulations have been generated using the code MPGRAFIC [133], that uses the method described in §4.3. In order to avoid the generation of  $\sim 10^4$  white noises we generated 3 independent white noises in cubes of  $4096^3$  particles each that we have subsequently split into 4096 sub-cubes. The latter were then used separately to generate the initial conditions of each simulation of Set A. A similar procedure has been used to generate the initial conditions of the simulations of Set B. These have been obtained by splitting 2 different white noises of  $4096^3$  particles in 64 cubes. The initial redshift has been set such that all simulations starts with the same amplitude of density fluctuations at the scale of the grid resolution. This is a standard technique that allows to consistently compare simulations with different spatial and mass resolution. Let us denote by  $\sigma(L/N_p, z_i)$  the root-mean-square fluctuation of the linear density field at an initial redshift  $z_i$  on the scale of the grid resolution  $L/N_p$ , where  $L$  is the simulation box-length and  $N_p$  is the number of particles. Then,  $z_i$  is determined by setting  $\sigma(L/N_p, z_i)$  to an arbitrary small value and iteratively solving the algebraic equation

$$\frac{\sigma(L/N_p, z_i)}{\sigma(L/N_p, z=0)} = \frac{D_+(z_i)}{D_+(z=0)}. \quad (6.3)$$

We set  $\sigma(L/N_p, z_i) = 0.02$ , such that initial redshifts are sufficiently large to ensure the validity of the Zel'dovich approximation, but not exceedingly large such as to avoid the introduction of systematic effects due to integration of numerical noise. In the case of simulation Set A this gives  $z_i \approx 105$ , while for the higher resolution Set B we have  $z_i \approx 190$ . Such large values guarantee that transient effects [143, 51] are negligible. Table 6.2 summarises the characteristics of the DEUS-PUR simulations.

The authors of Ref. [163] have performed a study of the 3D power spectrum covariance matrix from 5000 simulations of a standard  $\Lambda$ CDM model

Set	$N_s$	$L$ (Mpc $h^{-1}$ )	$N_p$	$m_p$ ( $M_\odot h^{-1}$ )
A	12288	656.25	$256^3$	$1.2 \times 10^{12}$
B	96	656.25	$1024^3$	$2 \times 10^{10}$

**Table 6.2:** DEUS-PUR simulation characteristics:  $N_s$  is the number of realisations,  $L$  is the box-side length,  $N_p$  is the number of dark matter particles and  $m_p$  the mass resolution. Taking set A as a reference, set B has been designed to study simulation mass resolution effects on large scale structure observables.

with a  $(1000 h^{-1} \text{Mpc})^3$  volume and a mass resolution of  $4.1 \times 10^{12} h^{-1} M_\odot$ , realised with a Particle Mesh (PM) solver with no spatial refinement and initial redshift  $z_i = 20$ . For comparison our Set A has nearly 3 times more realisations which allow us to determine the covariance matrix with reduced statistical errors. Furthermore, the DEUS-PUR simulations have a mass resolution  $\sim 3$  times higher, a better spatial resolution at the level of the coarse grid by nearly a factor of 1.5 (and a factor of  $\sim 100$  at the most refined level) and start at a much higher redshift, thus allowing us to reduce the effect of numerical systematics when compared to the sample used by Ref. [163].

The workflow of the AMADEUS application has been automated to generate a large number of N-body simulations. An external script has been coded to monitor in real time the job-queue and submit new simulations as soon as other simulations have terminated. For each simulation the initial conditions, the dynamic evolution, the data reduction and measurements of the matter power spectrum and the halo mass function are controlled through the same script. A final check on the file content has been implemented to detect any error due to unexpected machine failure. Each AMADEUS script has been launched as a separate job on the ADA supercomputer <sup>1</sup> of the Institute for Development and Resources in Intensive Scientific Computing (IDRIS). Simulations of Set A were run on 8 processors Intel Sandy Bridge E5-4650 for a running time of  $\sim 1$  h per simulation, while Set B simulations took  $\sim 24$  h per simulation on 64 processors.

## 6.2 Power Spectrum & Covariance Matrix Estimators

We compute the matter power spectrum using the code POWERGRID [133]. This estimates the power spectrum in band powers from the Fourier trans-

<sup>1</sup><http://www.idris.fr/eng/ada/hw-ada-eng.html>

form of the matter density field (see §4.4). We correct the measured spectrum for the effect of smoothing due to the Cloud-In-Cell (CIC) algorithm, that is used to estimate the density contrast field from the particle distribution. We do not correct for aliasing, since varying the size of the CIC grid we find that aliasing effects are negligible below half the Nyquist frequency of the CIC grid. Since the simulations have adaptive refinement, we use a CIC grid two times finer than the coarse grid of the simulation to compute the power spectra. This means that its Nyquist frequency is given by  $k_N = 2(\sqrt[3]{N_p} \pi/L)$ , thus the range of modes in which we compute the power spectrum is given by  $k_{\min} = 2\pi/L$  and  $k_{\max} = k_N/2$ . More specifically  $k_{\min} \approx 0.01 h \text{ Mpc}^{-1}$  for both sets A and B, while  $k_{\max} \approx 1.22 h \text{ Mpc}^{-1}$  for set A and  $k_{\max} \approx 5.9 h \text{ Mpc}^{-1}$  for set B. To minimise the effect of numerical systematics we restrict our analysis to Fourier modes in the interval  $0.03 < k[h \text{ Mpc}^{-1}] < 1.00$ .

The power spectrum measured from the DEUS-PUR simulations is binned linearly with  $\Delta k \approx 0.0048 h \text{ Mpc}^{-1}$  for a total number of 202 bins up to  $k \approx 1 h \text{ Mpc}^{-1}$ . Since the outputs of the simulations are written at slightly different redshifts  $z_i$  due to numerical errors, we rescale each spectrum to the same redshift  $z$  using the linear  $D_+$ , i.e.  $P_i(z) = D_+^2(z)/D_+^2(z_i) P_i(z_i)$ .

The covariance matrix is computed using the unbiased sample covariance estimator:

$$\widehat{\text{cov}}(k_1, k_2) = \frac{1}{N_s - 1} \sum_{i=1}^{N_s} [\hat{P}_i(k_1) - \bar{P}(k_1)][\hat{P}_i(k_2) - \bar{P}(k_2)], \quad (6.4)$$

where  $N_s$  is the number of independent realisations and  $\bar{P}(k) = \sum_{i=1}^{N_s} \hat{P}_i(k)/N_s$  is the sample mean, with  $\hat{P}_i(k)$  the matter power spectrum estimation of the  $i$ -th realisation.

### 6.3 Numerical Simulation Mass Resolution Errors

In the top panel of Fig. 6.1 we plot the diagonal elements of the matter power spectrum covariance matrix normalised to the linear Gaussian amplitude  $2 P_{lin}^2(k)/N_k$  for Set A (dash lines) and B (solid lines) at  $z = 0, 0.3, 0.5, 1$  and 2 (top to bottom) respectively. Here the linear power spectrum is obtained by evolving the power spectrum generated by CAMB at the redshift of the simulation snapshots using the linear growth function  $D_+$ . As we

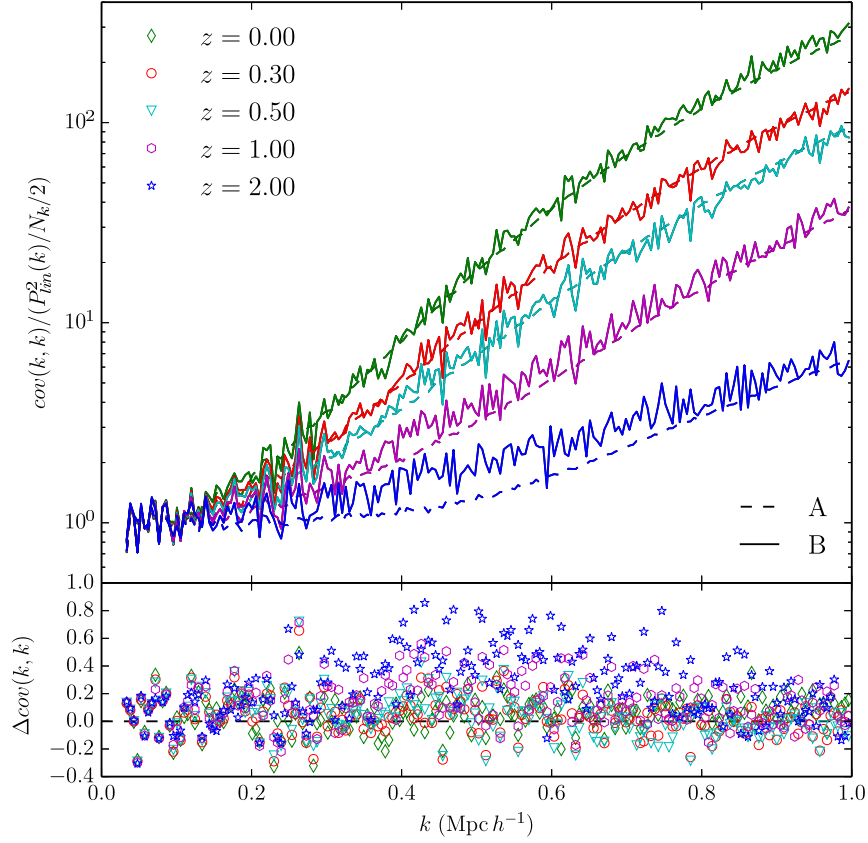


**Figure 6.1:** Top panel: diagonal elements of the covariance matrix normalised to the Gaussian variance for Set A (dashed lines) and B (solid lines) at  $z = 0$  (green), 0.3 (red), 0.5 (light-blue), 1 (magenta) and 2 (blue) respectively. Bottom panel: relative difference between Set A and B at different redshifts. The variance of Set A is under-estimated compared to that of Set B.

can see the curves corresponding to Set A are very smooth since they have negligible noise due to the large size of the simulation sample. This is not the case of Set B for which the covariance estimates are characterised by a higher level of noise. As expected, the onset of the non-linear regime causes deviations from the Gaussian prediction which occur at large  $k$ -values and shift towards smaller ones at lower redshifts. For instance, a deviation of a factor  $\sim 5$  at  $z = 1$  occurs at  $k \sim 0.55 h \text{Mpc}^{-1}$ , while at  $z = 0$  the same deviation occurs at  $k \sim 0.30 h \text{Mpc}^{-1}$ . The effect of such deviations is to increase the statistical errors on the power spectrum measurements at non-linear scales. Despite the higher level of statistical noise associated to Set B, it is evident that there is a systematic down shift of the variance of lower resolution simulations. In the bottom panel of Fig. 6.1 we can see that such a discrepancy exceeds the statistical noise of Set B at redshifts  $z > 0.5$  in the range of modes  $0.20 \lesssim k[h \text{Mpc}^{-1}] \lesssim 0.80$  with an amplitude that on average can be as large as  $\sim 40$  per cent. This is a direct consequence of the suppression of the matter power spectrum at large/intermediate  $k$  for lower mass resolution simulations, as described in §4.4. Nonetheless, the artificial suppression of power is mitigated at low redshifts and/or higher  $k$  when the local density of particles in the simulations triggers the AMR grid refinement, which explains why this systematic effect shown in Fig. 6.1 fades away across the whole interval at  $z \leq 0.5$ .

Ref. [134] corrected the BAO spectrum for the mass resolution effect by combining the cosmic variance limited power spectrum from DEUS-FUR with that of smaller volume and higher resolution simulations. In fact, since the mass resolution effect on the matter power spectrum is a smooth function of  $k$ , it can be corrected by taking the ratio  $r$  between the spectrum  $\hat{P}$  and a higher resolution one and fitting it with a polynomial function. The corrected spectrum is then  $\hat{P}^{\text{corr}} = r \hat{P}$ . Here, we opt for a similar strategy. Since the covariance is obtained by sampling the matter power spectrum of independent realisations, we can correct the lower resolution power spectra of Set A by implementing statistical information on the power spectra obtained from the higher resolution simulations of Set B. We assume that the corrected power spectrum estimator,  $\hat{P}_A^{\text{corr}}$ , and that of the lower resolution simulations,  $\hat{P}_A$ , are related by a simple linear transformation:

$$\hat{P}_A^{\text{corr}} = a \hat{P}_A + b. \quad (6.5)$$

The goal here is to find a correction that maps each of the  $\hat{P}_A$  from the pdf of Set A,  $f(\hat{P}_A)$ , into the one of Set B,  $f(\hat{P}_B)$ . Since the proposed correction has two parameters, we only need the first two moments of  $f(\hat{P}_B)$  to correct the spectra of Set A. In principle one can assume higher-order corrections,

$z$	$\alpha$	$\beta$	$\gamma$	$\delta$
0	-0.156	0.569	-0.442	0.146
0.3	0.098	-0.039	-0.290	0.188
0.5	-0.410	0.695	-0.895	0.343
1	0.266	1.026	0.280	0.252
2	2.240	-5.272	2.924	-0.051

**Table 6.3:** Best-fitting values for the parameters  $\alpha, \beta, \gamma$  and  $\delta$  of Eq.(6.9) at different redshifts.

but then higher moments of  $f(\hat{P}_B)$  are needed for the computation, and the statistics of our sample is not sufficient to resolve them.

We determine the coefficients  $a$  and  $b$  by imposing that the average  $\bar{P}_A^{\text{corr}} = \bar{P}_B$  and the variance  $\sigma_{\hat{P}_A^{\text{corr}}}^2 = \sigma_{\hat{P}_B}^2$ . Those conditions translate in the system:

$$\bar{P}_B = a \bar{P}_A + b, \quad (6.6)$$

$$\sigma_{\hat{P}_B}^2 = a^2 \sigma_{\hat{P}_A}^2, \quad (6.7)$$

from which we finally obtain

$$\hat{P}_A^{\text{corr}}(k) = \left[ \hat{P}_A(k) - \bar{P}_A(k) \right] \frac{\sigma_{\hat{P}_B}(k)}{\sigma_{\hat{P}_A}(k)} + \bar{P}_B(k), \quad (6.8)$$

The standard deviation of the power spectra from Set B is very noisy, and so is the ratio  $\sigma_{\hat{P}_B}/\sigma_{\hat{P}_A}$ . We find convenient to smooth out this noise and assume a fourth degree polynomial fitting function of  $k$ , such that

$$\sigma_{\hat{P}_B}/\sigma_{\hat{P}_A} \equiv \alpha k^4 + \beta k^3 + \gamma k^2 + \delta k + 1 \quad (6.9)$$

where  $\alpha, \beta, \gamma, \delta$  are the fitting parameters that we obtain by fitting the polynomial function to the numerical ratio of the standard deviations. We impose that on the large linear scales, e.g. at  $k_{\text{min}}$  this ratio tends to unity since in this regime there is no difference between Set A and B. In Fig. 6.2 we plot  $\sigma_{\hat{P}_B}/\sigma_{\hat{P}_A}$  and the best-fitting smoothing function at  $z = 0, 0.3, 0.5, 1$  and  $2$  respectively. The best-fitting values of the parameters are quoted in Table 6.3.

In Fig. 6.3 we plot the average matter power spectrum and the standard deviation at several redshifts in the interval  $0 \leq z \leq 2$  corrected for the mass resolution effect. The standard deviation is largest near  $k_{\text{min}}$  due to finite volume effects and reduces to less than 10% for  $k \gtrsim 0.03 h \text{ Mpc}^{-1}$ . We may

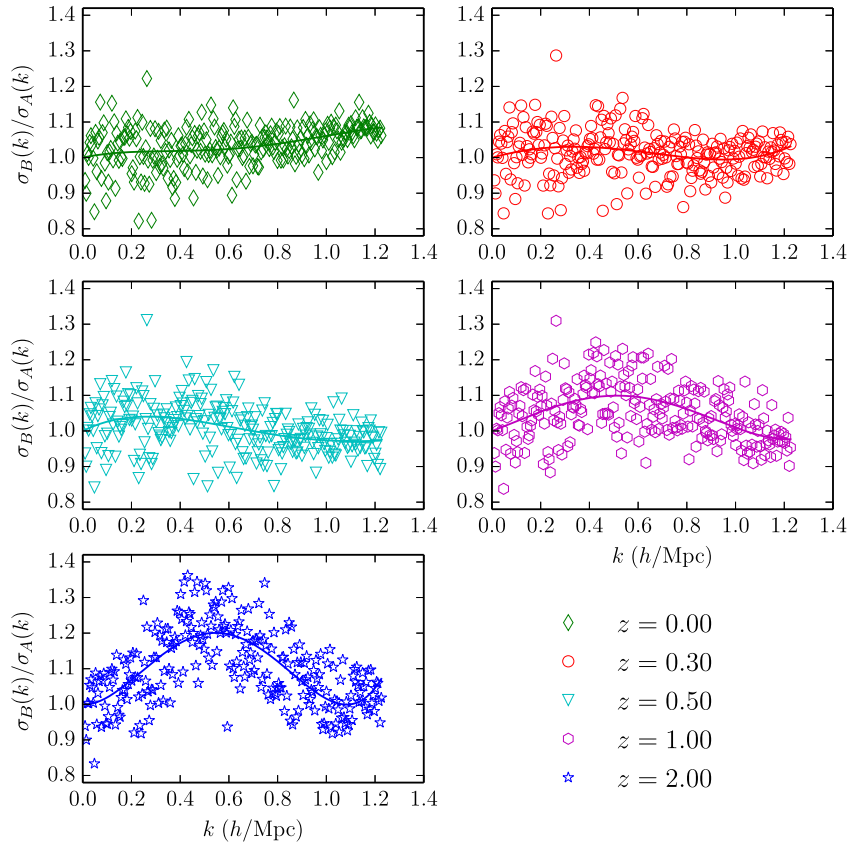


**Figure 6.2:** Ratio of the standard deviation of the spectra from Set B and A,  $\sigma_{\hat{P}_B}/\sigma_{\hat{P}_A}$  as a function of  $k$  at  $z = 0, 0.3, 0.5, 1$  and  $2$  respectively. The solid lines are the best-fitting smoothing functions.

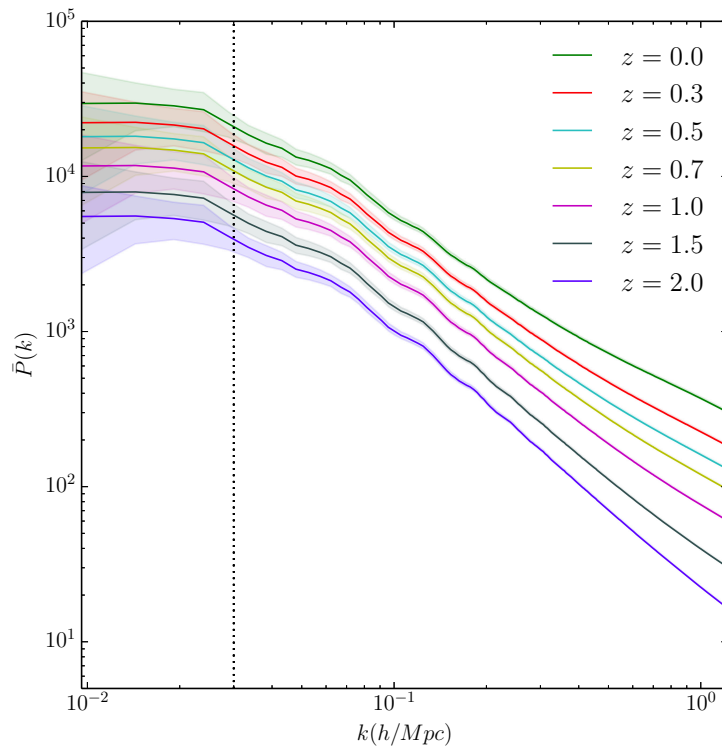


**Figure 6.3:** Average and standard deviation of the non-linear matter power spectrum at  $0 \leq z \leq 2$  (bottom to top) of Set A corrected for mass resolution effects.

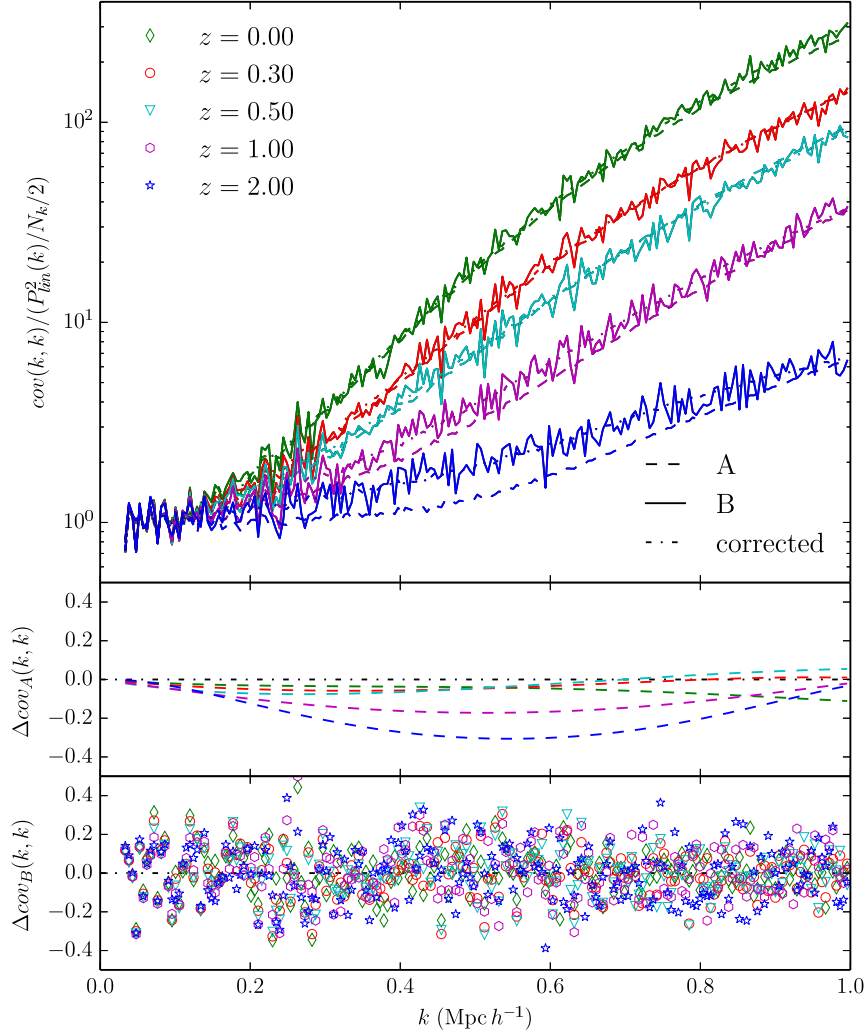


**Figure 6.4:** Top panel: as in Fig. 6.1 including the diagonal components of the covariance matrix from the corrected spectra of Set A (dot-dashed line). Middle panel: relative difference of the uncorrected variance of Set A (central) with respect to the corrected one. Corrections can be as large as 40 per cent at  $z = 2$ , 20 per cent at  $z = 1$  and less than 10 per cent at lower redshifts. Bottom panel: relative difference of the variance from the higher resolution simulations Set B with respect to the correct variance. The residuals show no systematic shift indicating that the correction efficiently accounts for the mass resolution effect.

notice that contrary to linear theory expectations the average power spectrum at different redshifts is nearly flat in the range  $0.01 < k [h \text{ Mpc}^{-1}] < 0.03$ , showing the typical power suppression due to finite volume effects [82]. Thus, to be conservative from now on we set  $k_{\text{min}} = 0.03 h \text{ Mpc}^{-1}$  unless otherwise specified.

In Fig. 6.4 we show the diagonal elements of the covariance matrix normalised to the Gaussian term for Set A before (dashed lines) and after (dashed dotted lines) correction, and for set B (solid lines) at  $z = 0.0, 0.3, 0.5, 1.0$  and  $2.0$  (top to bottom) respectively. As we can see the corrected curves fit well through those obtained from the higher resolution simulations. In the middle panel of Fig. 6.4 we show the relative differences between the corrected and uncorrected curves at different redshifts (dashed lines top to bottom corresponds to  $z = 0$  to  $2$ ). We can clearly see that the amplitude of the correction at high redshift in the interval  $0.20 \lesssim k [h \text{ Mpc}^{-1}] \lesssim 0.80$  can be as large as 40 per cent, while at  $z < 0.5$  the difference remains below the 10 per cent level. In the bottom panel of Fig. 6.4 we also plot the residuals between the corrected covariance of Set A and that from Set B (different dot types correspond to different redshifts as shown in the legend). As we can see there is no systematic shift and the only differences are due to the statistical noise of Set B.

The mass resolution error also underestimates the off-diagonal components of the covariance matrix, nonetheless the amplitude results to be smaller than the systematic shift we have seen on the diagonal elements. As expected we find the correction of the low resolution power spectra to also account for the mass resolution effect on the off-diagonal components.

## 6.4 Fourier Mode Correlations

In order to quantify the correlation between pairs of Fourier modes it is useful to introduce the correlation coefficient

$$r(k_1, k_2) = \frac{\text{cov}(k_1, k_2)}{\sqrt{\text{cov}(k_1, k_1) \text{cov}(k_2, k_2)}}, \quad (6.10)$$

which varies between 1 (maximum correlation) and  $-1$  (maximum anti-correlation), and is 0 when modes are uncorrelated. In linear regime the correlation coefficient is the identity matrix.

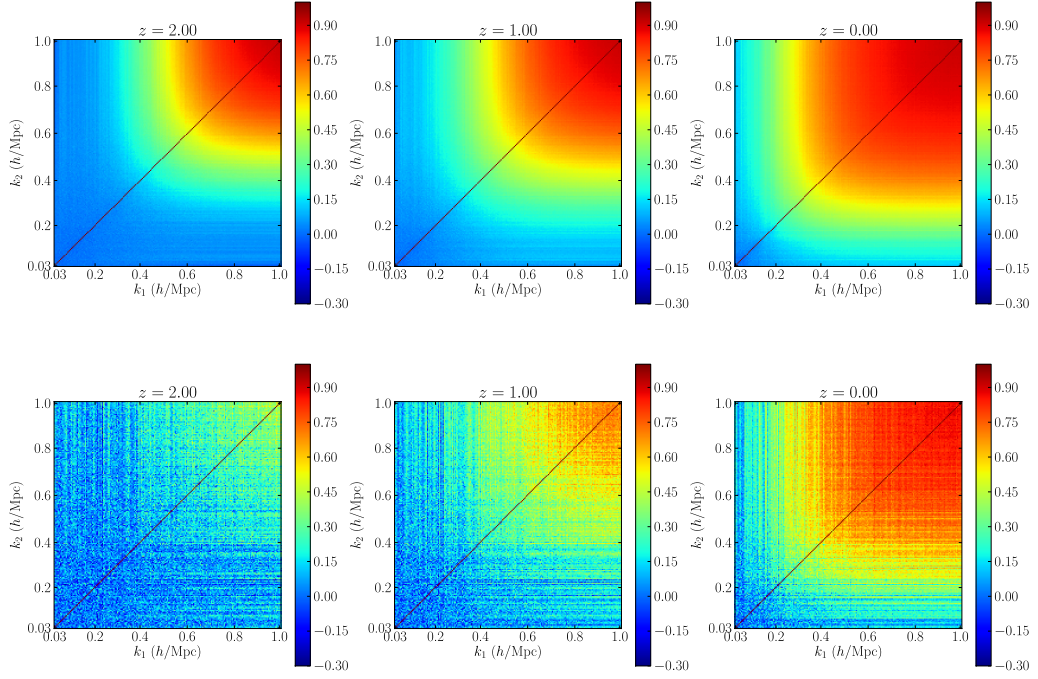


**Figure 6.5:** Correlation coefficient matrix at  $z = 2$  (left panels), 1 (central panels) and 0 (right panels) respectively estimated from Set A (top panels) and Set B (bottom panels). We can see the increasing amplitude of pair correlation at high  $k$  shifting towards lower wave-numbers for decreasing redshift. The comparison between the two sets shows that the structure of the correlations is poorly reproduced when using a low number of simulations.

In Fig. 6.5 we plot  $r(k_1, k_2)$  in the interval  $0.03 < k[h \text{ Mpc}^{-1}] < 1.00$  (which includes the BAO range) at  $z = 2$  (left panels), 1 (central panels) and 0 (right panels) for Set A (top panels) and for Set B (bottom panels). We do not show the correlation coefficient inferred from the corrected spectra of Set A since this coincides with the uncorrected one to very good approximation. This is because the mass resolution effect discussed in the previous section scales approximately linearly with the power spectrum affecting the covariance matrix amplitude. Since the correlation coefficient is given by the covariance matrix normalised by the root-square of the product of its diagonal elements the effect cancels out in the ratio.

Non-vanishing off-diagonal elements are already present at  $z = 2$  at large  $k$  values, for instance the mode  $k_1 \sim 0.3 h \text{ Mpc}^{-1}$  has a 10 per cent correlation with  $k_2 \sim 0.4 h \text{ Mpc}^{-1}$  and 20 per cent with  $k_2 \sim 1 h \text{ Mpc}^{-1}$ . The amplitude of the correlations increases as a function of  $k$  and extends towards smaller  $k$  values at lower redshifts as the dynamics of the modes increasingly deviates from the linear regime of collapse. The comparison between the two sets shows the importance of having a large set of simulations, in order to reduce the impact of noise. In fact, the structure of correlations is much clearer for Set A than for Set B, for which at  $z = 2$  the signal is hard to distinguish from the statistical noise. It is worth noticing that in the BAO range ( $0.01 < k[h \text{ Mpc}^{-1}] < 0.30$ ) the correlation in the off-diagonal components can reach a level up to 30-35 per cent between redshift 1 and 0, which confirms the need of an accurate estimation of the 3D power spectrum covariance matrix for BAO data analyses.

## 6.5 Probability Distribution of the Power Spectrum Estimator

We now focus on the probability distribution function (PDF) of the matter power spectrum estimator. For Gaussian initial conditions, during the linear regime of gravitational collapse the matter power spectrum at a given wave-number  $k$  is distributed as a  $\chi^2$  with  $N_k$  degrees-of-freedom [see e.g. 68]. In the large  $N_k$  limit, which corresponds to sufficiently large volumes and high wave-numbers, the PDF tends to a Gaussian. However, at high  $k$  the non-linear evolution of matter clustering is expected to introduce non-Gaussianities (i.e. departures from a  $\chi^2$ -distribution in the large  $N_k$  limit).

The large sample of simulations from DEUS-PUR allows us to finely sam-

ple such a distribution and test for non-Gaussianities. To this end it is convenient to rescale the power spectrum estimator as  $\sqrt{N_k/2}(\hat{P}/\bar{P} - 1)$ , such that in the large  $N_k$  limit and in linear regime the distribution is a Gaussian with zero mean and unity variance. In Fig. 6.6 we plot the estimated PDF from Set A at  $z = 0$  and  $k = 0.05, 0.20, 0.40, 0.60$  and  $1.00 h \text{ Mpc}^{-1}$  respectively. Poisson errors are shown as error bars on the points, but are usually much smaller than the size of the points.

We quantify the deviations from Gaussianity in terms of the skewness and kurtosis defined as:

$$S_3(k) = \frac{N_s^{-1} \sum_{i=1}^{N_s} [\hat{P}_i(k) - \bar{P}(k)]^3}{\left\{ (N_s - 1)^{-1} \sum_{i=1}^{N_s} [\hat{P}_i(k) - \bar{P}(k)]^2 \right\}^{3/2}}, \quad (6.11)$$

$$S_4(k) = \frac{N_s^{-1} \sum_{i=1}^{N_s} [\hat{P}_i(k) - \bar{P}(k)]^4}{\left\{ (N_s - 1)^{-1} \sum_{i=1}^{N_s} [\hat{P}_i(k) - \bar{P}(k)]^2 \right\}^2} - 3. \quad (6.12)$$

For a  $\chi^2$ -distribution with  $N_k$  degrees of freedom, these can be computed exactly, resulting in  $S_3(k) = \sqrt{8/N_k}$  and  $S_4(k) = 12/N_k$  [see e.g. 163].

In Fig. 6.7 we plot  $S_3(k)$  (left panels) and  $S_4(k)$  (right panels) from Set A estimated at  $z = 105$  and  $z = 0, 0.3, 0.5$  (where mass resolution effects are subdominant) respectively. For visual purposes we have binned the estimated values in bins of size  $\Delta k/k = 0.1$  and included statistical errors on the data points. The dashed lines correspond to the  $\chi^2$  expected values of  $S_3(k)$  and  $S_4(k)$ . We notice that at  $z = 105$  the skewness is consistent with that from the  $\chi^2$ -distribution, while for  $z < 0.5$  and  $k \gtrsim 0.25 h \text{ Mpc}^{-1}$  we can clearly see increasing deviations as a function of  $k$  at high statistical significance. In contrast the kurtosis remains consistent with  $\chi^2$  expected values and any departure of  $S_4(k)$  from the Gaussian random field prediction still remains within statistical errors.

In Fig. 6.8 we show the skewness normalised to the  $\chi^2$  expectation, where we can see that non-linear effects induce a skewness up to 8 times larger than the prediction at low redshift. These deviations can be understood as a signal of the correlation between the modes. In fact, band powers are measured from correlated modes, so that the central limit theorem does not apply and the effective number of degrees of freedom in the bin is reduced. We can have an estimate of the number of independent modes as [111]:

$$N_{dof} = \frac{2P_{lin}^2(k)}{cov(k, k)}. \quad (6.13)$$

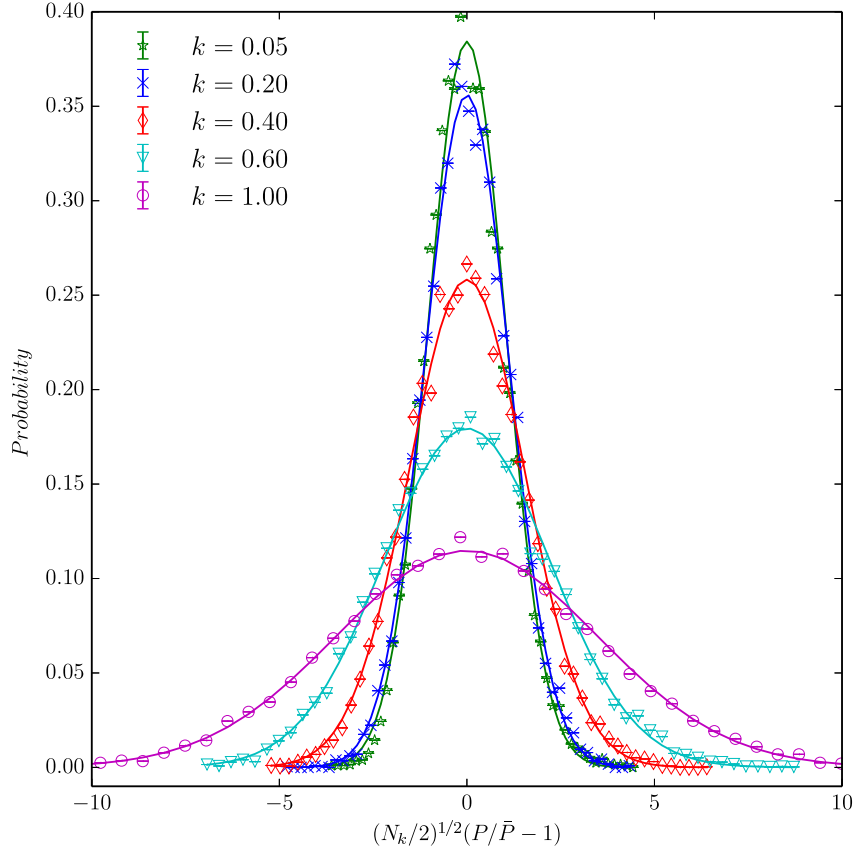


**Figure 6.6:** Probability distribution of the rescaled power spectrum estimator  $\sqrt{N_k/2}(\hat{P}/\bar{P} - 1)$  estimated from the 12288 realisations of Set A for  $k = 0.05$  (green star) 0.20 (blue cross) 0.40 (red diamond), 0.60 (light-blue triangle) and  $1.00 h \text{Mpc}^{-1}$  (magenta circle) respectively. The error bars are given by Poisson errors. The solid line curves show the Gaussian distribution with sample mean and variance of the same set at the corresponding values of  $k$ .

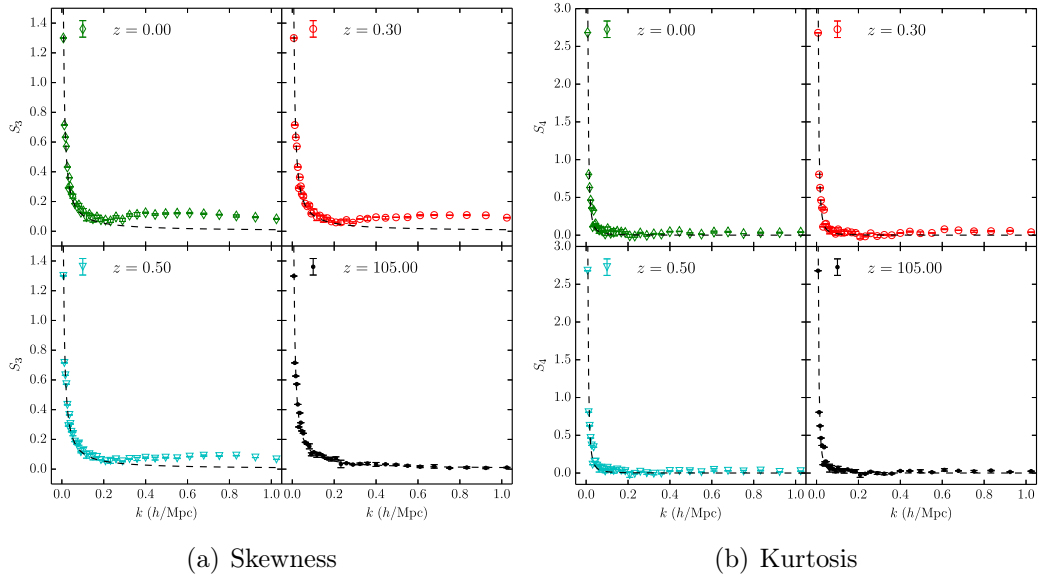


**Figure 6.7:** Higher moments of the probability distribution of  $\hat{P}$  as a function of  $k$  for  $z = 0, 0.3, 0.5$  and  $105$  respectively. The measured values are binned in intervals of size  $\Delta k/k \sim 0.1$ , the associated Poisson errors are smaller than the data points. The dashed lines represent the  $\chi^2$ -distribution predictions.

This is shown in Fig. 6.9 at  $z = 0, 0.3, 0.5$ , where the dashed black line indicates the number of modes obtained by counting modes in the bin  $N_k$ . We can observe that the difference between the predicted and effective  $N_{dof}$  is amplified going toward lower redshifts, as the correlations due to the non-linear evolution increase. This trend is consistent with the increase of skewness at high  $k$  and low redshifts.

Previous studies have determined the power spectrum distribution using smaller simulation ensembles and at low redshifts found no statistically significant deviation of the skewness from expectations of a Gaussian random density field [see e.g. 163]. We show in Fig. 6.10 a comparison of our measured skewness with the one of Ref. [163], that used 5000 simulations, where the error-bars are given by the square-root of the skewness sample variance  $\sim \sqrt{6/N_s}$ . This stresses the necessity of using very large samples of simulations to distinguish the skewness signal from sampling errors.

We believe that such a result can have important observational implications which warrant further investigation. At large  $k$  and  $z < 0.5$  the ratio  $S_3(k)/\sqrt{8/N_k} \gtrsim 2$ , hence unbiased measurements of the band power

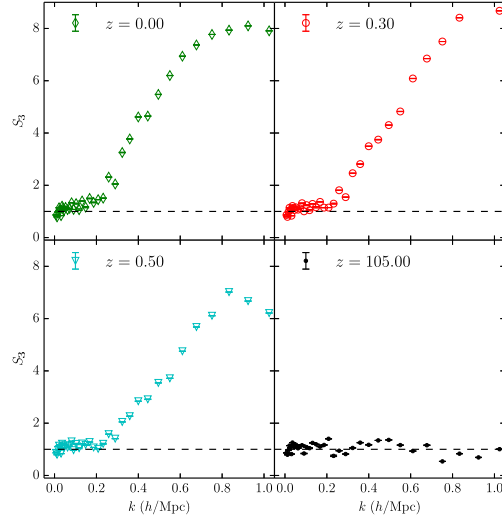


**Figure 6.8:** Skewness of the probability distribution of  $\hat{P}$  as a function of  $k$  for  $z = 0, 0.3, 0.5$  and  $105$  respectively, normalised to the  $\chi^2$ -distribution predictions.

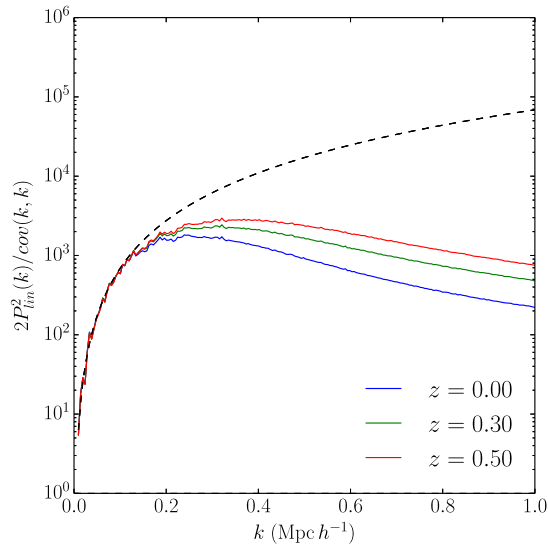


**Figure 6.9:** Effective number of degrees of freedom in the  $k$  bins for  $z = 0$  (blue),  $0.3$  (green),  $0.5$  (red). The dashed black curve represents  $N_k$ , the number of modes obtained by counting modes in the bin.

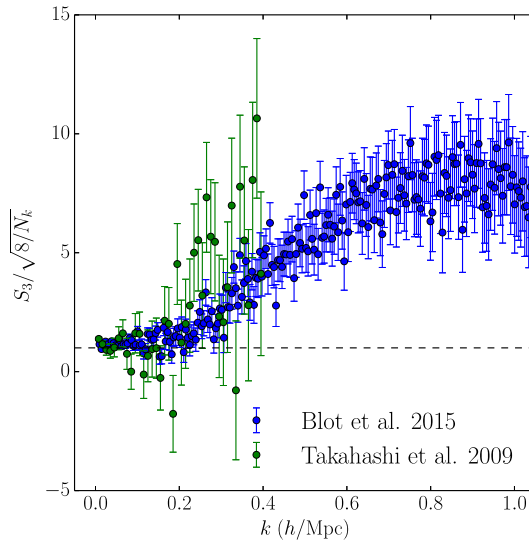


**Figure 6.10:** Skewness of the probability distribution of  $\hat{P}$  as a function of  $k$  at  $z = 0$ , normalised to the  $\chi^2$ -distribution predictions, for the DEUS PUR sample (blue) and the sample of Ref. [163] (green). Error-bars are given by the square root of the skewness sample variance  $\sim \sqrt{6/N_s}$  normalised to  $\sqrt{8/N_k}$ .

from observables of the clustering of matter such as weak lensing observations [see also 142] may require prior knowledge of the  $\hat{P}(k)$  distribution. At lower  $k$  the departure from a  $\chi^2$ -distribution is at most a factor 2 for  $k \lesssim 0.30 h \text{ Mpc}^{-1}$ . Thus, measurements of the BAO may still be performed using only covariance matrix information, though aiming at sub-percent accuracy may require a more detailed study to elucidate the full impact of the non-Gaussian distribution of  $\hat{P}(k)$ .



# Chapter 7

## Non-linear covariance matrix errors and cosmological parameter uncertainties for Euclid-like surveys

In this Chapter we focus on the sample covariance matrix estimator and study how the errors on this estimate propagate in the data analysis. We start by studying the effect of mass resolution and sampling errors on the power spectrum signal-to-noise in §7.1. For Gaussian distributed data it is possible to compute analytically the error on the sample estimators of the covariance matrix and its inverse, the precision matrix, which are respectively Wishart and inverse Wishart distributed. We test these predictions against the sample covariance and precision matrices measured in the DEUS-PUR Set A (see Table 6.2) in §7.2. Finally, to assess the impact of such errors on the cosmological parameter uncertainties from future surveys such as Euclid we perform a Fisher analysis forecast in §7.3.

### 7.1 Signal-to-Noise

The signal-to-noise of the matter power spectrum is defined as:

$$\left(\frac{S}{N}\right)^2 = \sum_{k_1, k_2 < k_{\max}} P(k_1) \mathcal{P}(k_1, k_2) P(k_2), \quad (7.1)$$

where  $\mathcal{P} = \mathcal{C}^{-1}$  is the inverse of covariance matrix, also known as precision matrix. Since we estimate the covariance from a finite ensemble of

independent realisations, there is a statistical error associated to the sample covariance. Thus, inverting the sample covariance gives a biased estimate of the precision matrix. For Gaussian distributed data the unbiased estimator of the precision matrix is given by (see §7.2):

$$\hat{\mathcal{P}} = \frac{N_s - N_b - 2}{N_s - 1} \hat{\mathcal{C}}^{-1}, \quad (7.2)$$

where  $\hat{\mathcal{C}}$  is the covariance estimator defined in Eq. (6.4),  $N_s$  is the number of realisations and  $N_b$  is the number of band power bins. This estimator is defined only for  $N_s > N_b + 2$ . In any case, for  $N_s < N_b + 1$  the values of the sample covariance are not positive definite and its inverse is not defined [81]. As we will show in the next section, this bias correction is accurate even if the power spectrum has a non-Gaussian distribution. In evaluating the signal-to-noise we set the power spectrum in Eq. (7.1) to the average of the corrected spectra from Set A and compute the signal-to-noise using the precision matrix defined by Eq. (7.2) for the corrected and uncorrected spectra of Set A respectively.

In Fig. 7.1 we plot the resulting signal-to-noise estimates at  $z = 0, 0.3, 0.5, 1$  and  $2$  respectively as a function of  $k_{\max}$ . We can see that the effect of mass resolution errors is to artificially enhance the signal-to-noise. As discussed in Section 6.3 this is because lower mass resolution simulations underestimate the covariance matrix. This results into a greater amplitude of the precision matrix components and consequently in a larger signal-to-noise compared to higher mass resolution estimates. As we can see in Fig. 7.1 the signal-to-noise from the corrected Set A is up to  $\sim 15$  per cent smaller at  $k_{\max} \gtrsim 0.30 h \text{ Mpc}^{-1}$ , while at lower redshift (where the mass resolution effect is negligible) the S/N from the corrected and uncorrected Set A agree within a few per cent. Assuming that the precision matrix from Set A is drawn from the inverse-Wishart distribution [131] we expect the statistical errors on S/N to be  $\sim 1$  per cent (see §7.2.3), much smaller than the effect of mass resolution at  $z > 1$ . For comparison, we also plot the expected S/N in the Gaussian case. As already noted by Ref. [11], the signal-to-noise saturates above a redshift dependent scale [see also 154, 163]. The signal-to-noise can in fact be interpreted as an information measure, so that the saturation reflects the fact that at non-linear scales the correlations reduce the independent information in the power spectrum, which leaks to higher-order correlation functions.

To have an idea of the effect of sampling error on the signal to noise we plot in Fig. 7.2 the signal-to-noise at  $k_{\max} = 0.40 h \text{ Mpc}^{-1}$  (a scale on the plateau of the S/N) as a function of the number of realisations at different

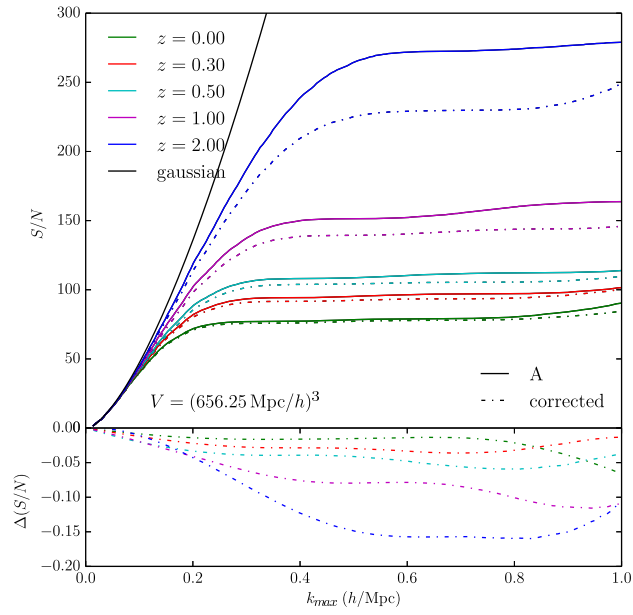


**Figure 7.1:** Top panel: signal-to-noise of power spectrum measurements as a function of  $k_{\text{max}}$  estimated from Set A with (solid line) and without (dash line) mass resolution correction for  $z = 0, 0.3, 0.5, 1$  and  $2$  respectively. The solid black line corresponds to the Gaussian prediction. Bottom panel: relative difference of  $S/N$  with and without mass resolution correction.

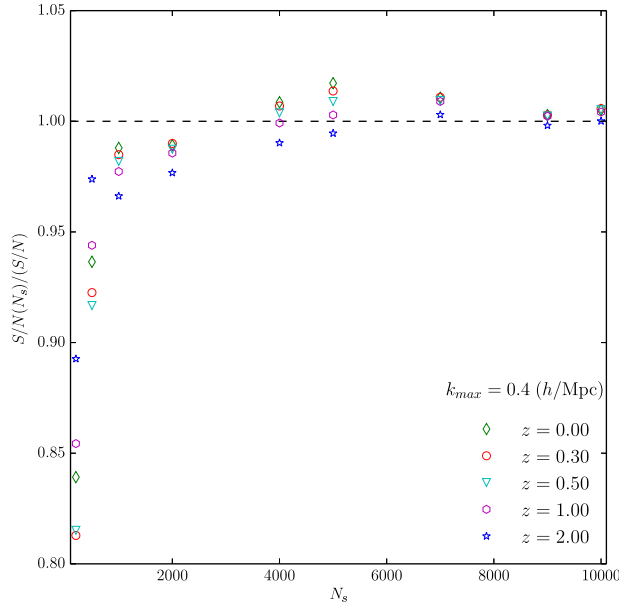


**Figure 7.2:** Signal-to-noise of power spectrum measurements at  $k_{\max} = 0.40 h \text{ Mpc}^{-1}$  estimated from sub-samples of Set A with mass resolution correction and normalised to the signal-to-noise of the full Set A for  $z = 0, 0.3, 0.5, 1$  and  $2$ . Convergence at the per cent level is achieved for  $N_s > 4000$ .

redshifts. As we can see the signal-to-noise converges for  $N_s > 4000$  at all the redshifts within a few per cent.

## 7.2 Covariance and Precision Matrix Errors

Let us consider a set of data consisting of measurements of the matter power spectrum,  $P_{k_i}^d$  collected in  $i = 1, \dots, N_d$  bands. A standard likelihood analysis will use these measurements to infer constraints on a set of parameters  $\vec{\theta}$  given a model prediction of the power spectrum  $P_{k_i}^t(\vec{\theta})$ . In the case of Gaussian distributed data the likelihood reads as

$$\mathcal{L} \propto \exp \left\{ -\frac{1}{2} \sum_{i,j=1}^{N_d} \left[ P_{k_i}^d - P_{k_i}^t(\vec{\theta}) \right] \mathcal{C}_{ij}^{-1} \left[ P_{k_j}^d - P_{k_j}^t(\vec{\theta}) \right] \right\}, \quad (7.3)$$

where  $\mathcal{C}_{ij}^{-1}$  is the inverse of the covariance matrix, also dubbed as precision matrix. Notice that in writing Eq. (7.3) we have assumed that the covariance is independent of the parameters  $\vec{\theta}$ , in such a case we can neglect the

normalisation factor which does not play any role in the determination of the parameter constraints. Nevertheless, it is worth remarking that the power spectrum covariance matrix may indeed vary with the cosmological parameters [see e.g. 97, who have studied the impact of a cosmological model dependent covariance obtained from simulations of a lognormal galaxy field]. However, the extent to which the cosmological parameter inference is affected by cosmological model dependencies of the covariance due to non-linearities is still not known and will require a dedicated study which is beyond the scope of this work.

The point that we want to address here is how non-linearities of the density field impact the estimation of the covariance and precision matrix errors. These errors arise from the fact that the true covariance  $\mathcal{C}$  is unknown, we only have an unbiased estimate of it as given by Eq. (6.4). This has twofold consequences: first the inverse of the sample covariance,  $\hat{\mathcal{P}} \equiv \hat{\mathcal{C}}^{-1}$ , is not an unbiased estimator of the precision matrix due to the noise in the sample covariance [10]; second, the noise in the sample covariance propagates in the cosmological parameter inference.

### 7.2.1 Precision Matrix Bias

Let us first consider the problem of the bias of the precision matrix estimator. This can be built by inverting the sample covariance estimator such that  $\hat{\mathcal{P}} \equiv \hat{\mathcal{C}}^{-1}$  provided that  $N_s > N_d + 1$  otherwise the sample covariance is not positive definite and the inverse is undefined. For Gaussian distributed data the expectation value of the inverse of the sampled covariance matrix, assuming that the mean of the precision matrix distribution is unknown, is given by [see e.g. 131, 10, 166]

$$\langle \hat{\mathcal{P}}_{ij} \rangle = \frac{N_s - 1}{N_s - N_d - 2} \mathcal{C}_{ij}^{-1}, \quad (7.4)$$

provided that  $N_s > N_d + 2$ , where  $N_s$  is the number of simulations used to estimate the sample covariance. It follows that an unbiased estimate of the precision matrix is given by [81]:

$$\mathcal{P}_{ij}^{\text{unbiased}} = \frac{N_s - N_d - 2}{N_s - 1} \hat{\mathcal{C}}_{ij}^{-1}, \quad (7.5)$$

which is the only unbiased estimator of the precision matrix [166]. We can test the validity of Eq. (7.4) using the ensemble of  $N_t = 12288$  spectra from the DEUS-PUR Set A corrected for mass resolution errors and sampled over

$N_d = 250$  bands in the range  $0.03 \lesssim k [h \text{ Mpc}^{-1}] \lesssim 1.22$ .

To compute the average of the sample precision matrix which appears in the left-hand-side of Eq. (7.4) as a function of the number of simulation  $N_s$  we divide the ensemble of spectra in  $N_g = \text{int}(N_t/N_s)$  groups, in each group we estimate the sample covariance using Eq. (6.4) and computing the inverse we obtain the biased estimate of precision matrix. Then, we compute the average biased precision matrix over the  $N_g$  groups as  $\langle \hat{\mathcal{P}} \rangle = 1/N_g \sum_k \hat{\mathcal{P}}_k$  which we compare to that obtained using the entire ensemble of  $N_t$  spectra,  $\mathcal{C}^{-1}$ , on the right-hand-side of Eq. (7.4). To compare the numerical results against the theoretical prediction we follow Ref. [166] and compute the fractional bias defined as:

$$B_{\mathcal{P}} \equiv \frac{\text{Tr} \langle \hat{\mathcal{P}} \rangle}{\text{Tr} \mathcal{C}^{-1}} = \frac{N_s - 1}{N_s - N_d - 2}, \quad (7.6)$$

which we plot in Fig. 7.3 as a function of  $N_s$  from the ensemble of spectra at  $z = 0$ . In the upper panel the solid black line is the scaling expected for Gaussian distributed data, while the blue points are the numerical results, the relative difference is shown in the lower panel. We can see that for  $N_s > 500$  the analytical prediction agrees to the N-body simulation results to better than 0.5%.

## 7.2.2 Variance of Sample Covariance

Let us now consider the errors on the sample covariance. For Gaussian distributed data the statistics of the sample covariance is described by the Wishart distribution [185, 131]. Ref. [166] have derived an analytical expression for the variance which reads as

$$\sigma^2(\hat{\mathcal{C}}_{ij}) = \frac{1}{N_s - 1} (\langle \mathcal{C}_{ij} \rangle^2 + \langle \mathcal{C}_{ii} \rangle \langle \mathcal{C}_{jj} \rangle). \quad (7.7)$$

As for the estimation of the fractional bias we estimate the average and standard deviation of the covariance over  $N_g = \text{int}(N_t/N_s)$  groups of simulations as a function of  $N_s$ . We can test the validity of Eq. (7.7) along the diagonal elements by computing the ratio:

$$\epsilon_{\mathcal{C}} = \sqrt{\frac{\sum_i \sigma^2(\hat{\mathcal{C}}_{ii})}{\sum_i \langle \mathcal{C}_{ii} \rangle^2}} = \sqrt{\frac{2}{N_s - 1}}, \quad (7.8)$$

which we plot in Fig. 7.4 as a function of  $N_s$  having taken the sum over the diagonal elements for three different  $k$ -intervals. We can see that deviations from the expected scaling in Eq. (7.8) are largest ( $> 10\%$ ) for

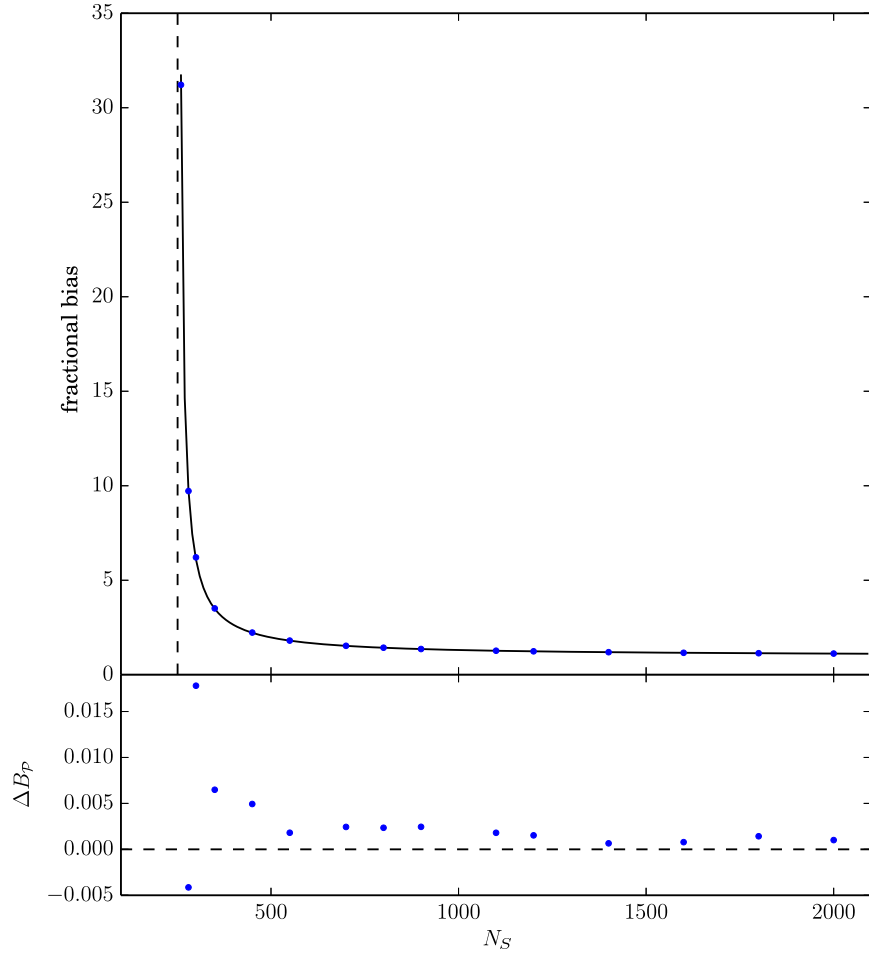


**Figure 7.3:** Fractional bias of the trace of the mean of the sample precision matrix at  $z = 0$  as a function of the number of simulations,  $N_s$ . The solid black line is the predicted scaling for Gaussian distributed data, Eq. (7.6), while the dots are the estimates from the N-body simulations. The vertical dashed line indicates the minimum number of simulations for which the sample covariance is positive definite. In the bottom panel is shown the relative difference.

$0.03 < k [h \text{ Mpc}^{-1}] < 0.11$  and decrease for increasing values of  $k_{\text{min}}$ . These deviations are due to finite volume effects which, as shown in Fig. 6.3, manifest in a larger standard deviation of the estimated power spectra at low  $k$ . For  $k > 0.11 h \text{ Mpc}^{-1}$  this sample variance effect is  $< 5\%$  on the matter power spectrum and correlates with the reduced discrepancy from the scaling of Eq. (7.8). Nonetheless, we may still notice deviations up to  $\sim 10\%$  in the higher  $k$ -intervals. This can be seen more clearly in Fig. 7.5 where we consider intervals at larger wave-numbers. In particular, we may notice increasing departures from Eq. (7.8) above  $\sim 10\%$  level for  $N_s > 1500$ . We interpret this systematic trend as an indication of deviations from the Wishart distribution due to the non-linearities of the matter density field which cause non-Gaussian errors. The same trend can be seen in the off-diagonal components of the variance of the sample covariance. To this purpose we compute the ratio of the sum of the left and right-hand side of Eq. (7.7) over off-diagonal elements for which the corresponding elements of the matter power spectrum correlation matrix are below and above the 50% level. We plot the results in Fig. 7.6. In the case of off-diagonal elements with correlation  $< 0.5$  we can see that the ratio is of order unity, while for off-diagonal elements characterised by larger correlations ( $> 0.5$ ) the ratio deviates from unity by more than 10% for  $N_s > 1500$ . This clearly shows that the non-Gaussian errors due to the non-linearities of the late time clustering of the matter density field cause deviations of the sample covariance errors from expectations of the Wishart distribution. It is worth noticing that even with our large ensemble of simulations, from the numerical analysis we are unable to assess whether these deviations saturate for very large  $N_s$  values, suggesting a significant departure from the Wishart distribution.

### 7.2.3 Variance of Sample Precision Matrix

The estimator of the precision matrix is distributed as the inverse-Wishart distribution [185, 131] and an analytical expression for the unbiased variance of the precision matrix has been derived in Ref. [166]:

$$\sigma^2(\widehat{\mathcal{P}}_{ij}) = A [(N_s - N_d)\langle \mathcal{P}_{ij} \rangle^2 + (N_s - N_d - 2)\langle \mathcal{P}_{ii} \rangle \langle \mathcal{P}_{jj} \rangle], \quad (7.9)$$

where  $A = (N_s - N_d - 1)^{-1}(N_s - N_d - 4)^{-1}$ . As in the case of the covariance errors we test this relation along the diagonal components and compute the ratio

$$\epsilon_{\mathcal{P}} = \sqrt{\frac{\sum_i \sigma^2(\widehat{\mathcal{P}}_{ii})}{\sum_i \langle \mathcal{P}_{ii} \rangle^2}} = \sqrt{\frac{2}{N_s - N_d - 4}}, \quad (7.10)$$

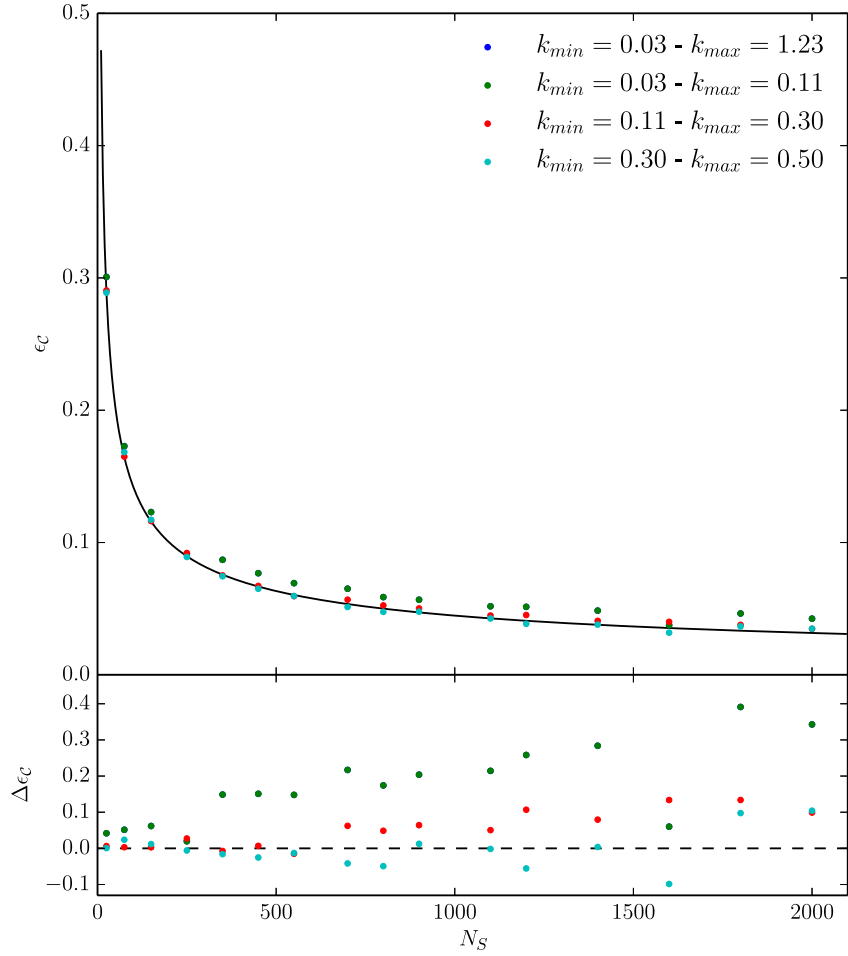


**Figure 7.4:**  $\epsilon_C$  as a function of  $N_s$  in different wavenumber intervals with increasing values of  $k_{\min} = 0.03$  (green dots),  $0.11$  (red dots) and  $0.30 h \text{ Mpc}^{-1}$  (light blue dots). Black solid line is the expected scaling from the Wishart distribution. In the bottom panel is shown the relative difference with respect to the expected scaling of Gaussian distributed data.

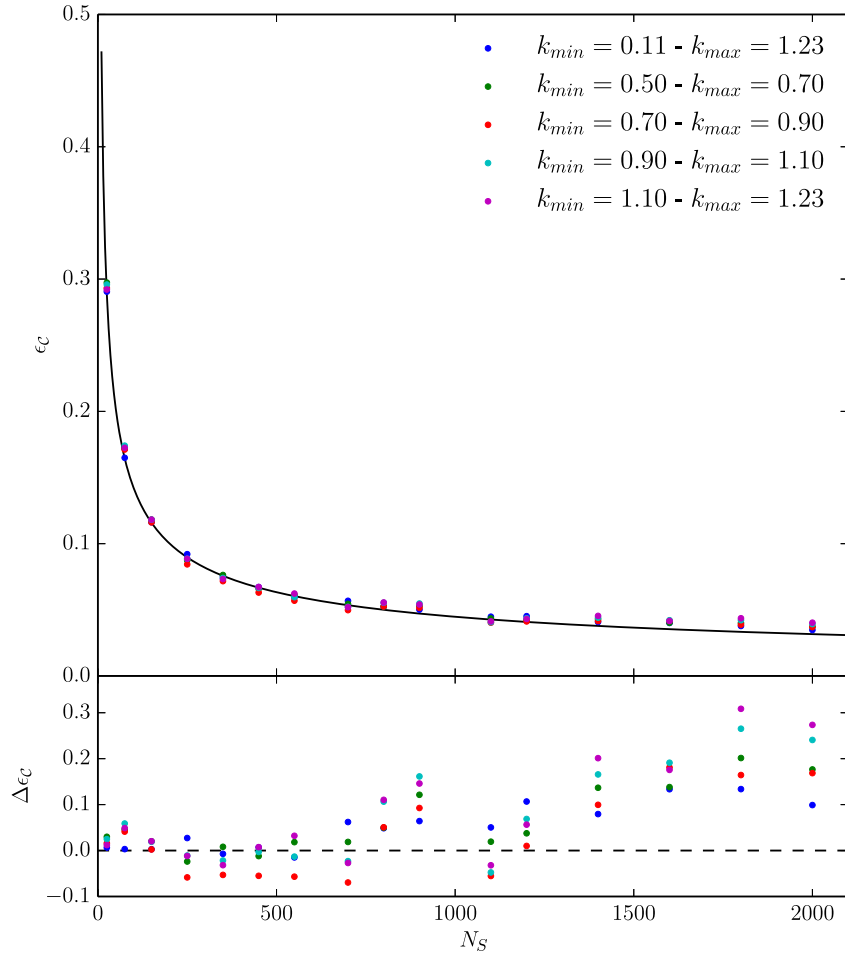


**Figure 7.5:** As in Fig. 7.4 for larger  $k$ -intervals with  $k_{\min} = 0.11$  (blue dots), 0.50 (green dots), 0.70 (red dots), 0.90 (light blue dots) and  $1.10 h \text{ Mpc}^{-1}$  (magenta dots).

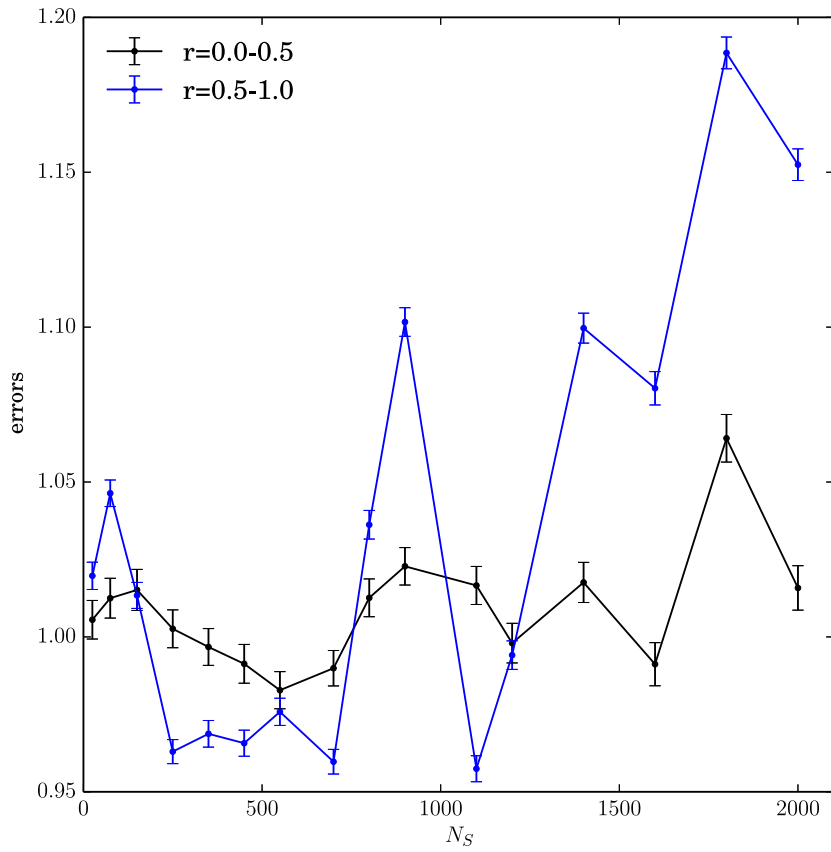


**Figure 7.6:** Ratio of the sum of the left-hand side of the off-diagonal components of Eq. (7.7) relative to that of the right-hand side for wavenumber configurations corresponding to correlation matrix elements with values in the range  $0 < r < 0.5$  (black points) and  $0.5 < r < 1$  (blue points). Error-bars indicate the dispersion.

in the range  $0.11 < k [h \text{ Mpc}^{-1}] < 1.22$  which we plot in Fig. 7.7 as a function of  $N_s$ . Differently from the covariance errors we notice that deviations from the expected scaling do not exceed 5% level in the range of  $N_s$  considered. Similarly the off-diagonal components do not show significant departures above 5% independently of the level of correlation as shown in Fig. 7.8.

### 7.3 Covariance Estimation Errors and Parameter Forecast

We perform a Fisher matrix analysis to investigate the impact of covariance matrix errors on the cosmological parameter uncertainties. In principle the use of analytical models of the covariance avoids such errors [see e.g. 162, 115, for work in this direction] and thus no sampling error will contribute to the model parameter uncertainties. Nonetheless, such models still need to match numerical simulation results and as shown by Ref. [186] in the context of the halo model, model calibration uncertainties will propagate in the parameter estimation errors.

In the following we assume as fiducial cosmology the flat  $\Lambda$ CDM model best-fit to the WMAP-7 years used for the DEUS-PUR simulations. We model the galaxy power spectrum at a given redshift  $z$  as

$$P_z^g(k) = b_z^2 P_z(k), \quad (7.11)$$

where  $b_z$  is a constant and  $P_z(k)$  is the non-linear matter power spectrum, while we model the galaxy power spectrum covariance matrix as in [163]:

$$\text{cov}_z^g(k_i, k_j) = b_z^4 \widehat{\mathcal{C}}_{ij} + b_z^2 [P_z(k_i) + P_z(k_j)] \bar{n}_g^{-1}(z) + \bar{n}_g^{-2}(z), \quad (7.12)$$

where  $\widehat{\mathcal{C}}_{ij}$  is the matter power spectrum covariance matrix at redshift  $z$  computed from the DEUS-PUR simulations and  $\bar{n}_g(z)$  is the mean number density of galaxies.

We consider a Euclid-like survey [98] with measurements of the galaxy power spectrum in  $N_z = 5$  redshift bins in the range  $0.2 \leq z \leq 2$  and mean galaxy number density  $\bar{n}_g(z)$  as given in Table 7.1. Notice that this setting does not reflect precisely the Euclid survey: first of all our simulations have a smaller volume with respect to the expected effective volume of the Euclid surveys. Moreover, we consider redshifts for which we have the simulation snapshots, that not always coincide with the Euclid redshift bins. The galaxy

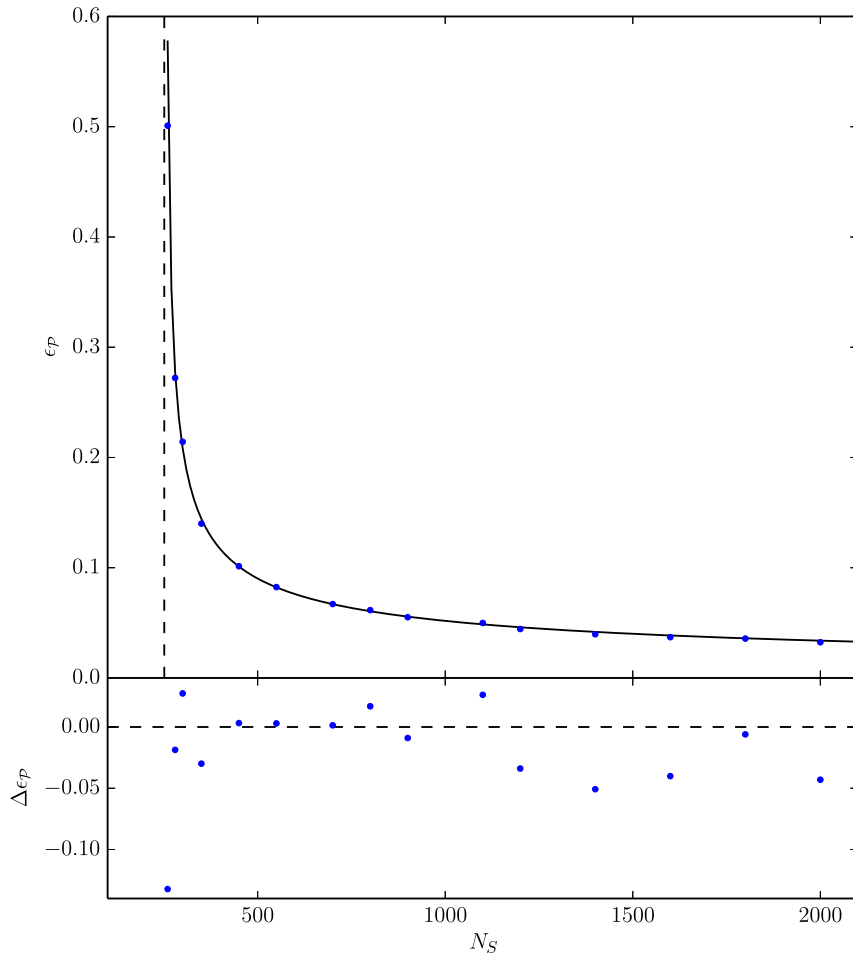


**Figure 7.7:**  $\epsilon_P$  as a function of  $N_s$  in the range  $0.11 < k [h \text{ Mpc}^{-1}] < 1.22$ . Black solid line is the expected scaling from the inverse-Wishart distribution. In the bottom panel is shown the relative difference.

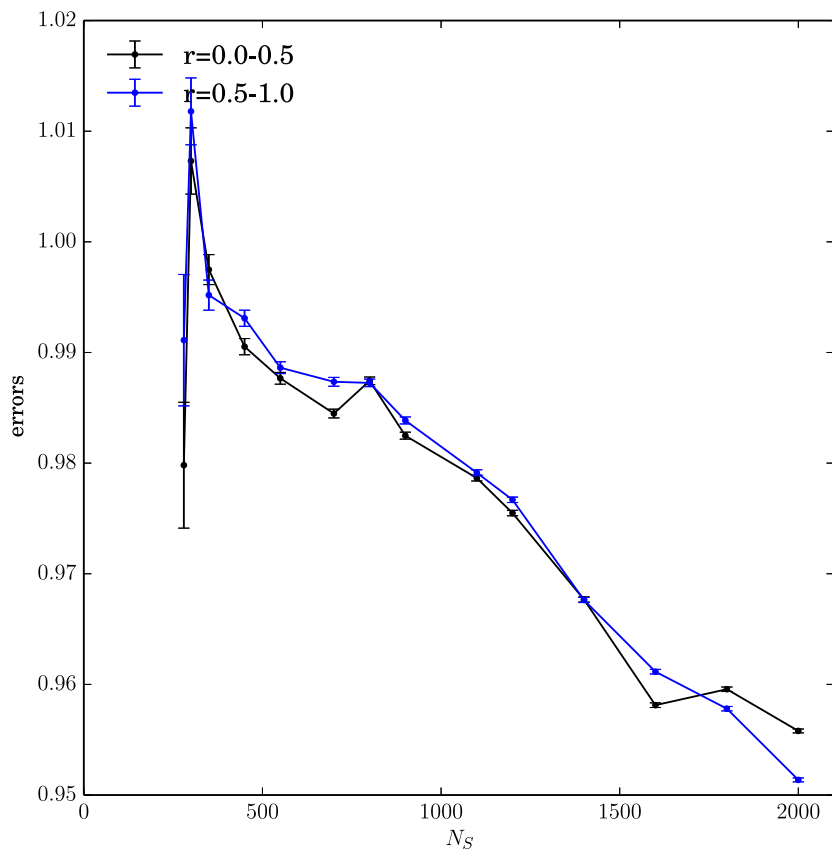


**Figure 7.8:** As in Fig. 7.6 for the variance of the precision matrix.

$z$	$\bar{n}_g(z)$
0.5	$4.2 \times 10^{-3}$
0.7	$2.99 \times 10^{-3}$
1.0	$1.81 \times 10^{-3}$
1.5	$0.77 \times 10^{-3}$
2.0	$0.15 \times 10^{-3}$

**Table 7.1:** Central redshift of the redshift bins and mean galaxy number density as expected from a Euclid-like survey [98].

number densities listed in Table 7.1 are as close as possible to those listed in Ref. [98], so that the level of shot-noise that we consider is representative of future galaxy surveys. In each bin we consider  $N_k = 250$  band power measurements in the range  $0.03 < k [h \text{ Mpc}^{-1}] < 1.22$ . We consider the following vector of model parameters  $\theta = \{\Omega_m, w, \sigma_8, n_s, \Omega_b, b_1, \dots, b_{N_z}\}$ . The Fisher matrix reads as

$$F_{\alpha\beta} = \sum_{l=1}^{N_z} \sum_{i,j=1}^{N_k} \frac{\partial P_{z_l}^g}{\partial \theta_\alpha}(k_i) \frac{\partial P_{z_l}^g}{\partial \theta_\beta}(k_j) \text{cov}_{z_l}^g(k_i, k_j), \quad (7.13)$$

where we have neglected correlations among different redshift bins. We compute the derivatives of the non-linear matter power spectrum using a five-point stencil approximation:

$$\frac{\partial P_z^g}{\partial \theta_\alpha} \approx \frac{2 P_z^g(\hat{\theta}_\alpha + \Delta\theta_\alpha) - P_z^g(\hat{\theta}_\alpha - \Delta\theta_\alpha)}{3 \Delta\theta_\alpha} + \quad (7.14)$$

$$+ \frac{P_z^g(\hat{\theta}_\alpha + 2\Delta\theta_\alpha) - P_z^g(\hat{\theta}_\alpha - 2\Delta\theta_\alpha)}{12\Delta\theta_\alpha}, \quad (7.15)$$

where  $\hat{\theta}_\alpha$  is the fiducial parameter value and  $\Delta\theta_\alpha = 0.05 \hat{\theta}_\alpha$  and the non-linear power spectra are computed with the emulator PkANN<sup>1</sup> [3].

In Fig. 7.9 we plot the marginalised 1 and  $2\sigma$  contours obtained assuming a simple Gaussian covariance with diagonal components proportional to the linear matter power spectrum of the fiducial cosmology (dashed lines) and the errors obtained with the covariance from the full ensemble of DEUS-PUR simulations (continuous lines). As we can see, assuming a Gaussian covariance underestimates the model parameter uncertainties. This can be inferred

<sup>1</sup><http://zuserver2.star.ucl.ac.uk/fba/PkANN/>

$\theta$	$\sigma_{\theta}^G$	$\sigma_{\theta}^{NG}$
$\Omega_m$	$8.4 \times 10^{-5}$	$1.8 \times 10^{-3}$
$\sigma_8$	$2.5 \times 10^{-3}$	$4.3 \times 10^{-3}$
$\Omega_b$	$7.0 \times 10^{-4}$	$7.9 \times 10^{-4}$
$n_s$	$9.4 \times 10^{-3}$	$9.1 \times 10^{-3}$
$w$	$1.7 \times 10^{-2}$	$1.7 \times 10^{-2}$

**Table 7.2:** Marginalised  $1\sigma$  Fisher matrix errors on the cosmological parameters obtained using a Gaussian covariance (second column) and the DEUS-PUR covariance (third column).

more clearly in Table 7.2 where we report the marginalised  $1\sigma$  errors on the cosmological parameters for the two cases. The discrepancy is maximal in the case of  $\Omega_m$ , for which the use of a linear covariance underestimates the  $1\sigma$  error by  $\sim 95\%$ . Smaller differences occur for  $\sigma_8$  and  $\Omega_b$  though still exceeding the  $\sim 10\%$  level. This highlights the need of fully non-linear covariances in order to have precise estimates of the uncertainty in cosmological parameter estimates.

In Fig. 7.10 we plot the ratio of the  $1\sigma$  marginalised model parameter errors  $\sigma_{\theta}$  as a function of the number of simulations with respect the errors obtained using the full DEUS-PUR sample. We can see that the fractional error contribution of the sample covariance to the parameter errors reduces to sub-percent level for  $N_s > 5000$ . This means that future galaxy surveys will need large number of realisations to compute covariance matrices. Advancements in numerical N-body simulations techniques may render this task less challenging in the future. Nevertheless the development of theoretical approaches capturing the relevant features of the non-linear collapse of matter on the scale of interest should be pursued to facilitate the statistical analysis of future data as well as to infer information on the late time clustering of matter.

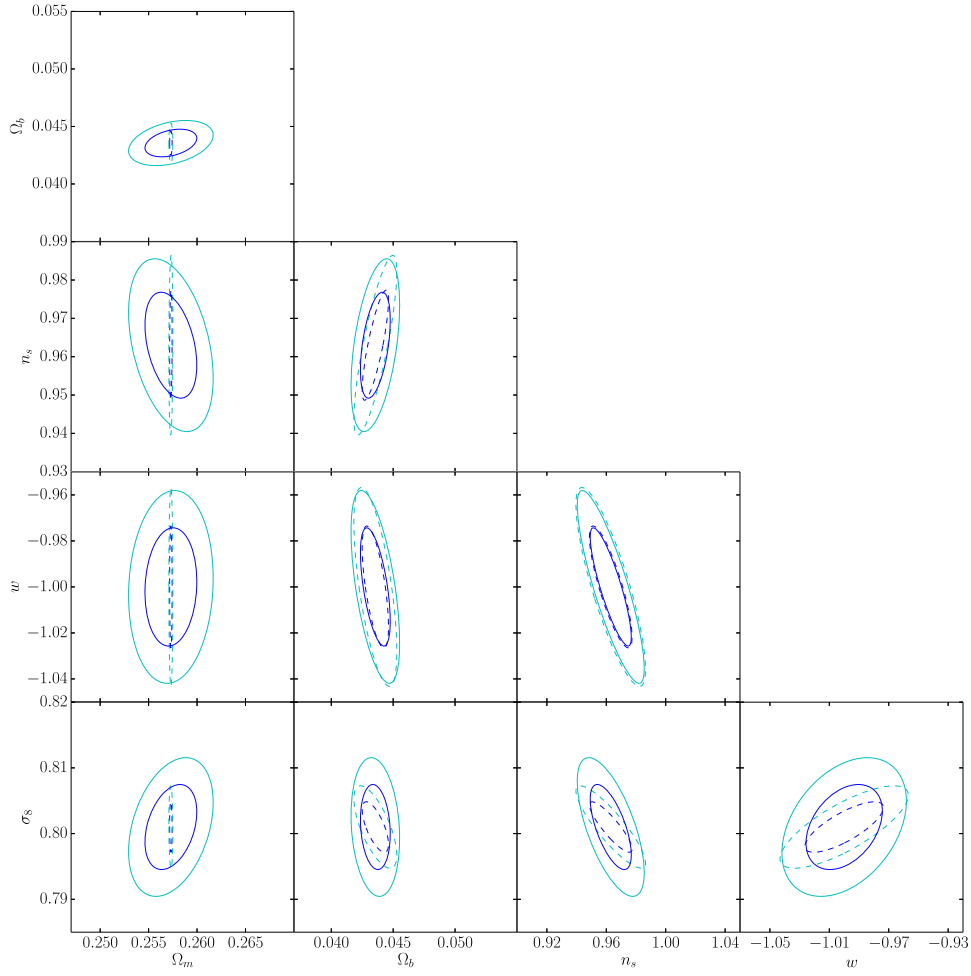


**Figure 7.9:** Fisher matrix 1 and  $2\sigma$  contours in the case of a Gaussian linear matter power spectrum covariance (dashed lines) and in the case of the fully non-linear covariance matrix from the DEUS-PUR simulation ensemble (continuous lines) for various combinations of the cosmological parameters, marginalised over the constant redshift bin bias parameters.

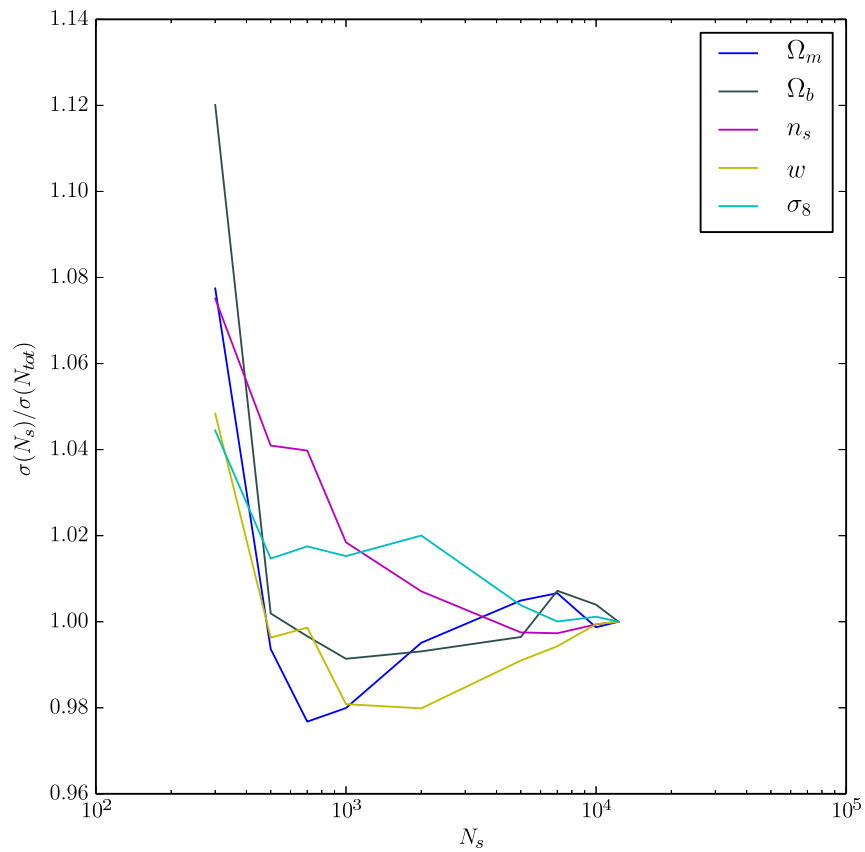


**Figure 7.10:** Fractional error contribution to the cosmological parameter errors of the numerically estimated covariance as a function of the number of simulations relative to the errors obtained using the covariance from the full DEUS-PUR sample.

## Part III

# Numerical methods for Dark Energy simulations



## Chapter 8

# Numerical methods for clustering Dark Energy simulations

As we have seen in §2.5, the success of the  $\Lambda$ CDM model remains purely empirical as the physical origin of the cosmic dark components remains unknown. In the lack of new fundamental principles which may guide the DE theoretical model building, there is hope nevertheless that the next generation of cosmological observations may reveal hints of the new physics underlying the DE phenomenon. This relies upon modelling DE as a perfect fluid characterised by a homogeneous pressure and density that are related through an equation of state parameter,  $w$ , the cosmological constant case corresponding to  $w = -1$ . Such an approach allows us to test properties of DE through observations. Future cosmological observations are specifically designed to determine the value of  $w$  with great accuracy and to test its behaviour as a function of time. However, if DE is a dynamical component (i.e.  $w \neq -1$ ), general covariance imposes that the DE energy density and pressure have to vary in space too. This suggests that the detection of the clustering of DE through observations of the cosmic structures may provide smoking gun evidence of the dynamical nature of the DE phenomenon. In this case an additional macroscopic quantity specifies the properties of the DE fluid, namely the speed of propagation of density and pressure perturbations,  $c_s$ .

Bounds on the DE equation of state and speed of sound can be translated into constraints of its microscopic properties, since these quantities can be related to terms in an effective field theory lagrangian of DE (see e.g. [50, 74]). For instance quintessence models in which DE is the result of the dynamics of a minimally coupled scalar field are characterised by  $c_s^2 = 1$  (in units of speed of light  $c = 1$ ) [34], while k-essence models in which DE

is due to a scalar field with a non-canonical kinetic term have  $c_s^2 \approx 0$  [14]. It is important to notice that a perfect fluid approach is not limited to the phenomenological study of DE. For instance models of unified DM and DE [23] as well as alternative Dark Matter scenarios (see e.g. [92]) are described as dark fluids characterised by an equation of state and a speed of sound. For this reason throughout this Chapter we may refer indistinctly to Dark Energy or dark fluids.

The clustering properties of Dark Energy can be tested through observations of the cosmic distribution of matter at different scales and times. On the large scales, linear perturbation theory can be used to predict the effect of DE inhomogeneities on the evolution of matter density perturbations [66, 21, 47]. However, since DE is a late time phenomenon, the presence of DE perturbations does not drastically alter the linear regime of matter collapse that determines the distribution of structures on the large scales. Consequently, deviations from  $\Lambda$ CDM predictions are well within cosmic variance uncertainties and available data remain uninformative [47, 56].

This may not be the case at small scales and late time where the collapse process is highly non-linear. For quintessence-like fluids characterised by  $c_s^2 = 1$  there are no relevant effects since any DE perturbation on sub-horizon scales has been damped by free-streaming. In such a case DE affects the non-linear structure formation by only altering the linear growth of structures due to its effects on the background expansion. Thus, in these models the non-linear clustering of matter can be investigated using standard N-body simulations [6, 91, 48]. Instead, in models with  $c_s^2 < 1$  perturbations may cluster at small scales. Studies of the non-linear regime of inhomogeneous dark energy have been limited to the fully clustered case  $c_s^2 = 0$  in the context of the spherical collapse model [118, 49, 19] or higher-order perturbation theory [145, 12, 13].

A thorough cosmological analysis of the non-linear clustering of matter in the presence of DE inhomogeneities has never been performed. This requires performing cosmological simulations that account not only for the non-linear evolution of the DM density field as sampled by N-body particles, but also the gravitational collapse of the DE fluid fluctuations. The difficulty in realising such simulations arises from the fact that the DE energy density does not scale with the scale factor as  $a^{-3}$ . Because of this, the mass of DE enclosed in a finite volume element is not conserved. Moreover, if  $0 < c_s^2 < 1$  pressure gradients generate fluid-dynamical effects at small scales. These peculiarities imply that the clustering of DE cannot be followed through the

gravitational dynamics of N-body lagrangian particles, instead an Eulerian approach is necessary.

The work presented here intends to fill this gap. We will show that the non-linear evolution of dark energy fluctuations is described by hyperbolic Euler equations which can be cast in the form of modified equations of hydrodynamics. Numerical schemes that are best suited to solve this type of equations are based on Finite Volume (FV) methods. Many of these schemes are already implemented in cosmological simulation codes such as ENZO [32], FLASH [72] or RAMSES [170] to follow the cosmological collapse of baryonic gas. These codes use high-order variants of the Godunov scheme originally introduced in [75] and have been shown to provide accurate solutions to a variety of problems in gas dynamics. The accuracy of these schemes relies on their ability to capture discontinuities in the fluid flow and correctly predict the velocity of propagating waves. The starting point of these methods is the solution of the Riemann problem. Exact and approximate solutions have been derived for several systems including real gases [40], inviscid flows of perfect gases [76], gases with generic equations of state [113], compressible liquids [88].

Here, we present a detailed study of the Riemann problem for cosmic dark fluid as a first step toward a cosmological study of the non-linear structure formation in inhomogeneous DE models. We derive an exact solution of the Riemann problem and construct several approximated solvers that in combination with Godunov-type schemes can efficiently solve the non-linear perturbation equations of DE. In future work we will apply these schemes to the study of the spherical collapse of a inhomogeneous DE fluid in the presence of pressure gradients.

## 8.1 Euler Equations for Dark Energy Fluids

The equations describing the evolution of a dark energy fluid under the influence of Newtonian gravity in a flat Friedmann-Lemaitre-Robertson-Walker background have been derived in [145]. In cartesian coordinates these read as:

$$\frac{\partial \rho}{\partial \tau} + 3\mathcal{H}(\rho + p) + \vec{\nabla} \cdot [(\rho + p)\vec{v}] = 0 \quad (8.1)$$

$$\frac{\partial \vec{v}}{\partial \tau} + \mathcal{H}\vec{v} + (\vec{v} \cdot \vec{\nabla})\vec{v} = -\frac{1}{\rho + p} \left( \vec{\nabla} p + \vec{v} \frac{\partial p}{\partial \tau} \right) - \vec{\nabla} \Phi, \quad (8.2)$$

where  $\rho$  and  $p$  are the DE energy density and pressure respectively,  $\vec{v}$  is the DE peculiar velocity with respect to the Hubble flow,  $\tau$  is the conformal time,  $\mathcal{H} = d \ln a / d\tau$  is the Hubble rate with  $a$  the scale factor and  $\Phi$  is the gravitational potential. These equations are valid for non-relativistic peculiar velocities ( $v \ll 1$ ) and on scales smaller than the horizon.

Given the non-barotropic nature of the DE fluid it is convenient to split the evolution of the background density  $\bar{\rho}$  and pressure  $\bar{p}$  from that of the fluctuations  $\delta\rho$  and  $\delta p$  such that

$$\rho(\vec{x}, \tau) \equiv \bar{\rho}(\tau) + \delta\rho(\vec{x}, \tau) \quad (8.3)$$

$$p(\vec{x}, \tau) \equiv \bar{p}(\tau) + \delta p(\vec{x}, \tau), \quad (8.4)$$

where  $\bar{p} = w\bar{\rho}$  and

$$\frac{\partial \bar{\rho}}{\partial \tau} = -3\mathcal{H}(1+w)\bar{\rho}. \quad (8.5)$$

In a generic frame density and pressure perturbations are related as [84]:

$$\vec{\nabla} \delta p = c_s^2 \vec{\nabla} \delta \rho + 3\mathcal{H}(1+w)(c_s^2 - c_a^2) \bar{\rho} \vec{v}, \quad (8.6)$$

with

$$c_a^2 \equiv \frac{\dot{\bar{p}}}{\dot{\bar{\rho}}} = w - \frac{\dot{w}}{3\mathcal{H}(1+w)}, \quad (8.7)$$

that is the adiabatic sound speed of the fluid (dots indicate derivatives with respect to conformal time). If the second term in Eq. (8.6), which is proportional to the DE peculiar velocity, remains sufficiently small with respect to the first one, which is proportional to the density gradient, then  $\delta p = c_s^2 \delta \rho$ . This approximation is especially valid for small values of the sound speed that characterise clustered dark energy models. Substituting this relation in Eq. (8.4) and introducing the rescaled density variable

$$\Delta \equiv 1 + w + (1 + c_s^2) \delta, \quad (8.8)$$

we can cast Eq. (8.1) and Eq. (8.2) in a quasi-conservative form:

$$\frac{\partial \Delta}{\partial \tau} + (1 + c_s^2) \vec{\nabla} \cdot (\Delta \vec{v}) = 3\mathcal{H}[(1 + w)(c_s^2 - c_a^2) \vec{v} + (w - c_s^2) \Delta] \quad (8.9)$$

$$\frac{\partial(\Delta \vec{v})}{\partial \tau} + \vec{\nabla} \cdot (\Delta \vec{v} \otimes \vec{v}) + \frac{c_s^2}{1 + c_s^2} \vec{\nabla} \Delta = \mathcal{H}(3w - 1) \Delta \vec{v} - \Delta \vec{\nabla} \Phi, \quad (8.10)$$

where we have intentionally written the friction terms due to the cosmic expansion on the right-hand side to distinguish the advection part of the

Euler equations from non-advecting time-dependent source terms. As we can see, the equation of state parameter  $w$  only enters in the friction terms, while the advection of density perturbations and velocities only depends on the sound speed parameter. Casted in this form, Eq. (8.9) and (8.10) are a hyperbolic system of non-linear equations describing the dynamical evolution of dark energy fluctuations in an expanding background under the effect of Newtonian gravitational potentials. It is worth noticing that in the case of a vanishing equation of state and sound speed, and neglecting the source terms the above equations reduce to standard conservation laws of mass and momentum.

## 8.2 The Riemann Problem

Let us consider the Euler equation in one spatial dimension and write Eq. (8.9) and (8.10) in a compact state-vector form

$$\mathbf{U}_\tau + \mathbf{F}(\mathbf{U})_x = \mathbf{S}(\mathbf{U}), \quad (8.11)$$

where the indices denote partial derivatives,  $\mathbf{U}$  is a state vector of unknowns,  $\mathbf{F}(\mathbf{U})$  is a vector of fluxes and  $\mathbf{S}(\mathbf{U})$  a vector of sources respectively. These are given by

$$\mathbf{U} = \begin{bmatrix} u_1 \\ u_2 \end{bmatrix}, \quad \mathbf{F} = \begin{bmatrix} (1 + c_s^2)u_2 \\ \frac{u_2^2}{u_1^2} + \frac{c_s^2}{1+c_s^2}u_1 \end{bmatrix}, \quad \mathbf{S} = \begin{bmatrix} 3\mathcal{H}(1+w)(c_s^2 - c_a^2) + 3\mathcal{H}(w - c_s^2)u_1 \\ \mathcal{H}(3w - 1)u_2 - u_1\Phi_x \end{bmatrix}, \quad (8.12)$$

with  $u_1 = \Delta$  and  $u_2 = \Delta v$ . Hereafter, we will extensively follow Toro's textbook [171] to which we refer interested readers for a detailed presentation of numerical methods in fluid dynamics.

The Riemann problem (RP) is an initial value problem (IVP) of the advection equation

$$\mathbf{U}_\tau + \mathbf{F}(\mathbf{U})_x = 0, \quad (8.13)$$

with initial conditions

$$\mathbf{U}(x, 0) = \begin{cases} \mathbf{U}_L & \text{if } x < 0 \\ \mathbf{U}_R & \text{if } x > 0 \end{cases} \quad (8.14)$$

In general, the solution of RP for a  $m \times m$  non-linear hyperbolic system consists of  $m + 1$  constant states separated by  $m$  waves in the plane  $x - \tau$ . In our case  $m = 2$ , hence the solution of the Riemann problem consists of three

constant states separated by two waves (see Fig. 8.1). These can be either shocks, rarefaction or contact waves associated with the so called *characteristic fields* of the advection equation (Eq.(8.13)). The characteristics are curves in the plane  $x - \tau$  along which Eq.(8.13) reduces to an ordinary differential equation. In order to determine these curves let us rewrite Eq. (8.13) as

$$\mathbf{U}_\tau + \mathbf{A}(\mathbf{U})\mathbf{U}_x = 0, \quad (8.15)$$

where  $\mathbf{A}(\mathbf{U})$  is the Jacobian matrix of the flux vector<sup>1</sup>

$$\mathbf{A}(\mathbf{U}) \equiv \frac{\partial \mathbf{F}}{\partial \mathbf{U}} = \begin{bmatrix} 0 & 1 + c_s^2 \\ \frac{c_s^2}{1+c_s^2} - v^2 & 2v \end{bmatrix}. \quad (8.19)$$

The eigenvalues of the Jacobian matrix  $\mathbf{A}(\mathbf{U})$  are given by

$$\lambda_\pm = v \pm c_s \sqrt{1 - v^2}, \quad (8.20)$$

these roots are real and distinct if and only if  $c_s \neq 0$ . In such a case we have  $\lambda_-(v) < \lambda_+(v)$  and the system is *strictly hyperbolic*. Notice that since we are considering Dark Energy models for which peculiar velocities are non-relativistic ( $v \ll 1$ ) the wave structure of the system approximately reproduces that of an isothermal fluid with constant sound speed.

The right eigenvectors associated to  $\lambda_\pm$  are given by

$$\mathbf{R}_+ = \begin{bmatrix} 1 + c_s^2 \\ v + c_s \sqrt{1 - v^2} \end{bmatrix}, \quad \mathbf{R}_- = \begin{bmatrix} 1 + c_s^2 \\ v - c_s \sqrt{1 - v^2} \end{bmatrix}, \quad (8.21)$$

---

<sup>1</sup>Notice that Eq. (8.13) can be rewritten also in terms of the primitive state variables  $\mathbf{W} = (\Delta, v)$ :

$$\mathbf{W}_\tau + \tilde{\mathbf{A}}(\mathbf{W})\mathbf{W}_x = 0, \quad (8.16)$$

where

$$\tilde{\mathbf{A}}(\mathbf{W}) = \begin{bmatrix} (1 + c_s^2)v & (1 + c_s^2)\Delta \\ \frac{c_s^2}{\Delta} \left( \frac{1}{1+c_s^2} - v^2 \right) & (1 - c_s^2)v \end{bmatrix}, \quad (8.17)$$

since conservative and primitive variables are related by a linear transformation  $d\mathbf{U} = \Lambda d\mathbf{W}$  with

$$\Lambda = \begin{bmatrix} 1 & 0 \\ v & \Delta \end{bmatrix} \quad \Lambda^{-1} = \begin{bmatrix} 1 & 0 \\ -\frac{v}{\Delta} & \frac{1}{\Delta} \end{bmatrix} \quad (8.18)$$

it is easy to show that  $\mathbf{A}(\mathbf{U}) = \Lambda \tilde{\mathbf{A}}(\mathbf{W})\Lambda^{-1}$ . This implies that the Jacobian matrix whether written in terms of primitive variables or conservative ones has identical eigenvalues, while the corresponding eigenvectors are related by a linear transformation. Therefore, the Riemann problem admits the same wave structure in the two formulations.

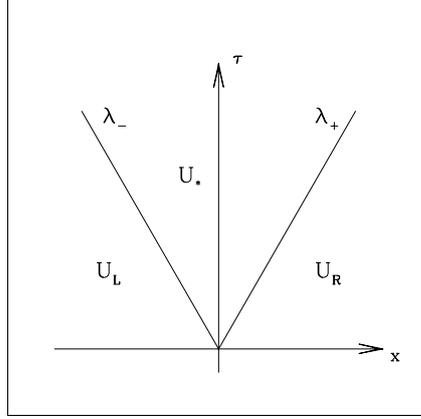


**Figure 8.1:** Structure of the solution of Riemann problem for a  $2 \times 2$  hyperbolic system.

while the left eigenvectors read as

$$\begin{aligned} \mathbf{L}_+ &= \left[ \frac{1}{2\Delta(1+c_s^2)} \left( 1 + \frac{vc_s^2}{\sqrt{1-v^2}} \right), \quad \frac{1}{2c_s\sqrt{1-v^2}} \right], \\ \mathbf{L}_- &= \left[ \frac{1}{2\Delta(1+c_s^2)} \left( 1 - \frac{vc_s^2}{\sqrt{1-v^2}} \right), \quad \frac{-1}{2c_s\sqrt{1-v^2}} \right] \end{aligned} \quad (8.22)$$

and satisfy the relation  $\mathbf{L}_\pm \cdot \mathbf{R}_\pm = \delta_{\pm\pm}$ , where  $\delta_{\pm\pm}$  is the Kronecker symbol.

The eigenvalues  $\lambda_\pm$  define the characteristic fields of the system, these are said to be “genuinely non-linear” if  $\vec{\nabla}_{\mathbf{U}} \lambda_\pm \cdot \mathbf{R}_\pm \neq 0$ . In such a case the family of waves associated to these fields are either shocks or rarefactions. Using Eq. (8.20) and Eq. (8.21) we obtain

$$\vec{\nabla}_{\mathbf{U}} \lambda_\pm \cdot \mathbf{R}_\pm = \pm \frac{c_s}{\Delta\sqrt{1-v^2}} [1 + v^2(1+c_s^2)], \quad (8.23)$$

hence the characteristic fields are genuinely non-linear if and only if  $c_s \neq 0$ . In this case the waves associated to  $\lambda_\pm$  are rarefactions or shocks.

In Fig. 8.1 we sketch the structure of the solution of the Riemann problem. Given the data to the left ( $\mathbf{U}_L$ ) and the right ( $\mathbf{U}_R$ ) of the initial discontinuity at  $x = 0$ , we want to determine the state ( $\mathbf{U}_*$ ) in the region enclosed

between the left and right waves and derive the solution of the Riemann problem,  $\mathbf{U}(x, \tau)$ . In Section 8.2.4 we will provide an exact solution in terms of primitive variables, however it is first useful to derive a set of equations that relate state variables across different wave patterns.

### 8.2.1 Generalised Riemann Invariants

These are ordinary differential equations which relate state variables across contact and rarefaction waves (see [90] for a detailed discussion). In the case of a  $2 \times 2$  system we have

$$\frac{du_1}{r_1^\pm} = \frac{du_2}{r_2^\pm} \quad (8.24)$$

where  $r_1^\pm$  and  $r_2^\pm$  are the two components of the right-eigenvectors  $\mathbf{R}_\pm$ . Using Eq. (8.21) and after some algebra we can write these relations in terms of primitive variables:

$$\frac{d\Delta}{\Delta} = -\frac{(1 + c_s^2)dv}{c_s(vc_s - \sqrt{1 - v^2})} \quad (\lambda = \lambda_+) \quad (8.25)$$

$$\frac{d\Delta}{\Delta} = -\frac{(1 + c_s^2)dv}{c_s(vc_s + \sqrt{1 - v^2})} \quad (\lambda = \lambda_-) \quad (8.26)$$

these can be integrated analytically to obtain the Riemann Invariants (RI)

$$\ln \Delta - \frac{1}{c_s} \arcsin(v) - \operatorname{arctanh}\left(\frac{vc_s}{\sqrt{1 - v^2}}\right) + \ln[1 - (1 + c_s^2)v^2] = \text{const.} \quad (\lambda = \lambda_+) \quad (8.27)$$

$$\ln \Delta + \frac{1}{c_s} \arcsin(v) + \operatorname{arctanh}\left(\frac{vc_s}{\sqrt{1 - v^2}}\right) + \ln[1 - (1 + c_s^2)v^2] = \text{const.} \quad (\lambda = \lambda_-) \quad (8.28)$$

which express the conservation of these relations across the waves associated to the characteristic fields  $\lambda_+$  and  $\lambda_-$  respectively.

### 8.2.2 Rarefaction Waves

Rarefaction waves are smooth solutions which connect two states without discontinuities. They satisfy the condition  $\lambda_\pm(\mathbf{U}_L) < \lambda_\pm(\mathbf{U}_R)$  and Riemann invariants hold across the rarefactions. We can use the Riemann invariants to relate a known state to the left (right) of the wave to that onto the right (left).

### Left Rarefactions

Let us consider a left rarefaction wave associated with  $\lambda_-$ -field. Using the Riemann invariant Eq. (8.28) we can relate the known state  $\mathbf{U}_L$  to the unknown state in the star region  $\mathbf{U}_*$  shown in Fig. 8.1. It is useful to introduce the auxiliary function

$$g_{Lr}(v) \equiv \frac{1}{c_s} \arcsin(v) + \operatorname{arctanh}\left(\frac{vc_s}{\sqrt{1-v^2}}\right) + \ln[1 - (1 + c_s^2)v^2], \quad (8.29)$$

hence from Eq. (8.28) we obtain

$$g_{Lr}(v_*) = \ln \frac{\Delta_L}{\Delta_*} + g_{Lr}(v_L), \quad (8.30)$$

this implicit relation can be inverted to obtain

$$v_* = f_{Lr}(\Delta_*, \mathbf{W}_L), \quad (8.31)$$

where we have denoted with  $f_{Lr}$  the inverse function  $g_{Lr}^{-1}$ .

The rarefaction wave is enclosed in a region delimited by the *head* of the wave moving with speed  $S_{HLr} = \lambda_-(v_L)$  and the *tail* with speed  $S_{TLr} = \lambda_-(v_*)$ . The evolution of this region, also dubbed *rarefaction fan*, can be obtained by integrating along the characteristic equation  $dx/d\tau = \lambda_-(v)$  with initial condition  $x(0) = x_0$  (the location of the discontinuity at initial time), this gives

$$\frac{x - x_0}{\tau} = \lambda_-(v_{Lfan}), \quad (8.32)$$

which can be inverted to obtain  $v_{Lfan}(x)$  at any given time.  $\Delta_{Lfan}(x)$  inside the fan is then obtained using the generalised Riemann invariant Eq. (8.28):

$$\ln \Delta_{Lfan}(x) = \ln \Delta_L + g_{Lr}(v_L) - g_{Lr}(v_{Lfan}(x)). \quad (8.33)$$

### Right Rarefactions

Let us now consider a right rarefaction wave associated with the characteristic field  $\lambda_+$ . Using the Riemann invariant Eq. (8.27) we can relate the known state  $\mathbf{U}_R$  to the right of the wave to the unknown state in the star region  $\mathbf{U}_*$  shown in Fig. 8.1. Let us introduce the auxiliary function

$$g_{Rr}(v) \equiv -\frac{1}{c_s} \arcsin(v) - \operatorname{arctanh}\left(\frac{vc_s}{\sqrt{1-v^2}}\right) + \ln[1 - (1 + c_s^2)v^2], \quad (8.34)$$

from Eq. (8.27) we obtain

$$g_{Rr}(v_*) = \ln \frac{\Delta_R}{\Delta_*} + g_{Rr}(v_R), \quad (8.35)$$

this implicit relation can be inverted to obtain

$$v_* = f_{\text{Rr}}(\Delta_*, \mathbf{W}_{\text{R}}), \quad (8.36)$$

where we have denoted with  $f_{\text{Rr}}$  the inverse function  $g_{\text{Rr}}^{-1}$ .

The right rarefaction fan is delimited by the head of the wave moving with speed  $S_{\text{HRr}} = \lambda_+(v_{\text{R}})$  and the tail with speed  $S_{\text{TRr}} = \lambda_+(v_*)$ . The evolution of the fan region is given by solving  $dx/d\tau = \lambda_+(v)$  with  $x(0) = x_0$  (the location of the discontinuity at initial time):

$$\frac{x - x_0}{\tau} = \lambda_+(v_{\text{Rfan}}), \quad (8.37)$$

this can be inverted to infer  $v_{\text{Rfan}}(x)$ . Then, using the Riemann invariant Eq. (8.27) we obtain  $\Delta_{\text{Rfan}}(x)$  inside the fan:

$$\ln \Delta_{\text{Rfan}}(x) = \ln \Delta_{\text{R}} + g_{\text{Rr}}(v_{\text{R}}) - g_{\text{Lr}}(v_{\text{Rfan}}(x)). \quad (8.38)$$

### 8.2.3 Shock Waves

Shock waves are discontinuous solutions which connect two states through a single jump-discontinuity condition. By denoting with  $S$  the propagation speed of the shock wave, it can be shown that across shocks hold the Rankine-Hugoniot (RH) conditions:

$$\Delta \mathbf{F} = S \Delta \mathbf{U}. \quad (8.39)$$

We can use the RH conditions to relate a known state to the left (right) of the shock to that unknown to the right (left).

#### Left Shocks

Let us consider a shock moving from right to left separating the known initial state  $\mathbf{U}_{\text{L}}$  from the unknown state  $\mathbf{U}_*$  in the star region represented in Fig. 8.1. Using Eq. (8.39) we have a system of algebraic equations in the primitive variables which reads as

$$(1 + c_s^2)(\Delta_{\text{L}} v_{\text{L}} - \Delta_* v_*) = S(\Delta_{\text{L}} - \Delta_*) \quad (8.40)$$

$$\frac{c_s^2}{1 + c_s^2}(\Delta_{\text{L}} - \Delta_*) + (\Delta_{\text{L}} v_{\text{R}}^2 - \Delta_* v_*^2) = S(\Delta_{\text{L}} v_{\text{L}} - \Delta_* v_*), \quad (8.41)$$

this is an algebraic system of two equations and three unknowns  $(\Delta_*, v_*, S)$ . We can solve for  $S$  and  $v_*$  to find

$$\frac{S_{Ls}}{1+c_s^2} = \frac{\Delta_L v_L}{\Delta_L + c_s^2 \Delta_*} - \sqrt{\frac{\Delta_L^2 v_L^2}{(\Delta_L + c_s^2 \Delta_*)^2} - \frac{\Delta_L v_L^2}{\Delta_L + c_s^2 \Delta_*} + \frac{\Delta_* c_s^2}{(\Delta_L + c_s^2 \Delta_*)(1+c_s^2)}} \quad (8.42)$$

$$v_* \equiv f_{Ls}(\Delta_*, \mathbf{W}_L) = \frac{\Delta_L}{\Delta_*} v_L - \frac{S_{Ls}}{1+c_s^2} \frac{\Delta_L - \Delta_*}{\Delta_*}, \quad (8.43)$$

where  $S_{Ls}$  is the negative root of the quadratic equation obtained from Eq. (8.40) and (8.41), this choice is consistent with the fact that the left shock moves from the right to the left.

### Right Shocks

Let us consider a shock moving from the left to the right separating the known initial state  $\mathbf{U}_R$  from the unknown state  $\mathbf{U}_*$  in the star region represented in Fig. 8.1. Using the Rankine-Hugoniot conditions we obtain the system of algebraic equations

$$(1+c_s^2)(\Delta_* v_* - \Delta_R v_R) = S(\Delta_* - \Delta_R) \quad (8.44)$$

$$\frac{c_s^2}{1+c_s^2}(\Delta_* - \Delta_R) + (\Delta_* v_*^2 - \Delta_R v_R^2) = S(\Delta_* v_* - \Delta_R v_R), \quad (8.45)$$

this is an algebraic system of two equations and three unknowns  $(\Delta_*, v_*, S)$ , solving for  $S$  and  $v_*$  we find

$$\frac{S_{Rs}}{1+c_s^2} = \frac{\Delta_R v_R}{\Delta_R + c_s^2 \Delta_*} + \sqrt{\frac{\Delta_R^2 v_R^2}{(\Delta_R + c_s^2 \Delta_*)^2} - \frac{\Delta_R v_R^2}{\Delta_R + c_s^2 \Delta_*} + \frac{\Delta_* c_s^2}{(\Delta_R + c_s^2 \Delta_*)(1+c_s^2)}} \quad (8.46)$$

$$v_* \equiv f_{Rs}(\Delta_*, \mathbf{W}_R) = \frac{\Delta_R}{\Delta_*} v_R + \frac{S_{Rs}}{1+c_s^2} \frac{\Delta_* - \Delta_R}{\Delta_*}, \quad (8.47)$$

where  $S_{Rs}$  is the positive root of the quadratic equation obtained from Eq. (8.44) and (8.45), consistently with the fact that the right shock moves from the left to the right.

### 8.2.4 Exact Riemann Solver

Having derived relations between primitive state variables  $\mathbf{W}_L$ ,  $\mathbf{W}_R$  and  $\mathbf{W}_*$  across the different wave patterns, we can derive an exact solution of

the RP for dark fluids as given by Eq. (8.13). The first step consists in determining the value of  $\Delta_*$  in the star region of Fig. 8.1. We have expressed the velocity  $v_*$  in terms of  $\Delta_*$  and the known states  $\mathbf{W}_L$ ,  $\mathbf{W}_R$  for all possible wave patterns. Thus, equating these relations for the left and right waves,  $\Delta_*$  is the root of the algebraic equation

$$f_L(\Delta_*, \mathbf{W}_L) - f_R(\Delta_*, \mathbf{W}_R) = 0, \quad (8.48)$$

where

$$f_L(\Delta, \mathbf{W}_L) = \begin{cases} f_{Ls}(\Delta, \mathbf{W}_L) & \text{if } \Delta > \Delta_L \text{ (shock)} \\ f_{Lr}(\Delta, \mathbf{W}_L) & \text{if } \Delta \leq \Delta_L \text{ (rarefaction)} \end{cases} \quad (8.49)$$

with  $f_{Ls}(\Delta, \mathbf{W}_L)$  and  $f_{Lr}(\Delta, \mathbf{W}_L)$  given by Eq. (8.43) and Eq. (8.31) respectively, while

$$f_R(\Delta, \mathbf{W}_R) = \begin{cases} f_{Rs}(\Delta, \mathbf{W}_R) & \text{if } \Delta > \Delta_R \text{ (shock)} \\ f_{Rr}(\Delta, \mathbf{W}_R) & \text{if } \Delta \leq \Delta_R \text{ (rarefaction)} \end{cases} \quad (8.50)$$

with  $f_{Rs}(\Delta, \mathbf{W}_R)$  and  $f_{Rr}(\Delta, \mathbf{W}_R)$  given by Eq. (8.47) and Eq. (8.36) respectively. Eq. (8.48) can be solved for  $\Delta_*$  to the desired level of accuracy using standard numerical root-finder schemes. Solving for  $\Delta_*$  completely determines the nature of the waves, then the value of  $v_*$  can be computed from one of the functions  $f_L(\Delta_*, \mathbf{W}_L)$  or  $f_R(\Delta_*, \mathbf{W}_R)$ . Once the state  $\mathbf{W}_*$  is known, the solution of the Riemann problem across the entire spatial interval can be sampled at any given time as follows:

- in the region to the left of the discontinuity corresponding to  $x - x_0 < v_*\tau$ :
  - if  $\Delta_L > \Delta_*$  the left wave is a rarefaction, then

$$\mathbf{W}(x, \tau) = \begin{cases} (\Delta_L, v_L) & \text{if } x - x_0 < S_{HLr}\tau \\ (\Delta_{Lfan}, v_{Lfan}) & \text{if } S_{HLr}\tau < x - x_0 < S_{TLr}\tau \\ (\Delta_*, v_*) & \text{if } x - x_0 > S_{TLr}\tau \end{cases} \quad (8.51)$$

where  $v_{Lfan}$  is given by solving Eq. (8.32) and  $\Delta_{Lfan}$  is given by Eq. (8.33).

- if  $\Delta_L < \Delta_*$  the left wave is a shock, then

$$\mathbf{W}(x, \tau) = \begin{cases} (\Delta_L, v_L) & \text{if } x - x_0 < S_{Ls}\tau \\ (\Delta_*, v_*) & \text{if } x - x_0 > S_{Ls}\tau \end{cases} \quad (8.52)$$

where  $S_{Ls}$  is given by Eq. (8.42).

Test	$\Delta_L$	$v_L$	$\Delta_R$	$v_R$
1	1.0	0.0	0.125	0.0
2	1.0	-0.0003	1.0	0.0003
3	0.3	0.0001	0.3	-0.0001

**Table 8.1:** Initial data for three test problems with exact solution.

- in the region to the right of the discontinuity corresponding to  $x - x_0 > v_*\tau$ :
  - if  $\Delta_R > \Delta_*$  the right wave is a rarefaction, then

$$\mathbf{W}(x, \tau) = \begin{cases} (\Delta_*, v_*) & \text{if } x - x_0 < S_{\text{TRr}}\tau \\ (\Delta_{\text{Rfan}}, v_{\text{Rfan}}) & \text{if } S_{\text{TRr}}\tau < x - x_0 < S_{\text{HRr}}\tau \\ (\Delta_R, v_R) & \text{if } x - x_0 > S_{\text{HRr}}\tau \end{cases} \quad (8.53)$$

where  $v_{\text{Rfan}}$  is given by solving Eq. (8.37) and  $\Delta_{\text{Rfan}}$  is given by Eq. (8.38).

- if  $\Delta_R < \Delta_*$  the right wave is a shock, then

$$\mathbf{W}(x, \tau) = \begin{cases} (\Delta_*, v_*) & \text{if } x - x_0 < S_{\text{Rs}}\tau \\ (\Delta_R, v_R) & \text{if } x - x_0 > S_{\text{Rs}}\tau \end{cases} \quad (8.54)$$

where  $S_{\text{Rs}}$  is given by Eq. (8.46).

We construct an exact Riemann solver as in [171]. We first solve Eq. (8.48) using the Newton-Raphson method. The value of  $\Delta_*$  is obtained to a given level of accuracy  $\epsilon$  through an iteration procedure

$$\Delta_{(i)}^* = \Delta_{(i-1)}^* - \frac{f[\Delta_{(i-1)}^*]}{f'[\Delta_{(i-1)}^*]}, \quad (8.55)$$

where  $f(\Delta^*) = f_L(\Delta_*, \mathbf{W}_L) - f_R(\Delta_*, \mathbf{W}_R)$  and  $f'(\Delta^*) = df/d\Delta|_*$  (the derivatives can be computed analytically). The iteration continues until the desired accuracy is reached

$$\frac{|\Delta_{(i)}^* - \Delta_{(i-1)}^*|}{|\Delta_{(i)}^* + \Delta_{(i-1)}^*|} < \frac{\epsilon}{2}. \quad (8.56)$$

An initial guess value is necessary to start the iteration. Thus, the computation of the solution requires several iterations if the initial guess is too far off the solution. To address this point we use an adaptive scheme to optimise the initial guess using approximate Riemann solvers described in §8.2.5.

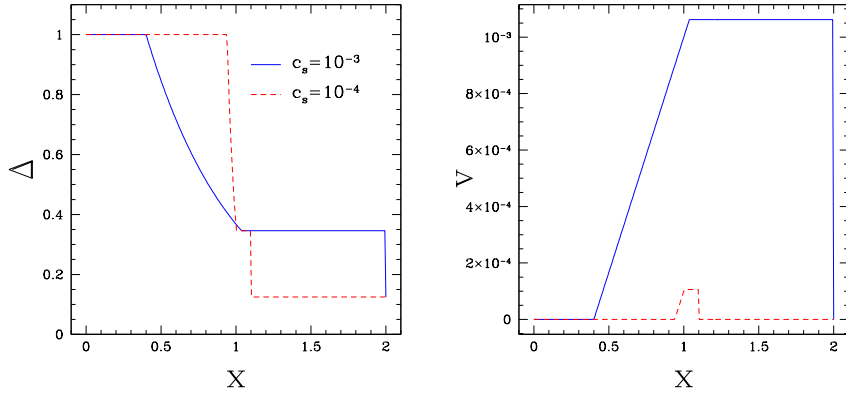


**Figure 8.2:** Exact solution of Test 1 for  $\Delta$  (left panel) and  $v$  (right panel) at time  $\tau = 600$  units for  $c_s = 10^{-3}$  (solid blue line) and  $10^{-4}$  (dot red line) respectively.

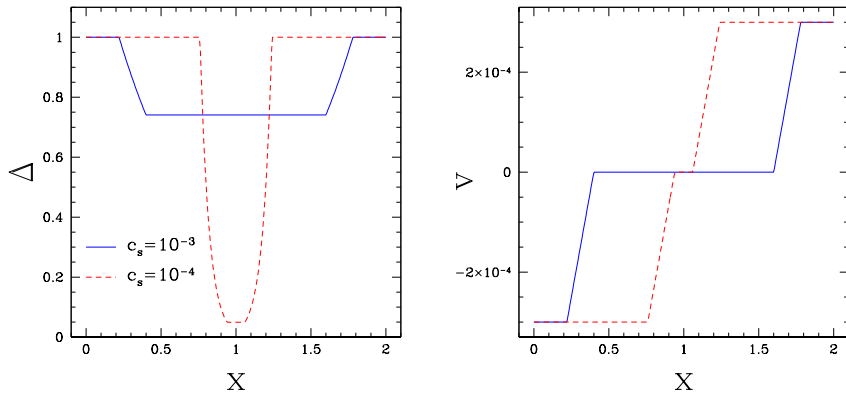


**Figure 8.3:** As in Fig. 8.2 for Test 2.

In Table 8.1 we quote the initial data for three standard test cases of the RP. Test 1 is the standard Sod test [156], the solution consists of a left rarefaction and a right shock. Test 2 has a solution consisting of two rarefaction waves, while Test 3 consists of two colliding shocks. We consider two different values of the speed of sound corresponding to  $c_s = 10^{-3}$  and  $10^{-4}$  respectively. We set the initial discontinuity at  $x_0 = 1$  and sample the solution in the interval  $0 < x < 2$  at time  $\tau = 600$ . We set the accuracy of the Newton-Raphson method to  $\epsilon = 10^{-6}$ .

The exact solutions to Tests 1, 2 and 3 are shown in Fig. 8.2, 8.3 and 8.4 respectively. In the case of Test 1 we can clearly see the opening of the rarefaction fan moving from right to left and the shock wave propagating

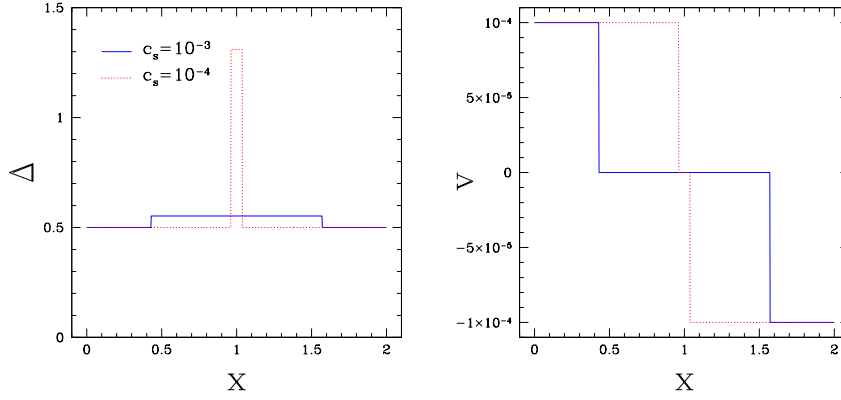


**Figure 8.4:** As in Fig. 8.2 for Test 3.

to the right. For Test 2 we notice the opening of the two rarefaction fans propagating to the left and to the right respectively, while in the case of Test 3 we can see the density and velocity profile of the colliding shock waves.

## 8.2.5 Approximate Riemann Solvers

### Primitive Variables Riemann Solver

Let us consider the characteristic equations of the primitive variable advection equation Eq. (8.16) given by  $\vec{L}_\pm \cdot d\vec{W} = 0$  where  $\vec{L}_\pm$  are the left eigenvectors, Eq. (8.22), and  $d\vec{W} = (d\Delta, dv)$ . We have

$$d\Delta + \frac{1 + c_s^2}{c_s^2} \frac{\Delta dv}{\sqrt{1 - v^2 + vc_s}} = 0 \quad \text{along } dx/d\tau = \lambda_+ \quad (8.57)$$

$$d\Delta - \frac{1 + c_s^2}{c_s^2} \frac{\Delta dv}{\sqrt{1 - v^2 - vc_s}} = 0 \quad \text{along } dx/d\tau = \lambda_-, \quad (8.58)$$

and let us introduce the variables

$$C^+ = \frac{1 + c_s^2}{c_s^2} \frac{\Delta}{\sqrt{1 - v^2 + vc_s}}, \quad (8.59)$$

$$C^- = \frac{1 + c_s^2}{c_s^2} \frac{\Delta}{\sqrt{1 - v^2 - vc_s}}, \quad (8.60)$$

following the derivation presented in [171], we connect the star state to the left state by integrating Eq. (8.57) along the characteristic of speed  $\lambda_+$  where  $C_+$  is evaluated at the foot of the characteristic, this gives:

$$\Delta_L - \Delta_* = -C_L^+ v_L + C_L^+ v_*. \quad (8.61)$$

Similarly, we connect the star region to the right state by integrating Eq. (8.58) along the characteristic with speed  $\lambda_+$  with  $C_-$  is evaluated at the foot of the characteristics, we have

$$\Delta_* - \Delta_R = C_R^- v_* - C_R^- v_R, \quad (8.62)$$

solving the linear system of Eq. (8.61) and (8.62) we finally obtain the approximate state variables in the star region

$$v_* = \frac{1}{C_L^+ + C_R^+} [C_L^+ v_L + C_R^- v_R + (\Delta_L - \Delta_R)], \quad (8.63)$$

$$\Delta_* = \frac{1}{C_L^+ + C_R^+} [C_L^+ \Delta_R + C_R^- \Delta_L + C_L^+ C_R^- (v_L - v_R)]. \quad (8.64)$$

### Two Rarefactions Riemann Solver

This solver computes the primitive variables in the star region assuming it is comprised between two rarefaction waves. Thus, from Eq. (8.30) and Eq. (8.35) we have

$$g_{Lr}(v_*) - g_{Rr}(v_*) = \ln \Delta_L - \ln \Delta_R + g_{Lr}(v_L) - g_{Rr}(v_R), \quad (8.65)$$

this algebraic equation can be solved numerically to obtain  $v_*$ , then substituting in Eq. (8.30) or Eq. (8.35) one obtain the value of  $\Delta_*$ .

### Two Shocks Riemann Solver

This solver computes the primitive variables in the star region assuming it is comprised between two shock waves. Thus, equating Eq. (8.43) and Eq. (8.47) we obtain an algebraic equation that can be solved numerically to obtain  $\Delta_*$ , which substituted back into Eq. (8.43) or Eq. (8.47) allows us to obtain the value of  $v_*$ .

## 8.2.6 Specificities of the Riemann Problem for Dark Fluids

The wave structure of the Riemann problem for dark fluids resemble that of an isothermal gas. Nonetheless, there are aspects that have no equivalent in standard gas dynamics and which are worth to clarify better. First, we should remind that in the dark fluid case what is behaving as an isothermal system are the dark density and pressure perturbations and not the dark fluid as whole. Hence, while in gas dynamics the density variable  $\rho$  is strictly

positive, the auxiliary density variable  $\Delta = 1 + w + (1 + c_s^2)\delta$  is not, as for a given set of DE model parameters the sign depends on the amplitude of the density perturbation. More specifically, we have that  $\Delta$  is strictly positive in regions where  $\delta > -(1 + w)/(1 + c_s^2)$ , while it is strictly negative in the opposite case. However, the advection part of Eq. (8.9) and (8.10) is invariant under sign transformation,  $\Delta \rightarrow -\Delta$ , thus implying that the structure of the Riemann problem remains the same independently of the sign of  $\Delta$ . On the other hand, the case  $\Delta = 0$  deserves a separate discussion.

In gas dynamics  $\rho = 0$  represents the vacuum state and the structure of the solution of the RP differs from the conventional one. As shown in [171] shock waves cannot propagate in a region adjacent to vacuum, while the only admissible discontinuous solutions are rarefaction and contact waves. This is not the case for dark fluids as no wave may propagate adjacent to  $\Delta = 0$ . On the one hand generalised Riemann invariants are ill defined, on the other hand shocks are no solution of the system. This can be understood by noticing that differently from gas dynamics  $\Delta = 0$  does not represent a vacuum state, rather a region where the density fluctuation is determined by the background homogeneous dark fluid density,  $\delta\rho = -(1 + w)/(1 + c_s^2)\bar{\rho}$ . We may construct a solution of the system in  $\Delta = 0$  regions which are adjacent to “non-vacuum” cells, by considering the advection part of the Euler equations in terms of  $\delta$  and  $\vec{v}$ . These read as:

$$\frac{\partial\delta}{\partial\tau} = 0, \quad \frac{\partial\vec{v}}{\partial\tau} + (\vec{v} \cdot \vec{\nabla})\vec{v} = 0,$$

where we can see that  $\delta = \text{const.}$  and  $\vec{v} = \text{const.}$  is a solution of the system. The constant values can be determined in terms of the boundary cell values, thus corresponding to a constant displacement in the cell with  $\Delta = 0$  of the density fluctuation and velocity of adjacent cells.

### 8.3 Wave structure in 3D

In the previous section we have discussed the Riemann problem in 1D. As we will show here this provides the base results to solve the Riemann problem in 3D. In fact, let us consider Eq. (8.9) and Eq. (8.10) without source terms in Cartesian coordinates. In terms of the conservative variables these can be written in a state-vector form:

$$\mathbf{U} + \mathbf{A}(\mathbf{U})\mathbf{U}_x + \mathbf{B}(\mathbf{U})\mathbf{U}_y + \mathbf{C}(\mathbf{U})\mathbf{U}_z = 0, \quad (8.66)$$

with  $\mathbf{U} = (\Delta, \Delta u, \Delta v, \Delta w)$  where  $u, v$  and  $w$  are the components of the peculiar velocity vector along  $x, y$  and  $z$  respectively, and

$$\mathbf{A}(\mathbf{U}) = \begin{bmatrix} 0 & 1 + c_s^2 & 0 & 0 \\ \frac{c_s^2}{1+c_s^2} - u^2 & 2u & 0 & 0 \\ -uv & v & u & 0 \\ -uw & w & 0 & u \end{bmatrix}, \quad \mathbf{B}(\mathbf{U}) = \begin{bmatrix} 0 & 0 & 1 + c_s^2 & 0 \\ -uv & v & u & 0 \\ \frac{c_s^2}{1+c_s^2} - v^2 & 0 & 2v & 0 \\ -vw & 0 & w & v \end{bmatrix},$$

$$\mathbf{C}(\mathbf{U}) = \begin{bmatrix} 0 & 0 & 0 & 1 + c_s^2 \\ -uw & w & 0 & u \\ -vw & 0 & w & v \\ \frac{c_s^2}{1+c_s^2} - w^2 & 0 & 0 & 2w \end{bmatrix}.$$

The eigenvalues of these matrices are  $\lambda_1 = s - c_s \sqrt{1 - s^2}$ ,  $\lambda_2 = s + c_s \sqrt{1 - s^2}$  and  $\lambda_{3,4} = s$  with  $s = u, v$  and  $w$  for  $\mathbf{A}$ ,  $\mathbf{B}$  and  $\mathbf{C}$  respectively. Hence, the 3D case can be seen as the composition of three advections with the same structure of the Riemann problem.

Let us consider the advection equations along the  $x$ -direction. The eigenvalues of  $\mathbf{A}$  are  $\lambda_{1,2} = u \pm c_s \sqrt{1 - u^2}$  and  $\lambda_{3,4} = u$ , the corresponding eigenvectors read as

$$\mathbf{R}_1 = \begin{bmatrix} 1 + c_s^2 \\ u - c_s \sqrt{1 - u^2} \\ \left(1 + \frac{uc_s}{\sqrt{1 - u^2}}\right) v \\ \left(1 + \frac{uc_s}{\sqrt{1 - u^2}}\right) w \end{bmatrix}, \quad \mathbf{R}_2 = \begin{bmatrix} 1 + c_s^2 \\ u + c_s \sqrt{1 - u^2} \\ \left(1 - \frac{uc_s}{\sqrt{1 - u^2}}\right) v \\ \left(1 - \frac{uc_s}{\sqrt{1 - u^2}}\right) w \end{bmatrix}, \quad \mathbf{R}_3 = \begin{bmatrix} 0 \\ 0 \\ 1 \\ 0 \end{bmatrix}, \quad \mathbf{R}_4 = \begin{bmatrix} 0 \\ 0 \\ 0 \\ 1 \end{bmatrix}. \quad (8.67)$$

The eigenvalues  $\lambda_{1,2}$  are real and distinct and associated to the genuinely non-linear characteristic fields which correspond to the shock and rarefaction waves discussed in Section 8.2. Using the components of  $\mathbf{R}_1$  and  $\mathbf{R}_2$ , it can be shown after some cumbersome algebra that the Riemann Invariants relating  $\Delta$  and  $u$  are identical to those derived in the 1D case, Eqs. (8.27) and (8.28). Similarly, one can also show that the Rankine-Hugoniot conditions relating  $\Delta$  and  $u$  are independent of the tangential velocities ( $v$  and  $w$ ) and identical to those derived in the 1D case. In the case of the tangential velocities the Riemann invariants are given by:

$$\frac{c_s}{1 + c_s^2} \frac{u}{\sqrt{1 - u^2}} \ln \Delta - \ln s = \text{const.} \quad (\lambda = \lambda_1) \quad (8.68)$$

$$\frac{c_s}{1 + c_s^2} \frac{u}{\sqrt{1 - u^2}} \ln \Delta + \ln s = \text{const.} \quad (\lambda = \lambda_2) \quad (8.69)$$

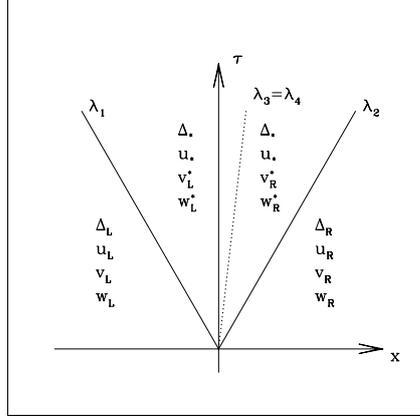


**Figure 8.5:** Structure of the solution of 3D Riemann problem along a given spatial dimension.

where  $s = v, w$ . The main difference with respect to the 1D case is the presence of additional waves associated to the degenerate eigenvalues  $\lambda_{3,4} = u$ . From the Boillat's theorem [29] the multiplicity 2 of these degenerate eigenvalues implies that they are linearly degenerate fields corresponding to contact discontinuities. From the components of right eigenvectors  $\mathbf{R}_3$  and  $\mathbf{R}_4$ , it can be immediately inferred that  $\Delta$  and  $u$  remain constant across the contact discontinuity, only the tangential velocities vary, thus corresponding to shear waves.

This provides us with all the information to draw the solution of the 3D Riemann problem along a given spatial direction as shown in Fig. 8.5. We can see that once the 1D Riemann problem is solved for  $\Delta$  and  $u$ , then the values of the tangential velocities in the star region to the left and right of the contact discontinuity can be easily determined using the Riemann Invariants and the Rankine-Hugoniot conditions depending on the nature of the  $\lambda_{1,2}$ -fields:

- if  $\lambda_1$  is associated to a left-rarefaction, then

$$s_L^* = s_L \exp \left[ \frac{c_s}{1 + c_s^2} \left( \frac{u_*}{\sqrt{1 - u_*^2}} \ln \Delta_* - \frac{u_L}{\sqrt{1 - u_L^2}} \ln \Delta_L \right) \right], \quad (8.70)$$

- if  $\lambda_1$  is associated to a left-shock, then

$$s_L^* = \frac{s_L \Delta_L (u_L - S_L)}{\Delta_* (u_* - S_L)}, \quad (8.71)$$

- if  $\lambda_2$  is associated to a right-rarefaction, then

$$s_R^* = s_R \exp \left[ \frac{c_s}{1 + c_s^2} \left( \frac{u_R}{\sqrt{1 - u_R^2}} \ln \Delta_R - \frac{u_*}{\sqrt{1 - u_*^2}} \ln \Delta_* \right) \right], \quad (8.72)$$

- if  $\lambda_2$  is associated to a right-shock, then

$$s_R^* = \frac{s_R \Delta_R (u_R - S_R)}{\Delta_* (u_* - S_R)}, \quad (8.73)$$

where  $s = v, w$  and  $S_{L,R}$  are the left and right shock speed respectively.

## 8.4 Upwind Numerical Schemes

### 8.4.1 Conservative Hyperbolic Methods

Let us consider the problem of solving numerically the 1D advection problem, Eq. (8.11), provided with a set of initial conditions and boundary conditions. The first step consists in discretising the time interval into a finite number of time-steps  $\Delta\tau$  and the spatial domain in a finite number of cells  $I_i = [x_{i-\frac{1}{2}}, x_{i+\frac{1}{2}}]$  with  $i = 1, \dots, M$  of size  $\Delta x = L/M$  (finite volume approach), where  $L$  is the size of the spatial domain of integration. A numerical solution of Eq. (8.11) can be obtained by splitting the system into a purely advection problem with  $\mathbf{U}_\tau + \mathbf{F}(\mathbf{U})_x = 0$  and an ordinary differential equation  $\mathbf{U}_\tau = \mathbf{S}(\mathbf{U})$ . The numerical solution to the advection problem can be obtained using a finite volume scheme:

$$\tilde{\mathbf{U}}_i^{n+1} = \mathbf{U}_i^n + \frac{\Delta\tau}{\Delta x} \left[ \mathbf{F}_{i-\frac{1}{2}} - \mathbf{F}_{i+\frac{1}{2}} \right], \quad (8.74)$$

where the  $\mathbf{F}_{i\pm\frac{1}{2}}$  are intercell fluxes at the boundaries of the  $i$ -th cell. The splitting method has to match the order of the solver used for the advection problem: at first order the source step can be numerically solved using a simple Euler method, e.g.

$$\mathbf{U}_i^{n+1} = \tilde{\mathbf{U}}_i^{n+1} + \Delta\tau \mathbf{S}(\tilde{\mathbf{U}}_i^{n+1}), \quad (8.75)$$

while at second order we can use Strang splitting [159], where the source step is performed for half a time step before the advection problem and half afterwards. Godunov methods, also known as upwind schemes, compute the flux as  $\mathbf{F}_{i\pm\frac{1}{2}} = \mathbf{F}[\mathbf{U}_{i\pm 1/2}(0)]$  where  $\mathbf{U}_{i\pm 1/2}(0)$  is the solution of the Riemann problem at each inter-cell boundary. Alternative to upwind methods are the

so called centred schemes that directly use approximated expressions of the intercell fluxes also derived from solutions of the Riemann problem at hand. Upwind methods differ on how boundary states to the left and right of the intercell location are evaluated to provide the initial data of the Riemann problem. The original method introduced by Godunov [75] computes the intercell fluxes at  $\mathbf{U}_{i\pm 1/2}^n(0)$ , that is the solution of the Riemann problem with initial data given by a constant distribution of the state variables  $\mathbf{U}_i^n$  and  $\mathbf{U}_{i+1}^n$  in contiguous cells. For this reason this scheme is also known as “piecewise constant method”, however this is only first-order accurate and consequently higher-order scheme are used for any real application.

Here, we will derive working examples of the Monotonic Upstream Centred Scheme for Conservation Laws (MUSCL-Hancock), the Piecewise Linear Method (PLM) and the Piecewise Parabolic Methods (PPM) with characteristic tracing steps for the advection equation of cosmic dark fluids. Before describing these schemes in the following we specify the Riemann solver, the choice of the integration time-step and the boundary conditions which are used hereafter.

### Approximate Riemann Solver

In the case of upwind schemes the Riemann problem can be solved using an exact solver as the one described in Section 8.2.4. However, for any practical application such as cosmological simulations, this is computationally too expensive, since it requires to iteratively solve algebraic equations at each cell of the spatial domain of integration. For this reason, approximate solvers are used instead of exact solvers. Here, we use the Primitive Variables Riemann Solver (PVRS) described in §8.2.5.

It is worth noticing that in the case of dark fluids, sampling the similarity solution of the Riemann problem at  $x/\tau = 0$  may require additional computations for rarefaction waves. This is because the fluid velocity inside the fan region is also given in the form of an algebraic equation, Eq. (8.32) for left rarefactions and Eq. (8.37) for right ones. To avoid these expensive iterative computations we use a weighted average estimate of the fluid velocity inside the fan region. More specifically, defining  $f_{Lr} \equiv S_{HLr}/(S_{HLr} - S_{TLr})$  and  $f_{Rr} \equiv S_{HRr}/(S_{HRr} - S_{TRr})$  we estimate the velocities in the fan as

$$v_{Lfan} = f_{Lr}v_* + (1 - f_{Lr})v_L, \quad (8.76)$$

$$v_{Rfan} = f_{Rr}v_* + (1 - f_{Rr})v_R. \quad (8.77)$$

### Courant Condition

The time-step  $\Delta\tau$  in Eq. (8.74) satisfies the condition  $\Delta\tau \leq \Delta x/S_{\max}^n$  where  $S_{\max}^n$  is the maximum wave velocity at  $\tau^n$  in the spatial domain of integration. This condition ensures that no waves in the solution of the Riemann problem travels more than the size of the cell  $\Delta x$  in the time interval  $\Delta\tau$ . A time-step satisfying the above condition can be set by introducing the Courant-Friedrichs-Lewy (CFL) coefficient  $C_{\text{cff}}$ , such that

$$\Delta\tau = C_{\text{cff}} \frac{\Delta x}{S_{\max}^n}, \quad (8.78)$$

with  $0 < C_{\text{cff}} \leq 1$ . Hereafter, we set  $C_{\text{cff}} = 0.9$  and estimate the maximum wave velocity as

$$S_{\max}^n = \max_i \{|v_i^n| + c_s\}, \quad (8.79)$$

which provides a very good approximation in the case of rarefaction waves, though it may underestimate the speed of propagation in the case of shocks.

### Transmissive Boundary Conditions

We test the numerical schemes for the test problems given in Table (8.1) assuming transmissive boundary conditions:

$$\Delta_{M+1}^n = \Delta_M^n, \quad v_{M+1}^n = v_M^n. \quad (8.80)$$

In such a case the boundaries do not affect the propagation of waves.

## 8.4.2 MUSCL-Hancock Method

As already mentioned, the original Godunov's scheme which is based on a piecewise constant distribution of data is only first-order accurate. Nevertheless, as shown by Godunov's theorem first-order schemes are guaranteed to preserve the monotonicity of the solution which is not the case of higher-order methods. In a series of seminal papers [173, 174, 175, 176, 177] Van Leer presented a modification to the piecewise constant data to achieve higher-order accuracy while restraining the scheme to satisfy monotonicity constraints. The idea is to use the initial piecewise constant data distribution to reconstruct data inside cells and extrapolate the values of the state variables at the cell interfaces. Then, using the conservation equations these boundary values are evolved by half-time step to achieve second-order accuracy in time. It is these reconstructed values that provide the initial data for the Riemann problem at the cell interface. However, the data reconstruction inside cells

may generate local extrema that lead to spurious numerical oscillations in the solution, thus we impose monotonicity constraints on the reconstruction.

The MUSCL-Hancock method introduced by Van Leer<sup>2</sup> in [178] is based of a linear reconstruction of the data distribution inside cells. The reconstruction consists of the following steps:

- Starting with the initial piecewise constant data  $\mathbf{U}_i^n$ , the left and right cell boundary value are linearly extrapolated as

$$\mathbf{U}_{i,L}^n = \mathbf{U}_i^n - \frac{1}{2}\partial\mathbf{U}_i, \quad \mathbf{U}_{i,R}^n = \mathbf{U}_i^n + \frac{1}{2}\partial\mathbf{U}_i, \quad (8.81)$$

where  $\partial\mathbf{U}_i$  denotes the slope of the linear interpolation in the  $i$ -th cell.

- Evolve  $\mathbf{U}_{i,L}^n$  and  $\mathbf{U}_{i,R}^n$  by a time  $\Delta t/2$  according to

$$\bar{U}_{i,L}^{n+1/2} = \mathbf{U}_{i,L}^n + \frac{1}{2} \frac{\Delta\tau}{\Delta x} [\mathbf{F}(\mathbf{U}_{i,L}^n) - \mathbf{F}(\mathbf{U}_{i,R}^n)], \quad (8.82)$$

$$\bar{U}_{i,R}^{n+1/2} = \mathbf{U}_{i,R}^n + \frac{1}{2} \frac{\Delta\tau}{\Delta x} [\mathbf{F}(\mathbf{U}_{i,L}^n) - \mathbf{F}(\mathbf{U}_{i,R}^n)], \quad (8.83)$$

- Solve the Riemann Problem at intercell location with piecewise constant data  $\bar{U}_{i,L}^{n+1/2}$  and  $\bar{U}_{i,R}^{n+1/2}$ :

$$\mathbf{U}_\tau + \mathbf{F}(\mathbf{U})_x = 0, \quad (8.84)$$

with initial conditions

$$\mathbf{U}(x, 0) = \begin{cases} \bar{U}_{i,L}^{n+1/2} & \text{if } x < 0 \\ \bar{U}_{i+1,R}^{n+1/2} & \text{if } x > 0 \end{cases} \quad (8.85)$$

A key point concerns the evaluation of the slopes  $\partial\mathbf{U}_i$ , which must satisfy monotonicity constraints. We implement the MUSCL-Hancock scheme with the MINMAX slope limiter which reads as:

$$\partial\mathbf{U}_i = \frac{1}{2} [\text{sign}(\mathbf{U}_i^n - \mathbf{U}_{i-1}^n) + \text{sign}(\mathbf{U}_{i+1}^n - \mathbf{U}_i^n)] \times \min(|\mathbf{U}_i^n - \mathbf{U}_{i-1}^n|, |\mathbf{U}_{i+1}^n - \mathbf{U}_i^n|). \quad (8.86)$$

In Fig. 8.6, 8.7 and 8.8 we plot the numerical solutions (dotted lines) to test cases given in Table 8.1 obtained with the MUSCL-Hancock method

---

<sup>2</sup>In [178] the idea behind this scheme is attributed to S. Hancock, see also [179], from which the acronym of MUSCL-Hancock method.

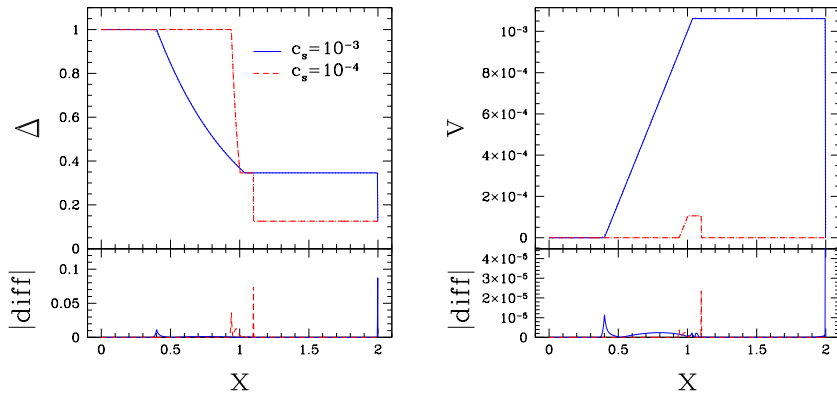


**Figure 8.6:** MUSCL-Hancock (dotted lines) vs. Exact solution of Test 1 for  $\Delta$  (left panel) and  $v$  (right panel) at time  $\tau = 600$  units for  $c_s = 10^{-3}$  (blue lines) and  $10^{-4}$  (red lines) respectively. In the bottom panels it is shown the absolute difference between the numerical and exact solution.

against the exact solutions at  $\tau = 600$  units for  $c_s = 10^{-3}$  (solid blue lines) and  $c_s = 10^{-4}$  (dashed red lines) respectively. In the bottom panels we plot the absolute value of the difference between the numerical and exact solutions.

Overall the scheme perform rather well. A zoom on the value of  $\Delta$  near the shocks in Fig. 8.6 and 8.8 reveals that shock waves are spread over  $\sim 3$  cells, rather than having the zero-width of the exact solution. On the other hand, the speed is correctly estimated as can be seen on the right panels, thus indicating that the average shock position is well determined by the numerical scheme. Another characteristic feature of the solutions of Test 1 and 3 near the shocks is the absence of spurious oscillations. In the case of rarefaction waves, larger errors occur near the head and the tail as can be seen from Fig. 8.6 and 8.7 and discontinuities are spread over  $\sim 10$  cells. We have checked that the numerical solution converges to the exact by increasing the spatial resolution of the grid.

### 8.4.3 Piecewise Linear Method (PLM)

This scheme introduced by Colella [40] builds upon the MUSCL method and uses a linear reconstruction of the data. We will follow the implementation presented in the lecture notes by M. Zingale [190] to which we refer the reader for a clear summary of higher-order reconstruction methods of non-linear advection equations.

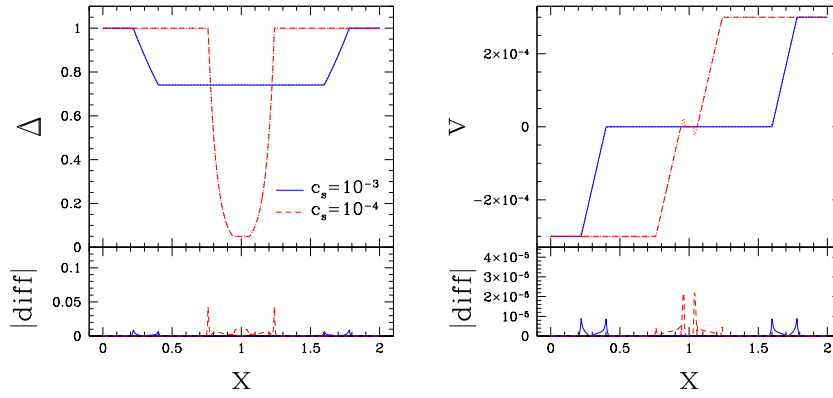


Figure 8.7: As in Fig. 8.6 for Test 2.

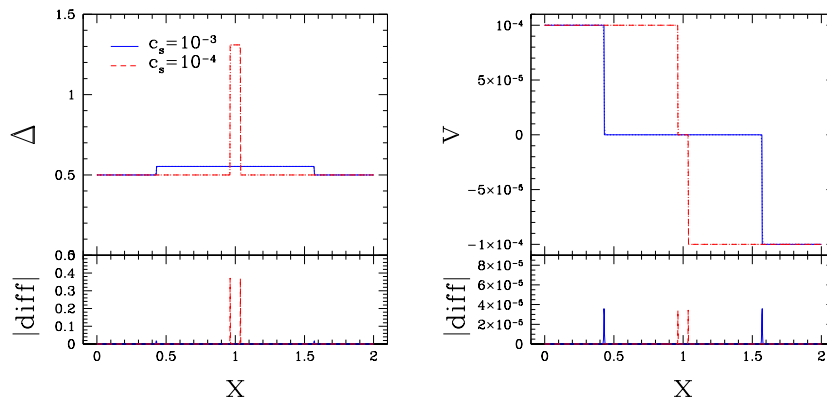


Figure 8.8: As in Fig. 8.6 for Test 3.

The basic idea is to obtain left and right intercell states as a Taylor expansion of the primitive variables to first-order in  $\Delta x/2$  to displace from the cell-centred value to the interface, and to first-order in  $\Delta\tau/2$  to evolve the states to mid-point in time. Then, the extrapolated left and right intercell boundary states are obtained by expliciting in the expansion the wave structure of the system and accounting only for waves that moves toward the cell interface, a constraint also known as *characteristic tracing*.

General formulae to construct these states are given in [190]. In the case of dark fluids, these reads as

$$\bar{\Delta}_{i,L}^{n+1/2} = \Delta_i^n + \frac{1}{2} [\tilde{\Delta}_i^- + \tilde{\Delta}_i^+] , \quad \bar{\Delta}_{i+1,R}^{n+1/2} = \Delta_{i+1}^n - \frac{1}{2} [\tilde{\Delta}_{i+1}^- + \tilde{\Delta}_{i+1}^+] , \quad (8.87)$$

with

$$\tilde{\Delta}_i^- = \begin{cases} \frac{1}{2} [1 - \frac{\Delta\tau}{\Delta x} \lambda_-(v_i)] \left[ \left(1 - \frac{v_i c_s}{\sqrt{1-v_i^2}}\right) \partial\Delta_i - \frac{1+c_s^2}{c_s \sqrt{1-v_i^2}} \Delta_i \partial v_i \right] & \text{if } \lambda_-(v_i) \geq 0 \\ 0 & \text{otherwise} \end{cases} \quad (8.88)$$

and

$$\tilde{\Delta}_i^+ = \begin{cases} \frac{1}{2} [1 - \frac{\Delta\tau}{\Delta x} \lambda_+(v_i)] \left[ \left(1 + \frac{v_i c_s}{\sqrt{1-v_i^2}}\right) \partial\Delta_i + \frac{1+c_s^2}{c_s \sqrt{1-v_i^2}} \Delta_i \partial v_i \right] & \text{if } \lambda_+(v_i) \geq 0 \\ 0 & \text{otherwise} \end{cases} \quad (8.89)$$

and for the velocity

$$\bar{v}_{i,L}^{n+1/2} = v_i^n + \frac{1}{2} [\tilde{v}_i^- + \tilde{v}_i^+] , \quad \bar{v}_{i+1,R}^{n+1/2} = v_{i+1}^n - \frac{1}{2} [\tilde{v}_{i+1}^- + \tilde{v}_{i+1}^+] , \quad (8.90)$$

with

$$\tilde{v}_i^- = \begin{cases} \frac{1}{2} [1 - \frac{\Delta\tau}{\Delta x} \lambda_-(v_i)] \left[ \left(1 - \frac{v_i^2 c_s^2}{1-v_i^2}\right) \frac{c_s \sqrt{1-v_i^2}}{\Delta_i(1+c_s^2)} \partial\Delta_i - \left(1 + \frac{c_s v_i}{\sqrt{1-v_i^2}}\right) \partial v_i \right] & \text{if } \lambda_-(v_i) \geq 0 \\ 0 & \text{otherwise} \end{cases} \quad (8.91)$$

and

$$\tilde{v}_i^+ = \begin{cases} \frac{1}{2} [1 - \frac{\Delta\tau}{\Delta x} \lambda_+(v_i)] \left[ \left(1 - \frac{v_i^2 c_s^2}{1-v_i^2}\right) \frac{c_s \sqrt{1-v_i^2}}{\Delta_i(1+c_s^2)} \partial\Delta_i + \left(1 - \frac{c_s v_i}{\sqrt{1-v_i^2}}\right) \partial v_i \right] & \text{if } \lambda_+(v_i) \geq 0 \\ 0 & \text{otherwise} \end{cases} \quad (8.92)$$

We compute the slope  $\partial W_i = \{\partial \Delta_i, \partial v_i\}$  using the SUPERBEE slope limiter:

$$\begin{aligned} \partial W_i &= [\text{sign}(\mathbf{W}_i^n - \mathbf{W}_{i-1}^n) + \text{sign}(\mathbf{W}_{i+1}^n - \mathbf{W}_i^n)] \times \\ &\times \min \left[ |\mathbf{W}_i^n - \mathbf{W}_{i-1}^n|, |\mathbf{W}_{i+1}^n - \mathbf{W}_i^n|, \frac{1}{2} \max (|\mathbf{W}_i^n - \mathbf{W}_{i-1}^n|, |\mathbf{W}_{i+1}^n - \mathbf{W}_i^n|) \right]. \end{aligned} \quad (8.93)$$

In Fig. 8.9, 8.10 and 8.11 we plot the PLM numerical solutions (dotted lines) to test cases given in Table 8.1 against the exact solutions at  $\tau = 600$  units for  $c_s = 10^{-3}$  (solid blue lines) and  $c_s = 10^{-4}$  (dashed red lines) respectively. In the bottom panels we plot the absolute value of the difference between the numerical and exact solutions. We can see only minor differences with the respect to the results obtained with the MUSCL-Hancock method shown in Fig. 8.6, 8.7 and 8.8. In particular we may notice that the former is less accurate than MUSCL-Hancock in resolving rarefaction waves, while it performs better in the case of shocks.

#### 8.4.4 Piecewise Parabolic Method (PPM)

Originally introduced by Colella & Woodward [41], these schemes achieve second-order accuracy using a parabolic reconstruction of the data with characteristic tracing. We refer again to Zingale's notes [190] for a clear summary of PPM in the case of non-linear advection equations. The expressions of the parabolic reconstruction of primitive variables with characteristics tracing step in the case of dark fluids are quite lengthy and here we only present the results of the numerical tests of Table 8.1 shown in Fig. 8.12, 8.13 and 8.14 (dotted lines) against the exact solutions at  $\tau = 600$  units for  $c_s = 10^{-3}$  (solid blue lines) and  $c_s = 10^{-4}$  (dashed red lines) respectively. In the bottom panels we plot the absolute value of difference between the exact and the numerical solutions. We can see the improvement of the PPM scheme compared to the PLM in resolving discontinuities.

## 8.5 Euler Equations in Supercomoving Variables

Cosmological simulation codes adopt super-comoving variables as defined in [109]. These reads as  $d\tilde{t} = (H_0/a)d\tau$  and  $d\tilde{x} = dx/L$ , where  $H_0$  is the Hubble parameter (in  $\text{km s}^{-1} \text{Mpc}^{-1}$ ) and  $L$  is the simulation box length (in Mpc). The convenience of these coordinates is that for a matter component with vanishing equation of state the Euler equations have the same form as in a

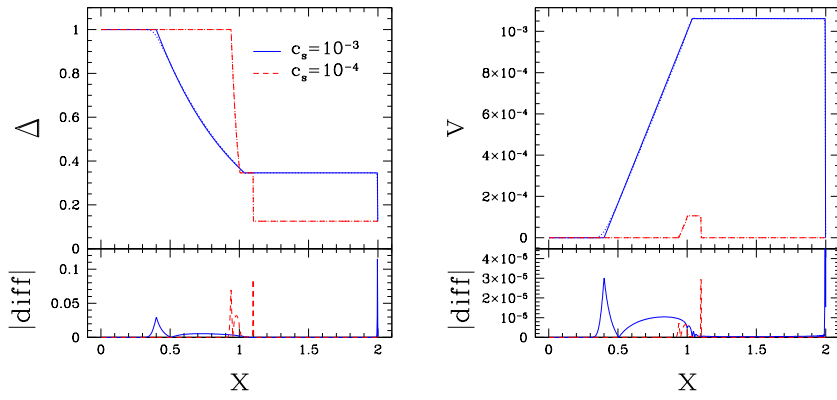


**Figure 8.9:** PLM (dotted lines) vs. Exact solution of Test 1 for  $\Delta$  (left panel) and  $v$  (right panel) at time  $\tau = 600$  units for  $c_s = 10^{-3}$  (blue lines) and  $10^{-4}$  (red lines) respectively. In the bottom panel the absolute difference between the numerical and exact solution.

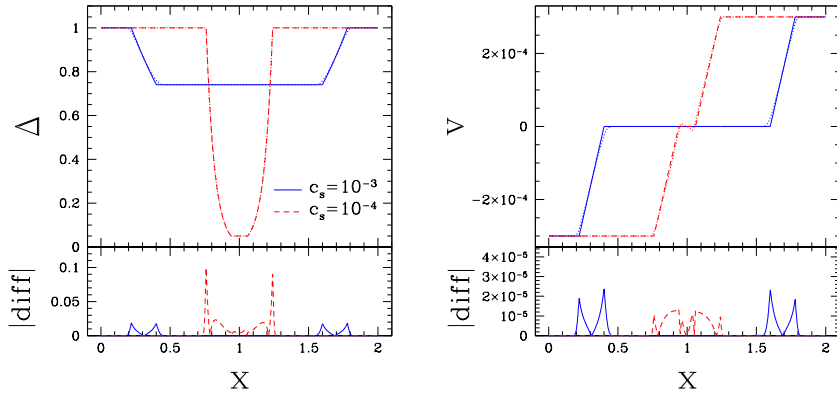


**Figure 8.10:** As in Fig. 8.9 for Test 2.

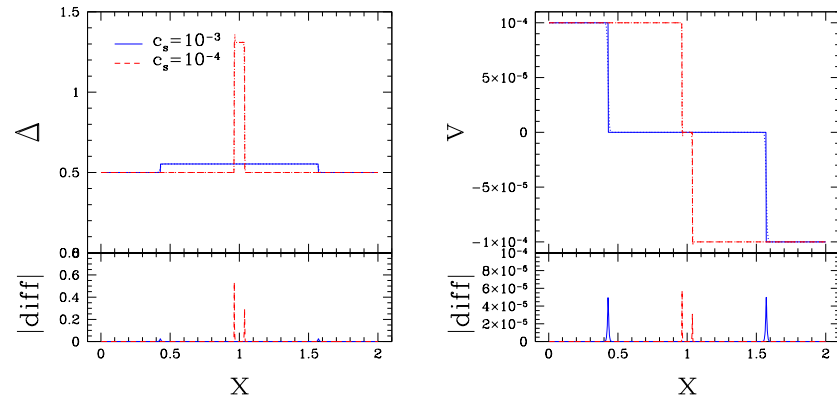


**Figure 8.11:** As in Fig. 8.9 for Test 3.

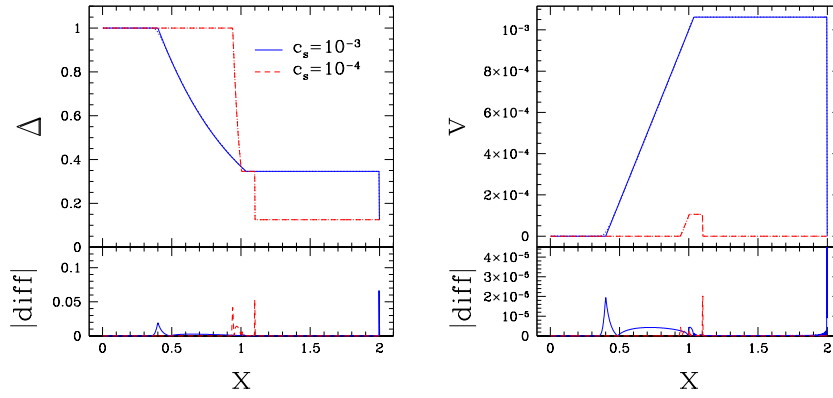


**Figure 8.12:** PPM (dotted lines) vs. Exact solution of Test 1 for  $\Delta$  (left panel) and  $v$  (right panel) at time  $\tau = 600$  units for  $c_s = 10^{-3}$  (blue lines) and  $10^{-4}$  (red lines) respectively. In the bottom panel the absolute difference between the numerical and exact solutions.

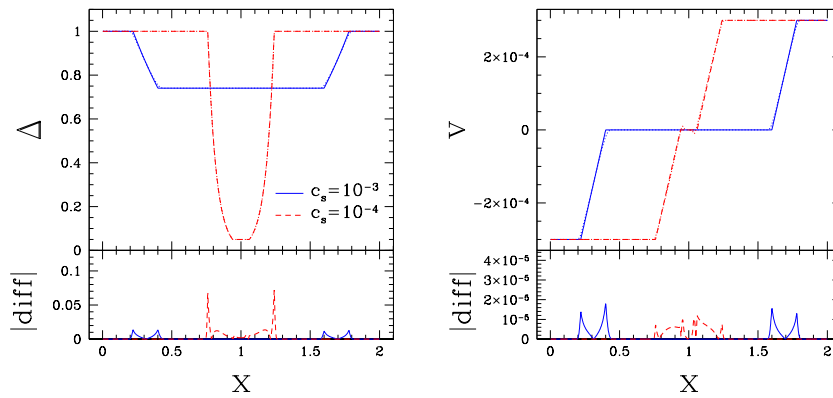


**Figure 8.13:** As in Fig. 8.12 for Test 2.

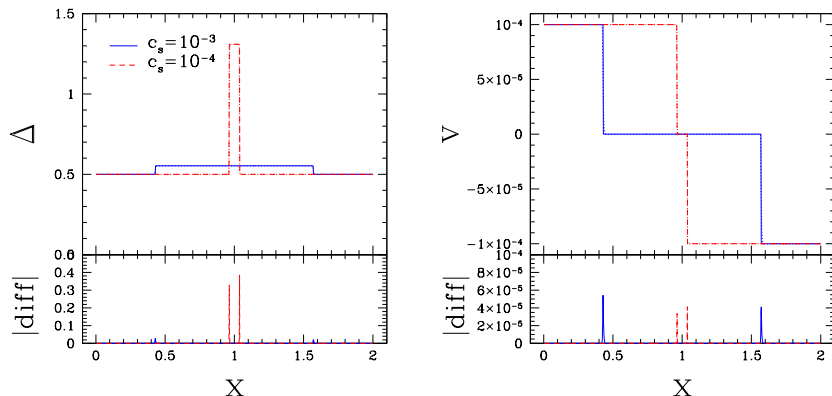


**Figure 8.14:** As in Fig. 8.12 for Test 3.

non-expanding universe. Because of the non-conservative nature of DE this is not the case of Eq. (8.9) and Eq. (8.10) which read as

$$\frac{\partial \Delta}{\partial \tilde{t}} + (1 + c_s^2) \frac{a}{H_0 L} \vec{\nabla} \cdot (\Delta \vec{v}) = 3a^2 E(a) [(1 + w)(c_s^2 - c_a^2) + (w - c_s^2) \Delta] \quad (8.94)$$

$$\frac{\partial (\Delta \vec{v})}{\partial \tilde{t}} + \frac{a}{H_0 L} \vec{\nabla} \cdot (\Delta \vec{v} \otimes \vec{v}) + \frac{c_s^2}{1 + c_s^2} \frac{a}{H_0 L} \vec{\nabla} \Delta = a^2 E(a) (3w - 1) \vec{v} - \frac{a}{H_0 L} \Delta \vec{\nabla} \Phi, \quad (8.95)$$

where  $E(a) = H(a)/H_0$  is the Hubble rate. It can be shown that the coordinate transformation does not alter the wave structure of the Riemann problem described in Section 8.2. In fact the in 1D Jacobian matrix  $\tilde{\mathbf{A}}$  associated with Eq. (8.94) and Eq. (8.95) can be written as  $a/(H_0 L) \mathbf{A}(\mathbf{U})$ , therefore the eigenvalues and eigenvectors are simply rescaled by a time-factor  $a/(H_0 L)$ . This also implies that the generalised Riemann invariants do not change with a rescaling of the time coordinate, while the speed of shocks from the Rankine-Hugoniot conditions is simply rescaled  $\tilde{S} = S/[a/(H_0 L)]$ .

## 8.6 Euler Equations in Spherical Symmetry

In order to test our 1D Godunov solvers in a realistic setting we want to compare the numerical solutions with analytical solutions of the spherical collapse problem. To this purpose we need to write the Euler equations Eq. (8.9) and Eq. (8.10) in spherical coordinates and assuming spherical

symmetry:

$$\frac{\partial \Delta}{\partial \tau} + 3\mathcal{H}(c_s^2 - w)(\Delta - 1 - w) + \frac{1 + c_s^2}{r^2} \frac{\partial}{\partial r} [r^2 \Delta v] = 0, \quad (8.96)$$

$$\frac{\partial \Delta \vec{v}}{\partial \tau} + \frac{1}{r^2} \frac{\partial}{\partial r} [r^2 \Delta \vec{v} \otimes \vec{v}] + \frac{c_s^2}{(1 + c_s^2)} \frac{\partial \Delta}{\partial r} = (3w - 1)\mathcal{H}\Delta v - \Delta \frac{\partial \Phi}{\partial r}. \quad (8.97)$$

After some algebra we get to the pseudo-conservative form:

$$\frac{\partial \Delta}{\partial \tau} + (1 + c_s^2) \frac{\partial \Delta v}{\partial r} = -2(1 + c_s^2) \frac{\Delta v}{r} - 3\mathcal{H}(c_s^2 - w)(\Delta - 1 - w), \quad (8.98)$$

$$\frac{\partial \Delta v}{\partial \tau} + \frac{\partial}{\partial r} \left[ \Delta v^2 + \frac{c_s^2}{(1 + c_s^2)} \Delta \right] = -2 \frac{\Delta v^2}{r} + (3w - 1)\mathcal{H}\Delta v - \Delta \frac{\partial \Phi}{\partial r}. \quad (8.99)$$

By comparing these equations to Eq. (8.9) and Eq. (8.10) we see that the only difference between the two systems are the geometrical source terms. This means that we can make use of the 1D Godunov methods in cartesian coordinates to solve the homogeneous equations and add the geometric sources with the splitting scheme described in §8.4.1. In order to close the equation system we integrate the Poisson equation to get:

$$F(r) = -\frac{\partial \Phi}{\partial r} = -\frac{GM(r)}{r^2}, \quad (8.100)$$

where  $M(r)$  is the mass enclosed in the radius  $r$ . If we consider matter and DE perturbations  $M(r) = 4\pi a^2 \bar{\rho} \int_0^r (\Omega_m \delta_m(x) + \Omega_{de} \delta_{de}(x) (1 + 3c_s^2)) x^2 dx$ , where  $\delta_m$  has to be evolved independently. The system of equations to solve is then:

$$\frac{\partial \Delta}{\partial \tau} + (1 + c_s^2) \frac{\partial \Delta v}{\partial r} = -2(1 + c_s^2) \frac{\Delta v}{r} - 3\mathcal{H}(c_s^2 - w)(\Delta - 1 - w), \quad (8.101)$$

$$\frac{\partial \Delta v}{\partial \tau} + \frac{\partial}{\partial r} \left[ \Delta v^2 + \frac{c_s^2}{(1 + c_s^2)} \Delta \right] = -\frac{2\Delta v^2}{r} + (3w - 1)\mathcal{H}\Delta v + \Delta F(r), \quad (8.102)$$

$$F(r) = -\frac{4\pi G a^2 \bar{\rho}}{r^2} \int_0^r (\Omega_m \delta_m(x) + \Omega_{de} \delta_{de}(x) (1 + 3c_s^2)) x^2 dx, \quad (8.103)$$

where the variables  $\Delta$  and  $v$  refer to the DE component alone.



# Chapter 9

## Future prospects

N-body simulations are an invaluable tool to understand the non-linear regime of gravitational collapse of matter on cosmological scales. In the second part of this thesis simulations allowed us to study in detail the effects of non-linearities on the matter power spectrum estimator and its covariance matrix on the scales that will be probed by upcoming galaxy surveys. This study is the object of publications Ref.s [26, 27]. The work on numerical methods for clustering dark energy simulations presented in the third part of the thesis will enable us to explore the late-time phenomenology of this class of models, that once compared to observations can help shed light on the nature of dark energy. The results of this work will be published in a series of papers that present the numerical methods, study the spherical collapse of DM over-densities in presence of DE perturbations and present the results of the first cosmological simulations of clustering DE scenarios, Ref.s [46, 25, 28] respectively. There are many possible further studies that can build upon the work presented here, some of which we will outline in the following.

As we already mentioned, covariance matrices are also affected by finite volume errors [see e.g. 79, 106]. In the DEUS-PUR simulation ensemble we have a set of simulations with the same mass resolution of the main set A but with volumes 8 times larger that we plan to use for the study of volume effects on the covariance matrix.

Since the matter power spectrum covariance is a key quantity for upcoming galaxy surveys, a number of approximated methods to estimate it have been proposed in the last years. Some of them rely on the simulation of several realisations with approximated methods to account for the non-linear regime [see e.g. 116, 165] and are thus subject to the same sampling errors that we discussed in Chapter 7. This means that an equally large number of

realisation is needed to achieve high precision in the estimated covariance. Other methods instead rely on theoretical modelling of the covariance [see e.g. 162, 115] and are thus exempt from sampling errors, but they may carry calibration errors or other forms of modelling errors [186]. Thus, it is of great interest to compare the covariance obtained with these methods with the one measured from N-body simulations and study the impact on cosmological parameter estimation.

In Chapter 6 we have shown that the probability distribution of the matter power spectrum estimator deviate from the Gaussian distribution at small scales. The distribution measured in the simulation set can be used to construct a likelihood function and compare the parameter errors obtained in the Fisher matrix approximation with those obtained with a full likelihood analysis. Moreover, since these deviations are limited to a small skewing of a Gaussian, the distribution can be described as a series expansion around the Gaussian distribution and the posterior can be written as a series expansion of which the Fisher matrix is the lowest order [see e.g. 146]. This kind of approximations in the context of forecasts yield confidence contours which better capture non-linear degeneracies between cosmological parameters.

We plan to extend the DEUS-PUR simulation ensemble used in this thesis to different cosmological models. This will enable us to study the dependence of the covariance on the cosmological parameters, that has been neglected in most of the studies on galaxy surveys till now. Moreover, using the formalism of model selection we can study the ability of a given galaxy survey to rule out some cosmological models [119].

The numerical methods exposed in Chapter 8 are meant to be implemented in the code RAMSES [170], where similar methods are used to simulate the baryonic matter component. This means that by simply modifying the hydrodynamical solver we can take advantage of a well tested N-body code and AMR structure. In particular, we will implement the Riemann solvers described in Chapter 8 and modify the Godunov solver to take into account the differences between the baryonic hydrodynamic equations and the ones for the clustering Dark Energy. Simulations produced with the modified code will allow us to explore the phenomenology of clustering dark energy scenarios at cosmological scales. The presence of a clustering dark energy component will have effects on all the usual cosmological observables, like the matter power spectrum and the halo mass function, and can possibly lead to a new range of phenomena that can be tested against observations. These would in fact be among the first cosmological simulations with a sec-

ond dynamical dark component that can significantly alter the dynamics of gravitational collapse on the scale of the dark matter halos.

At the same time, the 1D Godunov solver can be used to solve simplified problems in spherical symmetry, such as the collapse of a top-hat perturbation in a cosmological setting or stellar equilibrium in presence of dark energy perturbations. The first case has been studied before with analytical methods in Ref.s [49, 19], allowing us to compare the numerical solution to the analytical one under certain conditions. As already mentioned, the methods developed in this thesis can be generalised to any non-relativistic fluid-like component that can be characterised by an equation of state parameter and the speed of sound. This can be of interest for unified Dark Matter - Dark Energy scenarios [see e.g. 23] or alternative Dark Matter scenarios [see e.g. 92].



## Acknowledgments

The research leading to these results has received funding from the European Research Council under the European Community's Seventh Framework Programme (FP7/2007-2013 Grant Agreement no. 279954).

I wish to thank first of all my supervisor, Pier Stefano Corasaniti, for his constant guidance during these years of intense work and for his openness and willingness to discuss, that encouraged me to bring forth my ideas and develop my independence. Conversations with him sparked many ideas and his insights on the academic world have always been very helpful.

I thank the CNRS, the Observatory of Paris and the ED 127 for giving me the opportunity to do my PhD at LUTh. I also want to thank the staff of LUTh for their support during my stay in Meudon. A special thanks to the informatics team for their help and availability.

I am grateful to my research group, the COS team at LUTh, for their support. Discussions at journal clubs, meetings or over a coffee have always been stimulating and fruitful. I want to thank the students of the group for their suggestions, the chats and pub excursions over these three long years. I am particularly grateful to Vincent Reverdy, my co-bureau and partner in running the huge simulation sets used in this thesis, for introducing me to doxygen, bash scripting and python, all tools that I used every day since then.

I thank the thesis committee members for dedicating their time to the exposition of my research work. I particularly thank Lauro Moscardini and Will Percival for reading this manuscript thoroughly. I also want to thank Lauro, Bruce Bassett and Filippo Vernizzi for writing recommendation letters for me while I was looking for a post-doc. Thanks for being so patient and kind to me.

With regards to topics discussed in this thesis, I acknowledge useful discussions and/or collaborative work with Thomas Kitching, Luca Amendola and Emiliano Sefusatti. I also want to thank Ben Wandelt and Stephane Colombi for their bayesian statistic classes, that introduced me to this branch of statistics that revealed very important to frame my research work. I also wish to thank Andrey Kravtsov and Nick Gnedin for having me at the Computational Cosmology summer school, where I learned plenty about N-body codes, which have had a fundamental role in this thesis.

The biggest thanks goes to my family for their constant support during all my years as a student, for believing in my dreams and encouraging me to follow them without regrets. Last but not least I want to thank my life partner Alà Eddin for being at my side both in the most joyful and stressful moments of this PhD experience.

# Bibliography

- [1] S. J. Aarseth. Dynamical evolution of clusters of galaxies, I. *Monthly Notices of the Royal Astronomical Society*, 126:223, 1963.
- [2] S. J. Aarseth. *Gravitational N-Body Simulations*. Cambridge University Press, 2003.
- [3] S. Agarwal, F. B. Abdalla, H. A. Feldman, O. Lahav, and S. A. Thomas. PkANN - II. A non-linear matter power spectrum interpolator developed using artificial neural networks. *Monthly Notices of the Royal Astronomical Society*, 439:2102, 2014.
- [4] S. Agarwal, P. S. Corasaniti, S. Das, and Y. Rasera. Small scale clustering of late forming dark matter. *Physical Review D*, 92:063502, 2015.
- [5] J.-M. Alimi, V. Bouillot, Y. Rasera, et al. First-ever full observable universe simulation. In *Proceedings of the International Conference on High Performance Computing, Networking, Storage and Analysis*, number 73 in Super Computing 2012. IEEE Computer Society Press, 2012.
- [6] J.-M. Alimi, A. Fuzfa, V. Boucher, Y. Rasera, J. Courtin, and P. S. Corasaniti. Imprints of dark energy on cosmic structure formation: I) realistic quintessence models. *Monthly Notices of the Royal Astronomical Society*, 401:775, 2010.
- [7] R. A. Alpher and R. Herman. Evolution of the universe. *Nature*, 162:774, 1948.
- [8] D. Anderhalden, A. Schneider, A. V. Macciò, J. Diemand, and G. Bertone. Hints on the nature of dark matter from the properties of Milky Way satellites. *Journal of Cosmology and Astroparticle Physics*, 03:014A, 2013.

- [9] L. Anderson et al. The clustering of galaxies in the SDSS-III Baryon Oscillation Spectroscopic Survey: baryon acoustic oscillations in the Data Releases 10 and 11 galaxy samples. *Monthly Notices of the Royal Astronomical Society*, 441:24, 2014.
- [10] T. W. Anderson. *An introduction to multivariate statistical analysis*. Wiley - Interscience, third edition, 2003.
- [11] R. E. Angulo, C. M. Baugh, C. Frenk, and C. G. Lacey. The detectability of baryonic acoustic oscillations in future galaxy surveys. *Monthly Notices of the Royal Astronomical Society*, 383:755, 2012.
- [12] S. Anselmi, G. Ballestreros, and M. Pietroni. Non-linear dark energy clustering. *Journal of Cosmology and Astroparticle Physics*, 11:014, 2011.
- [13] S. Anselmi, D. Lopez Nacir, and E. Sefusatti. Non-linear effects of dark energy clustering beyond the acoustic scale. *Journal of Cosmology and Astroparticle Physics*, 07:013, 2014.
- [14] C. Armendariz-Picon, V. Mukhanov, and P. J. Steinhardt. Essentials of k-essence. *Physical Review D*, 63:103510, 2001.
- [15] J. M. Bardeen, J. R. Bond, N. Kaiser, and A. S. Szalay. The statistics of peaks of gaussian random fields. *Astrophysical Journal*, 304:15, 1986.
- [16] J. Barnes and P. Hut. A hierarchical  $O(N \log N)$  force-calculation algorithm. *Nature*, 324:466, 1986.
- [17] S. Bashinsky and E. Bertschinger. Position-space description of the Cosmic Microwave Background and its temperature correlation function. *Physical Review Letters*, 87:081301, 2001.
- [18] S. Bashinsky and E. Bertschinger. Dynamics of cosmological perturbations in position space. *Physical Review D*, 65:123008, 2002.
- [19] T. Basse, O. Eggers Bjaelde, and Y. Y. Y. Wong. Spherical collapse of dark energy with an arbitrary sound speed. *Journal of Cosmology and Astroparticle Physics*, 10:038, 2011.
- [20] R. A. Battye and A. Moss. Evidence for massive neutrinos from cosmic microwave background and lensing observations. *Physical Review Letters*, 112:051303, 2014.

- [21] R. Bean and O. Dore. Probing dark energy perturbations: the dark energy equation of state and speed of sound as measured by WMAP. *Physical Review D*, 69:083503, 2004.
- [22] F. Bernardeau, S. Colombi, E. Gaztañaga, and R. Scoccimarro. Large-scale structure of the universe and cosmological perturbation theory. *Physics Reports*, 367:1, 2002.
- [23] D. Bertacca, S. Matarrese, and M. Pietroni. Unified dark matter in scalar field cosmologies. *Modern Physics Letters A*, 22:2893, 2007.
- [24] J. Binney and S. Tremaine. *Galactic Dynamics*. Princeton University Press, second edition, 2008.
- [25] L. Blot and P. S. Corasaniti. Non-linear eulerian hydrodynamics of cosmic dark fluids: Spherical collapse (II). In preparation.
- [26] L. Blot, P. S. Corasaniti, J.-M. Alimi, V. Reverdy, and Y. Rasera. Matter power spectrum covariance matrix from the DEUS-PUR  $\Lambda$ CDM simulations: Mass resolution and non-gaussian errors. *Monthly Notices of the Royal Astronomical Society*, 446:1756, 2015.
- [27] L. Blot, P. S. Corasaniti, L. Amendola, and T. Kitching. Non-linear matter power spectrum covariance matrix errors and cosmological parameter uncertainties for Euclid-like surveys. In preparation.
- [28] L. Blot, P. S. Corasaniti, et al. Non-linear eulerian hydrodynamics of cosmic dark fluids: Cosmological simulations of clustering dark energy scenarios (III). In preparation.
- [29] G. Boillat. Chocs caractéristiques. *Comptes rendus hebdomadaires des seances de l'Academie des Sciences serie A*, 274:1018, 1972.
- [30] W. B. Bonnor. Jeans' formula for gravitational instability. *Monthly Notices of the Royal Astronomical Society*, 117:104, 1957.
- [31] M. Boylan-Kolchin, J. S. Bullock, and M. Kaplinghat. Too big to fail? The puzzling darkness of massive Milky Way subhaloes. *Monthly Notices of the Royal Astronomical Society: Letters*, 415:L40, 2011.
- [32] G. L. Bryan and M. L. Norman. Simulating X-ray clusters with Adaptive Mesh Refinement. In D. A. Clarke and M. J. West, editors, *Computational Astrophysics: 12th Kingston Meeting on Theoretical Astrophysics*, volume 123 of *Astronomical Society of the Pacific Conference Series*, page 363, 1997.

- [33] E. M. Burbidge, G. R. Burbidge, W. A. Fowler, and F. Hoyle. Synthesis of the elements in stars. *Reviews of Modern Physics*, 29:547, 1957.
- [34] R. R. Caldwell, R. Dave, and P. J. Steinhardt. Cosmological imprint of an energy component with general equation of state. *Physical Review Letters*, 80:1582, 1998.
- [35] J. Carlson, M. White, and N. Padmanabhan. Critical look at cosmological perturbation theory techniques. *Physical Review D*, 80:043531, 2009.
- [36] J. Carron. On the incompleteness of the moment and correlation function hierarchy as probes of the lognormal field. *Astrophysical Journal*, 738:86, 2011.
- [37] L.-Y. Chiang and P. Coles. Phase information and the evolution of cosmological density perturbations. *Monthly Notices of the Royal Astronomical Society*, 311:809, 2000.
- [38] T. Clifton, P. G. Ferreira, A. Padilla, and C. Skordis. Modified gravity and cosmology. *Physics Reports*, 513:1, 2012.
- [39] S. Cole et al. The 2dF Galaxy Redshift Survey: Power-spectrum analysis of the final dataset and cosmological implications. *Monthly Notices of the Royal Astronomical Society*, 362:505, 2005.
- [40] P. Colella and H. M. Glaz. Efficient solution algorithms for the Riemann problem for real gases. *Journal of Computational Physics*, 59:264, 1985.
- [41] P. Colella and P. R. Woodward. The piecewise parabolic method (PPM) for gas-dynamical simulations. *Journal of Computational Physics*, 54:174, 1984.
- [42] P. Coles and B. Jones. A lognormal model for the cosmological mass distribution. *Monthly Notices of the Royal Astronomical Society*, 248:1, 1991.
- [43] P. Coles and F. Lucchin. *Cosmology: the origin and evolution of cosmic structure*. Wiley, second edition, 2002.
- [44] S. Colombi, S. Dodelson, and M. Widrow. Large scale structure tests of warm dark matter. *Astrophysical Journal*, 458:1, 1996.
- [45] E. J. Copeland, M. Sami, and S. Tsujikawa. Dynamics of dark energy. *International Journal of Modern Physics D*, 15:1753, 2006.

- [46] P. S. Corasaniti and L. Blot. Non-linear eulerian hydrodynamics of cosmic dark fluids: Riemann problem and upwind schemes (I). To be submitted.
- [47] P. S. Corasaniti, T. Giannantonio, and A. Melchiorri. The essence of quintessence and the cost of compression. *Physical Review D*, 71:123521, 2005.
- [48] J. Courtin, Y. Rasera, J.-M. Alimi, P. S. Corasaniti, V. Boucher, and A. Fuzfa. Imprints of dark energy on cosmic structure formation: II) non-universality of the halo mass function. *Monthly Notices of the Royal Astronomical Society*, 410:1911, 2011.
- [49] P. Creminelli, G. D’Amico, J. Noreña, L. Senatore, and F. Vernizzi. Spherical collapse in quintessence models with zero speed of sound. *Journal of Cosmology and Astroparticle Physics*, 03:047, 2011.
- [50] P. Creminelli, G. D’Amico, J. Noreña, and F. Vernizzi. The effective theory of quintessence: the  $w < -1$  side unveiled. *Journal of Cosmology and Astroparticle Physics*, 02:018, 2009.
- [51] M. Crocce, S. Pueblas, and R. Scoccimarro. Transients from initial conditions in cosmological simulations. *Monthly Notices of the Royal Astronomical Society*, 373:369, 2006.
- [52] M. Crocce and R. Scoccimarro. Nonlinear evolution of baryon acoustic oscillations. *Physical Review D*, 77:023533, 2008.
- [53] S. Das and N. Weiner. Late forming dark matter in theories of neutrino dark energy. *Physical Review D*, 84:123511, 2011.
- [54] K. S. Dawson et al. The Baryon Oscillation Spectroscopic Survey of SDSS-III. *Astronomical Journal*, 145:10, 2013.
- [55] P. de Bernardis et al. A flat universe from high-resolution maps of the cosmic microwave background radiation. *Nature*, 404:955, 2000.
- [56] R. De Putter, D. Huterer, and E. V. Linder. Measuring the speed of dark: detecting dark energy perturbations. *Physical Review D*, 81:103513, 2010.
- [57] W. De Sitter. Einstein’s theory of gravitation and its astronomical consequences. Third paper. *Monthly Notices of the Royal Astronomical Society*, 78:3, 1917.

- [58] R. H. Dicke, P. J. E. Peebles, P. G. Roll, and D. T. Wilkinson. Cosmic black-body radiation. *Astrophysical Journal*, 142:414, 1965.
- [59] T. H. Dupree. Nonlinear theory of drift-wave turbulence and enhanced diffusion. *Physics of Fluids*, 10:1049, 1967.
- [60] J. Einasto, A. Kaasik, and E. Saar. Dynamic evidence on massive coronas of galaxies. *Nature*, 250:309, 1974.
- [61] A. Einstein. Cosmological considerations in the general theory of relativity. *Sitzungsber. Preuss. Akad. Wiss. Berlin (Math. Phys.)*, pages 142–152, 1917.
- [62] A. Einstein. Einstein archives doc. 15 085. In H. Kragh, editor, *Cosmology and Controversy: The Historical Development of Two Theories of the Universe*, page 54. Princeton University Press, 1996.
- [63] D. J. Eisenstein et al. Detection of the baryon acoustic peak in the large-scale correlation function of SDSS Luminous Red Galaxies. *Astrophysical Journal*, 633:5, 2005.
- [64] D. J. Eisenstein and W. Hu. Baryonic features in the matter transfer function. *Astrophysical Journal*, 496:605, 1998.
- [65] D. J. Eisenstein, H.-J. Seo, S. E., and D. N. Spergel. Improving cosmological distance measurements by reconstruction of the baryon acoustic peak. *Astrophysical Journal*, 664:675, 2007.
- [66] J. K. Erickson, R. R. Caldwell, P. J. Steinhardt, C. Armendariz-Picon, and V. Mukhanov. Measuring the speed of sound of quintessence. *Physical Review Letters*, 69:083503, 2002.
- [67] S. M. Faber and J. S. Gallagher. Masses and mass-to-light ratios of galaxies. *Annual Review of Astronomy and Astrophysics*, 17:135, 1979.
- [68] K. B. Fisher, M. Davis, M. A. Strauss, A. Yahil, and J. P. Huchra. The power spectrum of IRAS galaxies. *Astrophysical Journal*, 402:42, 1993.
- [69] A. Friedmann. On the curvature of space. *Z. Phys.*, 10:377, 1922.
- [70] A. Friedmann. On the possibility of a world with constant negative curvature of space. *Z. Phys.*, 21:326, 1924.
- [71] J. N. Fry. The evolution of bias. *Astrophysical Journal Letters*, 461:65, 1996.

- [72] B. Fryxell et al. FLASH: an adaptive mesh hydrodynamics code for modeling astrophysical thermonuclear flashes. *Astrophysical Journal Supplement Series*, 131:273, 2000.
- [73] G. Gamow. Expanding universe and the origin of elements. *Physical Review*, 70:572, 1946.
- [74] J. Gleyzes, D. Langlois, and F. Vernizzi. A unifying description of dark energy. *International Journal of Modern Physics D*, 23:1443010, 2014.
- [75] S. K. Godunov. A finite difference method for the computation of discontinuous solutions of the equations of fluid dynamics. *Matematicheskii Sbornik*, 89:271, 1959.
- [76] J. J. Gottlieb and C. P. T. Groth. Assessment of Riemann solvers of unsteady one-dimensional inviscid flows of perfect gases. *Journal of Computational Physics*, 78:437, 1988.
- [77] L. P. Grishchuk and Y. B. Zeldovich. Gravitational instability in a multicomponent fluid. *Soviet Astronomy*, 25:267, 1981.
- [78] A. Guth. Inflationary universe: A possible solution to the horizon and flatness problems. *Physical Review D*, 23:347, 1981.
- [79] A. J. S. Hamilton, C. D. Rimes, and R. Scoccimarro. On measuring the covariance matrix of the non-linear power spectrum from simulations. *Monthly Notices of the Royal Astronomical Society*, 371:1188, 2006.
- [80] S. Hanany et al. A measurement of the cosmic microwave background anisotropy on angular scales of  $10^{-5}^{\circ}$ . *Astrophysical Journal Letters*, 545:L5, 2000.
- [81] J. Hartlap, P. Simon, and P. Schneider. Why your model parameter confidences might be too optimistic. Unbiased estimation of the inverse covariance matrix. *Astronomy and Astrophysics*, 464:399, 2007.
- [82] K. Heitmann, M. White, C. Wagner, S. Habib, and D. Higdon. The Coyote universe. I. Precision determination of the nonlinear matter power spectrum. *Astrophysical Journals*, 715:104, 2010.
- [83] R. W. Hockney and J. W. Eastwood. *Computer Simulations Using Particles*. McGraw - Hill, 1981.
- [84] W. Hu. Structure formation with generalized dark matter. *Astrophysical Journal*, 506:485, 1998.

- [85] E. Hubble. NGC 6822, a remote stellar system. *Astrophysical Journal*, 62:409, 1925.
- [86] E. Hubble. A relation between distance and radial velocity among extra-galactic nebulae. *Proc. Nat. Acad. Sci.*, 15:168–173, 1929.
- [87] E. Hubble. Effects of red shifts on the distribution of nebulae. *Astrophysical Journal*, 84:517, 1936.
- [88] M. J. Ivings, D. M. Causon, and E. F. Toro. On Riemann solvers for compressible liquids. *International Journal for Numerical Methods in Fluids*, 28:395, 1998.
- [89] J. Jeans. The stability of a spherical nebula. *Philosophical Transactions of the Royal Society of London.*, 199:1, 1902.
- [90] A. Jeffrey. *Quasilinear Hyperbolic Systems and Waves*. Pitman Publishing, 1976.
- [91] E. Jennings, C. M. Baugh, R. E. Angulo, and S. Pascoli. Simulations of quintessential cold dark matter: beyond the cosmological constant. *Monthly Notices of the Royal Astronomical Society*, 401:2181, 2010.
- [92] J. Khoury. Alternative to particle dark matter. *Physical Review D*, 91:024022, 2015.
- [93] A. Kiessling, A. N. Taylor, and A. F. Heavens. Simulating the effect of non-linear mode coupling in cosmological parameter estimation. *Monthly Notices of the Royal Astronomical Society*, 416:1045, 2011.
- [94] Y. L. Klimontovich. *The Statistical Theory of Non-Equilibrium Processes in a Plasma*. MIT Press, 1967.
- [95] A. Klypin, A. V. Kravtsov, O. Valenzuela, and F. Prada. Where are the missing galactic satellites? *Astrophysical Journal*, 522:82, 1999.
- [96] A. V. Kravtsov, A. Klypin, and A. M. Khokhlov. Adaptive refinement tree: A new high-resolution N-body code for cosmological simulations. *Astrophysical Journal Supplement Series*, 111:73, 1997.
- [97] A. Labatie, J. L. Starck, and M. Rachièze-Rey. Effect of model-dependent covariance matrix for studying Baryon Acoustic Oscillations. *Astrophysical Journal*, 760:97, 2012.

- [98] R. Laureijs et al. Euclid definition study report. *arXiv:1110.3193*, 2011.
- [99] J. Lee and U.-L. Pen. Information content in the galaxy angular power spectrum from the Sloan Digital Sky Survey and its implication on weak-lensing analysis. *Astrophysical Journal Letters*, 686:1, 2008.
- [100] G. Lemaître. Un univers homogène de masse constante et de rayon croissant rendant compte de la vitesse radiale des nébuleuses extragalactiques. *Annales de la Société Scientifique de Bruxelles*, 47:49–59, 1927.
- [101] G. Lemaître. The beginning of the world from the point of view of quantum theory. *Nature*, 127:706, 1931.
- [102] G. Lemaître. Evolution of the expanding universe. *Proceedings of the National Academy of Sciences*, 20:12, 1934.
- [103] J. Lesgourgues. The Cosmic Linear Anisotropy Solving System (CLASS) I: Overview. *arXiv:1104.2932*, 2011.
- [104] J. Lesgourgues and S. Pastor. Neutrino cosmology and Planck. *New Journal of Physics*, 16:065002, 2014.
- [105] A. Lewis, A. Challinor, and A. Lasenby. Efficient computation of Cosmic Microwave Background anisotropies in closed Friedmann-Robertson-Walker models. *Astrophysical Journal*, 538:473, 2000.
- [106] Y. Li, W. Hu, and M. Takada. Super-sample covariance in simulations. *Physical Review D*, 89:083519, 2014.
- [107] J. A. S. Lima, V. Zanchin, and R. Brandenberger. On the Newtonian cosmology equations with pressure. *Monthly Notices of the Royal Astronomical Society: Letters*, 291:L1, 1997.
- [108] R. G. Mann, J. A. Peacock, and A. F. Heavens. Eulerian bias and the galaxy density field. *Monthly Notices of the Royal Astronomical Society*, 293:209, 1998.
- [109] H. Martel and P. R. Shapiro. A convenient set of comoving cosmological variables and their application. *Monthly Notices of the Royal Astronomical Society*, 297:467, 1998.

- [110] J. C. Mather et al. Measurement of the cosmic microwave background spectrum by the COBE FIRAS instrument. *Astrophysical Journal*, 420:439, 1994.
- [111] A. Meiksin and M. White. The growth of correlations in the matter power spectrum. *Monthly Notices of the Royal Astronomical Society*, 308:1179, 1999.
- [112] A. Melott, S. F. Shandarin, J. S. Randall, and Y. Suto. Demonstrating discreteness and collision error in cosmological N-body simulations of Dark Matter gravitational clustering. *Astrophysical Journal Letters*, 479:L79, 1997.
- [113] R. Menikoff and B. J. Plohr. The Riemann problem for fluid flow of real materials. *Reviews of Modern Physics*, 61:75, 1989.
- [114] P. Meszaros. The behaviour of point masses in an expanding cosmological substratum. *Astronomy and Astrophysics*, 37:225, 1974.
- [115] I. Mohammed and U. Seljak. Analytic model for the matter power spectrum, its covariance matrix and baryonic effects. *Monthly Notices of the Royal Astronomical Society*, 445:3382, 2014.
- [116] P. Monaco, E. Sefusatti, S. Borgani, M. Crocce, P. Fosalba, R. K. Sheth, and T. Theuns. An accurate tool for the fast generation of dark matter halo catalogues. *Monthly Notices of the Royal Astronomical Society*, 433:2389, 2013.
- [117] B. Moore. Evidence against dissipation-less dark matter from observations of galaxy haloes. *Nature*, 370:629M, 1994.
- [118] D. F. Mota and C. van de Bruck. On the spherical collapse model in dark energy cosmologies. *Astronomy and Astrophysics*, 421:71, 2004.
- [119] P. Mukherjee, D. Parkinson, P. S. Corasaniti, A. R. Liddle, and M. Kunz. Model selection as a science driver for dark energy surveys. *Monthly Notices of the Royal Astronomical Society*, 369:1725, 2006.
- [120] W. Ngan, J. Harnois-Déraps, U.-L. Pen, P. McDonald, and I. MacDonald. Non-gaussian errors of baryonic acoustic oscillations. *Monthly Notices of the Royal Astronomical Society*, 419:2949, 2012.
- [121] D. Obreschkow, C. Power, M. Bruderer, and C. Bonvin. A robust measure of cosmic structure beyond the power spectrum: Cosmic filaments

- and the temperature of dark matter. *Astrophysical Journal*, 762:115, 2013.
- [122] J. P. Ostriker, P. J. E. Peebles, and A. Yahil. The size and mass of galaxies, and the mass of the universe. *Astrophysical Journal*, 194:L1, 1974.
- [123] N. Padmanabhan and M. White. Calibrating the baryon oscillation ruler for matter and halos. *Physical Review D*, 80:063508, 2009.
- [124] P. J. E. Peebles. *The large-scale structure of the universe*. Princeton University Press, 1980.
- [125] A. A. Penzias and R. W. Wilson. A measurement of excess antenna temperature at 4080 Mc/s. *Astrophysical Journal*, 142:419, 1965.
- [126] W. J. Percival, S. Cole, D. J. Eisenstein, R. C. Nichol, J. A. Peacock, A. C. Pope, and A. S. Szalay. Measuring the Baryon Acoustic Oscillation scale using the Sloan Digital Sky Survey and 2dF Galaxy Redshift Survey. *Monthly Notices of the Royal Astronomical Society*, 381:1053, 2007.
- [127] W. J. Percival et al. The 2dF Galaxy Redshift Survey: The power spectrum and the matter content of the universe. *Monthly Notices of the Royal Astronomical Society*, 327:1297, 2001.
- [128] S. Perlmutter et al. Measurements of  $\Omega$  and  $\Lambda$  from 42 high-redshift supernovae. *Astrophysical Journal*, 517:565, 1999.
- [129] Planck Collaboration. Planck 2015 results. XIII. Cosmological parameters. *arXiv:1502.01589*, 2015.
- [130] V. Poulin and S. P. D. Loophole to the universal photon spectrum in electromagnetic cascades and application to the cosmological Lithium problem. *American Physical Society*, 114:091101, 2015.
- [131] S. J. Press. *Applied Multivariate Analysis*. Krieger Publishing Co., Malabar, 1982.
- [132] W. H. Press, S. A. Teukolsky, W. T. Vetterling, and B. P. Flannery. *Numerical Recipes: The Art of Scientific Computing*. Cambridge University Press, third edition, 2007.

- [133] S. Prunet, C. Pichon, D. Aubert, D. Pogosyan, R. Teyssier, and S. Gottloeber. Initial conditions for large cosmological simulations. *Astrophysical Journal Supplement Series*, 178:179, 2008.
- [134] Y. Rasera, P. S. Corasaniti, J.-M. Alimi, V. Bouillot, V. Reverdy, and I. Balmès. Cosmic-variance limited baryon acoustic oscillations from the DEUS-FUR  $\Lambda$ CDM simulation. *Monthly Notices of the Royal Astronomical Society*, 440:1420, 2014.
- [135] A. G. Riess et al. Observational evidence from supernovae for an accelerating universe and a cosmological constant. *Astrophysical Journal*, 116:1009, 1998.
- [136] A. G. Riess et al. A 3% solution: Determination of the Hubble constant with the Hubble Space Telescope and Wide Field Camera 3. *Astrophysical Journal*, 730:119R, 2011.
- [137] C. D. Rimes and A. J. S. Hamilton. Information content of the non-linear power spectrum: the effect of beat-coupling to large scales. *Monthly Notices of the Royal Astronomical Society*, 371:1205, 2006.
- [138] H. P. Robertson. On the foundation of relativistic cosmology. *Proceedings of the National Academy of Sciences*, 15:822, 1929.
- [139] V. C. Rubin and W. K. J. Ford. Emission lines in the nuclear region of M31. *Bulletin of the American Astronomical Society*, 2:192, 1970.
- [140] D. Rudd, A. R. Zentner, and A. V. Kravtsov. Effects of baryons and dissipation on the matter power spectrum. *Astrophysical Journal*, 672:19, 2008.
- [141] A. D. Sakharov. Vacuum quantum fluctuations in curved space and the theory of gravitation. *Doklady Akademii Nauk SSSR*, 177:70, 1967.
- [142] M. Sato, T. Hamana, R. Takahashi, M. Takada, N. Yoshida, T. Matsubara, and N. Sugiyama. Simulations of Wide-Field Weak Lensing Surveys. I. Basic statistics and non-gaussian effects. *Astrophysical Journal*, 701:945, 2009.
- [143] R. Scoccimarro. Transients from initial conditions: a perturbative analysis. *Monthly Notices of the Royal Astronomical Society*, 299:1097, 1998.

- [144] R. Scoccimarro, M. Zaldarriaga, and L. Hui. Power spectrum correlations induced by nonlinear clustering. *Astrophysical Journal*, 527:1, 1999.
- [145] E. Sefusatti and F. Vernizzi. Cosmological structure formation with clustering quintessence. *Journal of Cosmology and Astroparticle Physics*, 03:047, 2011.
- [146] E. Sellentin, M. Quartin, and L. Amendola. Breaking the spell of Gaussianity: forecasting with higher order Fisher matrices. *Monthly Notices of the Royal Astronomical Society*, 441:1831, 2014.
- [147] E. Semboloni, L. van Waerbeke, C. Heymans, H. Takashi, S. Colombi, M. White, and Y. Mellier. Cosmic variance of weak lensing surveys in the non-gaussian regime. *Monthly Notices of the Royal Astronomical Society: Letters*, 375:L6, 2007.
- [148] H.-J. Seo, J. Eckel, D. J. Eisenstein, K. Metha, M. Metchnik, N. Padmanabhan, P. Pinto, R. Takahashi, M. White, and X. Xu. High-precision predictions for the acoustic scale in the nonlinear regime. *Astrophysical Journal*, 720:1650, 2010.
- [149] S. F. Shandarin and Y. B. Zeldovich. The large-scale structure of the universe: Turbulence, intermittency, structures in a self-gravitating medium. *Reviews of Modern Physics*, 61:185, 1989.
- [150] H. Shapley. Studies based on the colors and magnitudes in stellar clusters. VI. On the determination of the distances of globular clusters. *Astrophysical Journal*, 48:89, 1918a.
- [151] H. Shapley. Studies based on the colors and magnitudes in stellar clusters. VII. The distances, distribution in space, and dimensions of 69 globular clusters. *Astrophysical Journal*, 48:154, 1918b.
- [152] J. Silk. The spectrum of density perturbations in an expanding universe. In M. S. Longair, editor, *Confrontation of cosmological theories with observational data*, volume 63 of *IAU Symposium*, page 175, 1974.
- [153] V. M. Slipher. Nebulae. *Proceedings of the American Philosophical Society*, 56:403, 1917.
- [154] R. E. Smith. Covariance of cross-correlations: towards efficient measures for large-scale structure. *Monthly Notices of the Royal Astronomical Society*, 400:851, 2009.

- [155] G. F. Smoot et al. Structure in the COBE Differential Microwave Radiometer first-year maps. *Astrophysical Journal*, 396:L1, 1992.
- [156] G. A. Sod. A survey of several finite difference methods for system of nonlinear hyperbolic conservation laws. *Journal of Computational Physics*, 27:1, 1978.
- [157] D. N. Spergel et al. Three-year Wilkinson Microwave Anisotropy Probe (WMAP) observations: Implications for cosmology. *Astrophysical Journal Supplement Series*, page 377, 170.
- [158] D. N. Spergel and P. J. Steinhardt. Observational evidence for self-interacting cold dark matter. *Physical Review Letters*, 84:3760, 2000.
- [159] G. Strang. On the construction and comparison of different splitting schemes. *SIAM Journal on Numerical Analysis*, 5(3):506, 1968.
- [160] Super-Kamiokande Collaboration. Evidence for oscillation of atmospheric neutrinos. *Physical Review Letters*, 81:1562, 1998.
- [161] Super-Kamiokande Collaboration. A measurement of the appearance of atmospheric Tau neutrinos by Super-Kamiokande. *Physical Review Letters*, 110:181802, 2012.
- [162] M. Takada and W. Hu. Power spectrum super-sample covariance. *Physical Review D*, 87:123504, 2013.
- [163] R. Takahashi et al. Simulations of Baryon Acoustic Oscillations. II. Covariance matrix of the matter power spectrum. *Astrophysical Journal*, 700:479, 2009.
- [164] R. Takahashi et al. Non-gaussian error contribution to likelihood analysis of the matter power spectrum. *Astrophysical Journal*, 726:7, 2011.
- [165] S. Tassev, M. Zaldarriaga, and D. J. Eisenstein. Solving large scale structure in ten easy steps with COLA. *Journal of Cosmology and Astroparticle Physics*, 6:36, 2013.
- [166] A. N. Taylor, B. Joachimi, and T. Kitching. Putting the precision in precision cosmology: How accurate should your data covariance matrix be? *Monthly Notices of the Royal Astronomical Society*, 432:1928, 2013.
- [167] M. Tegmark et al. The 3D power spectrum of galaxies from the SDSS. *Astrophysical Journal*, 606:702, 2004.

- [168] M. Tegmark and P. J. E. Peebles. The time evolution of bias. *Astrophysical Journal Letters*, 500:79, 1998.
- [169] M. Tegmark, A. N. Taylor, and A. F. Heavens. Karhunen-Loève eigenvalue problems in cosmology: How should we tackle large data sets? *Astrophysical Journal*, 480:22, 1997.
- [170] R. Teyssier. Cosmological hydrodynamics with adaptive mesh refinement. *Astronomy and Astrophysics*, 385:337, 2002.
- [171] E. F. Toro. *Riemann Solvers and Numerical Methods for Fluid Dynamics: A Practical Introduction*. Springer, third edition, 2009.
- [172] S. Tsujikawa. Modified gravity models of dark energy. *Lecture Notes in Physics*, 800:99, 2010.
- [173] B. van Leer. Towards the ultimate conservative difference scheme. I. The quest for monotonicity. *Lecture Notes in Physics*, 18:163, 1973.
- [174] B. van Leer. Towards the ultimate conservative difference scheme. II. Monotonicity and conservation combined in a second-order scheme. *Journal of Computational Physics*, 14:361, 1974.
- [175] B. van Leer. Towards the ultimate conservative difference scheme. III. Upstream-centered finite-difference schemes for ideal compressible flow. *Journal of Computational Physics*, 23:263, 1977.
- [176] B. van Leer. Towards the ultimate conservative difference scheme. IV. A new approach to numerical convection. *Journal of Computational Physics*, 23:276, 1977.
- [177] B. van Leer. Towards the ultimate conservative difference scheme. V. A second-order sequel to Godunov’s method. *Journal of Computational Physics*, 32:101, 1979.
- [178] B. van Leer. On the relation between the upwind-differencing schemes of Godunov, Engquist, Osher and Roe. *Journal on Scientific and Statistical Computing*, 5:1, 1984.
- [179] B. van Leer. Upwind and high-resolution methods for compressible flow: from donor cell to residual-distribution schemes. *Communications in Computational Physics*, 1:192, 2006.

- [180] M. Vogelsberger, J. Zavala, S. Christine, and A. Jenkins. Dwarf galaxies in CDM and SIDM with baryons: observational probes of the nature of dark matter. *Monthly Notices of the Royal Astronomical Society*, 444:3684, 2014.
- [181] A. G. Walker. Distance in an expanding universe. *Monthly Notices of the Royal Astronomical Society*, 94:159, 1933.
- [182] M. White and W. Hu. A new algorithm for computing statistics of weak lensing by large-scale structure. *Astrophysical Journal*, 537:1, 2000.
- [183] S. D. M. White. Formation and evolution of galaxies. In R. Schaeffer, J. Silk, M. Spiro, and J. Zinn-Justin, editors, *Cosmology and large-scale structure*, page 349. Elsevier, 1996.
- [184] C. Wirtz. Einiges zur statistik der radialbewegungen von spiralnebeln und kugelsternhaufen. *Astronomische Nachrichten*, 215:349, 1922.
- [185] J. Wishart. The generalised product moment distribution in samples from a normal multivariate population. *Biometrika*, 20A:32, 1928.
- [186] H.-Y. Wu and D. Huterer. The impact of systematic uncertainties in N-body simulations on the precision cosmology from galaxy clustering: a halo model approach. *Monthly Notices of the Royal Astronomical Society*, 434:2556, 2013.
- [187] I. Zehavi et al. The luminosity and color dependence of the galaxy correlation function. *Astrophysical Journal*, 630:1, 2005.
- [188] Y. B. Zeldovich. Cosmological constant and elementary particles. *Soviet Physics JETP Letters*, 6:316, 1967.
- [189] Y. B. Zeldovich. An approximate theory for large density perturbations. *Astronomy and Astrophysics*, 5:84, 1970.
- [190] M. Zingale. Computational hydrodynamics for astrophysics. [http://bender.astro.sunysb.edu/hydro\\_by\\_example/CompHydroTutorial.pdf](http://bender.astro.sunysb.edu/hydro_by_example/CompHydroTutorial.pdf).
- [191] F. Zwicky. Die rotverschiebung von extragalaktischen nebeln. *Helvetica Physica Acta*, 6:110, 1933.
- [192] F. Zwicky. On the masses of nebulae and of clusters of nebulae. *Astrophysical Journal*, 86:217, 1937.